DISSERTATION

submitted to the

Combined Faculties for the Natural Sciences and for Mathematics
of the Ruperto-Carola University of Heidelberg, Germany

for the degree of

Doctor of Natural Sciences

Put forward by

Matthias Redlich
born in Heidelberg, Germany

Oral examination: 9 December 2014

STATISTICAL PROBES OF THE STANDARD COSMOLOGICAL MODEL

Referees:	Prof. Dr. Matthias Bartelmann
	Prof. Dr. Luca Amendola

ZUSAMMENFASSUNG

Teil I: Ist unser Universum auf den größten beobachtbaren Skalen räumlich homogen? Um diese Frage zu untersuchen, entwickeln wir eine flexible Methode, die auf sphärisch symmetrischen, aber räumlich inhomogenen Lemaître-Tolman-Bondi-Modellen basiert. Diese Methode ermöglicht es uns, eine Vielfalt alternativer kosmologischer Modelle zu studieren, die nicht dem kopernikanischen Prinzip folgen. Wir verwenden einen Monte-Carlo-Algorithmus, der das (lokale) Dichteprofil der theoretischen Modelle unter Berücksichtigung aktueller Beobachtungsdaten systematisch variiert und optimiert. Nach einer ausführlichen Analyse inhomogener Kosmologien mit und ohne kosmologischer Konstante kommen wir zu dem Schluss, dass die betrachteten Beobachtungsdaten keinen statistischen Hinweis auf eine Abweichung von räumlicher Homogenität auf großen Skalen enthalten. Es sind allerdings präzisere Messungen erforderlich, um die Annahmen des kosmologischen Prinzips endgültig zu bestätigen.

Teil II: Stehen die stärksten beobachteten Gravitationslinsen im Widerspruch zu den theoretischen Vorhersagen des kosmologischen Standardmodells? Um diese Frage zu diskutieren, betrachten wir die Extremwert- und Ordnungsstatistik der kosmologischen Verteilung der größten Einstein-Radien. Wir zeigen, dass Verschmelzungen von Galaxienhaufen die Einstein-Radien der stärksten Gravitationslinsen substanziell vergrößern können. Ein Vergleich mit aktuellen Beobachtungsdaten ergibt, dass es momentan keine verlässlichen statistischen Hinweise dafür gibt, dass die größten beobachteten Einstein-Radien die maximalen Erwartungen des kosmologischen Standardmodells übertreffen.

ABSTRACT

Part I: Is our Universe spatially homogeneous on the largest observable scales? To investigate this question, we develop a flexible method based on spherically symmetric, but radially inhomogeneous Lemaître-Tolman-Bondi models that allows us to study a wide range of non-Copernican cosmological models. We employ a Monte Carlo sampler to systematically vary the shape of the (local) matter density profile and determine the likelihood of the sampled models given a selected set of observational data. After analysing non-Copernican models with and without cosmological constant, we arrive at the final conclusion that the observational data considered provide no statistical evidence for deviations from spatial homogeneity on large scales. However, more accurate constraints are required to ultimately confirm the validity of the cosmological principle.

Part II: Are the strongest observed gravitational lenses in conflict with the predictions of the standard cosmological model? To address this question, we apply extreme value and order statistics to the cosmological distribution of the largest Einstein radii. We show that cluster mergers can substantially increase the Einstein radii of the strongest gravitational lenses. A comparison with current observational data reveals that, presently, there is no reliable statistical evidence for observed Einstein radii to exceed the theoretical expectations of the standard cosmological model.

CONTENTS

LIST OF FIGURES

LIST OF TABLES

ACRONYMS

CDF	cumulative distribution function
CDM	cold dark matter
CMB	cosmic microwave background
FLRW	Friedmann-Lemaître-Robertson-Walker
GEV	general extreme value
LSS	last scattering surface
LTB	Lemaître-Tolman-Bondi
MC	Monte Carlo
MCMC	Markov chain Monte Carlo
NFW	Navarro-Frenk-White
PDF	probability density function
PNC	past null cone

INTRODUCTION

The standard cosmological model is remarkably successful: Based on only six parameters, some of which are fundamental, some are effective, the spatially flat Λ cold dark matter (ΛCDM) model consistently explains the vast majority of cosmological observations (Weinberg 2008; Bartelmann 2010a). This success, however, comes at a high prize because the model requires that the cosmological constant Λ and cold dark matter make up $\sim 95\%$ of today's energy density of the Universe, while only $\sim 5\%$ consist of baryonic matter explained by the standard model of particle physics (Planck Collaboration et al. 2013). In other words, the *standard* cosmological model asserts that the energy content of the current epoch is almost entirely dominated by *non-standard* physics. Of course, this statement is deliberately provocative, but it is fair to say that the physical origin of the two dark components is still speculative, and a satisfying theoretical explanation has yet to be given (Peebles & Ratra 2003; Bertone et al. 2005; Amendola & Tsujikawa 2010).

These open questions certainly do not falsify the standard cosmological model, but they motivate to critically probe the theoretical foundations the model is built upon. One of these foundations is the cosmological principle, which asserts that our Universe is spatially isotropic and homogeneous when averaged over sufficiently large scales ($\gtrsim 100\,\mathrm{Mpc}$). This assumption is truly remarkable as if correct it implies that the space-time geometry of our Universe – which is notably inhomogeneous on small scales – should on large scales effectively be described by the simple class of highly symmetric Friedmann-Lemaître-Robertson-Walker (FLRW) models (Friedmann 1922; Lemaître 1927; Robertson 1935; Walker 1935). Statistical isotropy about our position seems to be well established, in particular given the observed distribution of galaxies (Hogg et al. 2005; Sarkar et al. 2009; Pullen & Hirata 2010; Scrimgeour et al. 2012) and the near-perfect isotropy of the cosmic microwave background (CMB; Bennett et al. 2013; Planck Collaboration et al. 2013). In contrast, spatial homogeneity cannot be directly observed. To this end, one would have to analyse the structure of three-dimensional space-like hypersections with constant time, which is impossible because all our observations are confined to the past null cone (PNC). As we look down the PNC, we simultaneously observe temporal and spatial evolution. Thus, we can hardly distinguish between a time-evolving homogeneous matter distribution and a spatially inhomogeneous matter distribution with a different time evolution (see Maartens 2011; Clarkson 2012, for detailed discussions). Therefore, it is perhaps fair to say that spatial homogeneity is only a working assumption that is, however, in good agreement with most cosmological observations.

Nonetheless, we can (and should) indirectly probe the fundamental assumption of spatial homogeneity by means of statistical methods. Non-Copernican cosmological models are one particular option to do this. We can theoretically construct spatially inhomogeneous cosmologies, calculate observable consequences of these models, and compare the corresponding predictions with observed data. The statistical likeli-

hood of the non-Copernican cosmologies considered can then be compared with the likelihood of the standard cosmological model, which eventually allows us to decide whether or not there is statistical support for deviations from spatial homogeneity.

We adopt such an approach in the first part of this thesis. To this end, in Chap. 1, we first introduce the Lemaître-Tolman-Bondi (LTB; Lemaître 1933; Tolman 1934; Bondi 1947) model, which is a spherically symmetric, but radially inhomogeneous dust solution of Einstein's field equations (Einstein 1915). If we assume that we – the observer – are located at the distinguished symmetry centre of an LTB space-time, we can construct non-Copernican cosmological models that conserve isotropy but may otherwise exhibit interesting physical properties such as varying spatial curvature, radially dependent expansion rates, or inhomogeneous matter density profiles.

This leads to the basic idea of Chap. 2: We assume that the space-time geometry around us is described by the LTB metric and expand the matter density profile of the (local) Universe in terms of flexible interpolation schemes and orthonormal polynomials. A Monte Carlo (MC) sampler is used to systematically vary the shape of the flexibly parametrised matter density profiles and maximise the likelihood given a selected set of observational data. In doing so, we aim to answer questions of the following kind: What does the statistically favoured matter density profile of the observable Universe look like? Can we find statistical evidence for deviations from spatial homogeneity on large scales? Could the observed (apparent) late-time acceleration of the expansion rate of the Universe be explained by a Gpc-scale void model without dark energy that is consistent with recent observational data?

After analysing various LTB models with and without cosmological constant, we conclude that the observational data considered in Chap. 2 provide no evidence for deviations from spatial homogeneity on large scales. However, our analysis is limited by the fact that linear perturbation theory in LTB models is quite demanding and we still lack the proper tools for numerically solving the linear perturbation equations with realistic cosmological initial conditions. To be conservative, we thus have to exclude all observables that depend on the details of structure formation. To ultimately confirm the validity of the cosmological principle, however, it would be important to include more observational data in future analyses. Given upcoming surveys such as the Euclid mission (Amendola et al. 2013), we expect that studies of cosmological weak lensing will meaningfully complement the observational data used in Chap. 2. Therefore, in Chap. 3, we outline a simple framework for studying weak gravitational lensing in linearly perturbed LTB models. This framework can readily be applied as soon as our new numerical code for solving the linear perturbation equations on LTB backgrounds has been finished (Meyer et al., in preparation).

In comparison to the first part, we adopt a completely different perspective in the second part of this thesis. We no longer question the theoretical foundations the standard cosmological model is based on but instead assume that the ΛCDM model is a valid description of our Universe and study the statistics of strong-lensing events. Before going into details, it is perhaps useful to explain why strong-lensing statistics is a valuable cosmological probe.

At first, we note that only very massive objects can act as strong gravitational lenses. Thus, typical strong-lensing phenomena, such as giant gravitational arcs or

multiply imaged source galaxies, are mainly observed in massive galaxy clusters. The frequency of strong-lensing events in a certain cosmological volume is hence sensitive to the abundance of galaxy clusters, which in turn depends on the halo mass function, the matter density parameter, and the normalisation of the power spectrum (Bartelmann 2010a). Furthermore, the strong-lensing efficiency of individual clusters is sensitive to their internal properties, such as the concentration of the inner core or the detailed shape of the density profile (e. g. amount of triaxiality). These characteristics encode important information about the fundamental properties of dark matter (e. g. velocity dispersion) and the details of structure formation (formation time of clusters, merging activity, etc.). Finally, we note that the lensing efficiency also depends on the angular-diameter distances between the observer, the cluster, and the lensed source. Consequently, strong lensing also probes the geometry of the Universe.

There are many more aspects that influence the statistical strong-lensing efficiency of cosmological cluster populations (see Meneghetti et al. 2013, for a detailed review). However, the effects outlined above already indicate that strong-lensing statistics is sensitive to a wide range of theoretical assumptions concerning the foundations of the cosmological model (e. g. nature of dark matter), the details of structure formation, and the exact values of the cosmological parameters. It is precisely this large diversity that makes the statistics of strong lensing such a powerful cosmological tool.

As recently reviewed by Meneghetti et al. (2013), there are two persistent problems that have been controversially discussed over the last fifteen years: The *arc statistics problem* denotes the ongoing debate whether or not the high rate of observed gravitational arcs substantially exceeds the theoretically expected abundance of arcs. The *Einstein ring problem* names the concern raised by several authors that the largest observed Einstein radii are too large to be consistent with the ΛCDM model. In essence, both problems question whether the strongest observed gravitational lenses exceed the maximum theoretical expectations of the standard cosmological model. This is the key issue of the second part of this thesis.

Our approach to this problem consists of several successive steps. At first, we briefly summarise the basics of strong gravitational lensing in Chap. 4. In particular, we define the strong-lensing cross section and the Einstein radius of a gravitational lens.

In Chap. 5, we explain the close link between the arc statistics problem and the Einstein ring problem, which eventually allows us to only focus on the statistics of the largest Einstein radii in the subsequent chapters. Moreover, we show that cluster mergers are an important mechanism to boost the strong-lensing efficiency of individual clusters. Based on a newly developed semi-analytic method, we demonstrate that cluster mergers are particularly relevant for the statistics of the strongest lenses, indicating that mergers might help to mitigate the tension between theory and observations.

Is the largest observed Einstein radius consistent with the ΛCDM model? The theory of extreme value statistics provides the proper mathematical framework for quantitatively answering such questions. In Chap. 6, we show that the occurrence probability of the largest observed Einstein radius in a concrete survey is well described by the general extreme value distribution. Given the current state of the theory, however, the extreme value distribution of the largest Einstein radius still is subject to

many model uncertainties. Therefore, in Chap. 7, we explain that it is beneficial to extend our statistical approach of Chap. 6 by considering the order statistics of the n largest Einstein radii. This allows formulating more robust ΛCDM exclusion criteria based on n observations instead of a single extreme event that might have been caused by an extremely peculiar lensing system that was statistically not accounted for.

At last, in Chap. 8, we combine all our previously developed techniques and calculate the extreme value and order statistics of the largest Einstein radii in a ΛCDM model taking the effect of cluster mergers into account. A comparison with current observational data reveals that, presently, there is no reliable statistical evidence for the strongest observed gravitational lenses to exceed the maximum theoretical expectations of the standard cosmological model.

Obviously, the two parts of this thesis discuss largely different topics. While the first part focuses on a very fundamental principle, the second part simultaneously probes a wide range of theoretical assumptions made within the framework of the ΛCDM model. What they have in common, however, is the basic idea to probe the standard cosmological model by means of statistical methods.

Unless stated otherwise, we set the speed of light to unity ($c = 1$) throughout this thesis. Moreover, in mathematical expressions, bold typeface indicates vectors.

Parts of this thesis were published in the following articles:

- **Redlich, M.**, Bolejko, K., Meyer, S., Lewis, G. F. & Bartelmann, M. (2014): *Probing spatial homogeneity with LTB models: a detailed discussion*. A&A, in press, DOI: 10.1051/0004-6361/201424553
- **Redlich, M.**, Bartelmann, M., Waizmann, J.-C. & Fedeli, C. (2012): *The strongest gravitational lenses. I. The statistical impact of cluster mergers*. A&A, 547, A66
- Waizmann, J.-C., **Redlich, M.** & Bartelmann, M. (2012): *The strongest gravitational lenses. II. Is the large Einstein radius of MACS J0717.5+3745 in conflict with ΛCDM?*. A&A, 547, A67
- Waizmann, J.-C., **Redlich, M.**, Meneghetti, M. & Bartelmann, M. (2014): *The strongest gravitational lenses. III. The order statistics of the largest Einstein radii*. A&A, 565, A28
- **Redlich, M.**, Waizmann, J.-C. & Bartelmann, M. (2014): *The strongest gravitational lenses: IV. The order statistics of the largest Einstein radii with cluster mergers*. A&A, 569, A34

Part I

PROBING THE COPERNICAN PRINCIPLE

1

THE LEMAÎTRE-TOLMAN-BONDI MODEL

ABSTRACT

This chapter briefly introduces the Lemaître-Tolman-Bondi model, which is a spherically symmetric, but radially inhomogeneous dust solution of Einstein's field equations. After motivating the general form of the LTB metric in comoving-synchronous coordinates, we outline the solution of Einstein's field equations. A short comparison between the LTB metric and the FLRW metric allows us to highlight distinctive features of radially inhomogeneous cosmological models. After that, we discuss the propagation of light in LTB space-times and define cosmic distances as measured by a central observer. Finally, we describe some practical details concerning the numerical implementation of LTB models.

This chapter closely follows the textbooks by Straumann (2004) and Plebański & Krasiński (2006), the latter containing a complete chapter (Chap. 18) dedicated to LTB models. A brief, introductory review article of LTB models is provided by Enqvist (2008).

1.1 GENERAL ANSATZ FOR THE LTB METRIC

Let us consider a four-dimensional, *spherically symmetric* Lorentz manifold M with metric g. Spherical symmetry implies that the manifold admits the group $SO(3)$ as an isometry group, such that the group orbits are two-dimensional space-like surfaces which can be identified with two-spheres S^2. Consequently, we can naturally foliate the manifold into $M = \tilde{M} \times S^2$ and introduce local coordinates (t, r) on the two-dimensional submanifold $\tilde{M}$ as well as polar coordinates (θ, ϕ) on the two-spheres S^2. The coordinates (t, r) can always be chosen such that the metric tensor (in these coordinates) has no time–space components. Based on these considerations, the general ansatz for the metric of a four-dimensional, spherically symmetric space-time can be written as

$$g = -\mathrm{e}^{2a(t,r)}\mathrm{d}t^2 + \left[\mathrm{e}^{2b(t,r)}\mathrm{d}r^2 + R^2(t,r)\left(\mathrm{d}\theta^2 + \sin^2\theta\mathrm{d}\phi^2\right)\right] . \tag{1}$$

The *areal radius* $R(t, r)$ is a free function that assigns an area A to the surfaces $\{t = \text{const}, r = \text{const}\}$ by the usual Euclidean relation $A = 4\pi R^2$.

Let us further assume that the space-time M is exclusively filled with dust, that is, a pressureless perfect fluid described by the energy-momentum tensor

$$T^{\mu\nu} = \rho u^\mu u^\nu , \tag{2}$$

where ρ denotes the local energy density and u^μ the four-velocity of the dust. With vanishing pressure ($p = 0$), Einstein's field equations imply that the dust particles move along time-like geodesics, $\nabla_u u = 0$. In that case, the time coordinate t can always be redefined such that $g_{tt} = 1$. Therefore, the general ansatz for the metric of a *spherically-symmetric, dust-filled* space-time can be written as

$$g = -\mathrm{d}t^2 + \mathrm{e}^{2b(t,r)}\mathrm{d}r^2 + R^2(t,r)\left(\mathrm{d}\theta^2 + \sin^2\theta\mathrm{d}\phi^2\right) . \tag{3}$$

In the above *synchronous-comoving* coordinates, the four-velocity of freely-falling dust particles is simply given by $u = \partial_t$.

1.2 SOLUTION OF EINSTEIN'S FIELD EQUATIONS

Einstein's field equations including the cosmological constant Λ read

$$G_{\mu\nu} = 8\pi G T_{\mu\nu} - \Lambda g_{\mu\nu} , \tag{4}$$

where $G_{\mu\nu}$, G, $T_{\mu\nu}$ and $g_{\mu\nu}$ are, respectively, the Einstein tensor, Newton's gravitational constant, the energy-momentum tensor and the metric tensor (Einstein 1915). Inserting the above ansatz for the metric (3) and the energy-momentum tensor of dust (2) into Eq. (4), we find the following components of the field equations:

$$G^0{}_0 = -\frac{\dot{R}^2}{R^2} - \frac{2\dot{b}\dot{R}}{R} + \mathrm{e}^{-2b}\left(\frac{R'^2}{R^2} + \frac{2R''}{R} - \frac{2b'R'}{R}\right) - \frac{1}{R^2} = -8\pi G\rho - \Lambda , \tag{5}$$

$$G^1{}_0 = \frac{2\mathrm{e}^{-2b}}{R}\left(\dot{b}R' - \dot{R}'\right) = 0 , \tag{6}$$

$$G^1{}_1 = -\frac{\dot{R}^2}{R^2} - \frac{2\ddot{R}}{R} + \mathrm{e}^{-2b}\frac{R'^2}{R^2} - \frac{1}{R^2} = -\Lambda , \tag{7}$$

$$G^2{}_2 = G^3{}_3 = -\dot{b}^2 - \ddot{b} - \frac{1}{R}\left(\dot{b}\dot{R} + \ddot{R}\right) + \frac{\mathrm{e}^{-2b}}{R}\left(R'' - b'R'\right) = -\Lambda , \tag{8}$$

where a dot and a prime indicate, respectively, differentiation with respect to time and radial coordinate.

To simplify the further discussion, we only consider solutions that are interesting for cosmology. We can therefore assume $\dot{R} \neq 0$. If $\dot{R}$ was zero, Eq. (6) would either require $R' = 0$ (leading to the Nariai (1950) solution) or $\dot{b} = 0$, which, due to Eq. (5), has temporally constant density. Furthermore, we assume $R' \neq 0$ and refer to Hellaby & Lake (1985) for a detailed discussion of shell crossings and regularity conditions, as well as Sect. 19.4 of Plebański & Krasiński (2006) for the Datt-Ruban solution.

Under these assumptions ($\dot{R} \neq 0$, $R' \neq 0$), we can rewrite Eq. (6) as

$$\frac{\mathrm{d}}{\mathrm{d}t}\left(\mathrm{e}^{-2b}R'^2\right) = 0 , \tag{9}$$

and integrate Eq. (9) in time to find

$$\mathrm{e}^{2b} = \frac{R'^2}{1 + 2E(r)} . \tag{10}$$

Here, $E(r)$ formally appears as an arbitrary function fixing the boundary conditions of the above integration. Substituting Eq. (10) into the general ansatz for the metric (3), we see that $E(r)$ determines the spatial curvature of the LTB space-time as a function of r. If $E(r)$ was set to zero, the $t = \text{const}$ hypersurfaces would be flat. We require $E(r) > -1/2$ for the metric (3) to have the right signature.

Next, we substitute Eq. (10) into Eq. (7), yielding

$$\frac{2\ddot{R}}{R} + \frac{\dot{R}^2}{R^2} - \frac{2E(r)}{R^2} - \Lambda = 0 \,. \tag{11}$$

After multiplying Eq. (11) with $\dot{R}R^2$, we find

$$\frac{\mathrm{d}}{\mathrm{d}t}\left(\dot{R}^2 R - 2E(r)R - \frac{1}{3}\Lambda R^3\right) = 0 \,, \tag{12}$$

which can also be integrated in time with the result

$$\dot{R}^2 = \frac{2M(r)}{R} + 2E(r) + \frac{1}{3}\Lambda R^2 \,, \tag{13}$$

where $M(r)$ is one more arbitrary, non-negative function. $M(r)/G$ is the *active gravitational mass* that generates the gravitational field. In curved space-times, this mass does not necessarily need to equal the integrated rest mass. In fact, depending on the sign of the curvature $E(r)$, $M(r)/G$ may be larger than ($E > 0$), smaller than ($E < 0$) or equal to ($E = 0$) the integrated rest mass (cf. Plebański & Krasiński 2006, Sect. 18.3). This is the general-relativistic analogue of the mass defect known from nuclear physics.

Equation (13) determines the time evolution of the areal radius $R(t, r)$ as a function of the mass $M(r)$, the curvature $E(r)$ and the cosmological constant Λ. After a separation of variables, Eq. (13) can directly be integrated, yielding

$$t - t_\mathrm{B}(r) = \int_0^{R(t,r)} \frac{1}{\sqrt{\frac{2M(r)}{\tilde{R}} + 2E(r) + \frac{\Lambda}{3}\tilde{R}^2}} \,\mathrm{d}\tilde{R} \,, \tag{14}$$

where the *bang time function* $t_\mathrm{B}(r)$ formally appears as yet another free function defining the time of the Big Bang singularity, $R\left[t_\mathrm{B}(r), r\right] = 0$. From this it follows that, generally, in LTB models, the age of the Universe can vary as a function of r, and consequently the Big Bang does not need to occur simultaneously. We discuss this property at greater length in Chap. 2.

Finally, by substituting Eqs. (6) and (10) into the last independent field equation (5), we can relate the active gravitational mass $M(r)$ to the local mass density ρ,

$$8\pi G\rho = \frac{2M'(r)}{R^2 R'} \,. \tag{15}$$

Equation (15) is of key importance for our approach presented in Chap. 2, where we explain an algorithm that determines the LTB solution given a local matter density profile.

To conclude this section, we repeat the final form of the LTB metric in comoving coordinates in the synchronous time gauge:

$$g = -\mathrm{d}t^2 + \frac{R'^2(t,r)}{1+2E(r)}\,\mathrm{d}r^2 + R^2(t,r)\left(\mathrm{d}\theta^2 + \sin^2\theta\,\mathrm{d}\phi^2\right) \ . \tag{16}$$

This solution of Einstein's field equations was first derived by Lemaître (1933), and later reconsidered by Tolman (1934) and Bondi (1947).

1.3 COMPARISON WITH FLRW MODELS

It is illustrative to compare the LTB metric (16) with the spatially isotropic and homogeneous FLRW metric, in particular to highlight distinctive features of radially inhomogeneous cosmological models that are important for the following sections.

First, we note that the homogeneous FLRW metric is a special case of the LTB metric. Defining $R(t,r) = a(t)r$ and $2E(r) = -kr^2$, we obtain

$$g = -\mathrm{d}t^2 + \frac{a^2(t)}{1-kr^2}\,\mathrm{d}r^2 + a^2(t)r^2\left(\mathrm{d}\theta^2 + \sin^2\theta\,\mathrm{d}\phi^2\right) \ , \tag{17}$$

which is the standard notation for the FLRW metric in reduced-circumference polar coordinates (Weinberg 2008). The FLRW limit thus emerges by requiring a homogeneous scale factor $a(t)$ ($\partial_r\, a(t) = 0$) and constant spatial curvature.

Next, we slightly rewrite Eq. (13) to introduce the transversal Hubble rate $H_\mathrm{T}(t,r)$, which describes the angular expansion rate of individual spherical shells,

$$H_\mathrm{T}(t,r) \equiv \frac{\dot{R}^2(t,r)}{R^2(t,r)} = \frac{2M(r)}{R^3(t,r)} + \frac{2E(r)}{R^2(t,r)} + \frac{\Lambda}{3} \ . \tag{18}$$

In the above-mentioned FLRW limit, we recover the well-known Friedmann equation (Friedmann 1922) from Eq. (18),

$$H^2\left[a(t)\right] \equiv \frac{\dot{a}^2(t)}{a^2(t)} = \frac{8\pi G}{3}\frac{\rho(t_0)}{a^3(t)} - \frac{k}{a^2(t)} + \frac{\Lambda}{3} \tag{19}$$

$$= H_0^2\left[\frac{\Omega_\mathrm{m}}{a^3(t)} + \frac{\Omega_k}{a^2(t)} + \Omega_\Lambda\right] \ , \tag{20}$$

where we implicitly chose the standard gauge $a(t_0) = 1$ and also inserted $M(r) = \frac{4}{3}\pi G\rho(t_0)r^3$, which results from Eq. (15) for a homogeneous matter density. Equations (18)-(20) highlight an important consequence of radial inhomogeneities: While the Hubble rate in FLRW models is spatially homogeneous and depends on time only, the Hubble rate in LTB models may additionally vary as a function of r. Fluctuations in $M(r)$, $E(r)$, or $t_\mathrm{B}(r)$ can induce variations of the spatial expansion rate.

Finally, we combine Eqs. (5) and (7) to construct a generalised acceleration equation (Enqvist 2008),

$$\frac{2}{3}\frac{\ddot{R}(t,r)}{R(t,r)} + \frac{1}{3}\frac{\ddot{R}'(t,r)}{R'(t,r)} = -\frac{4}{3}\pi G\rho(t,r) + \frac{\Lambda}{3} \ . \tag{21}$$

The total acceleration – which is the weighted sum of the angular and radial acceleration – is negative unless the cosmological constant dominates ($\Lambda > 4\pi G\rho$); this result is familiar from FLRW models. However, even in pure dust universes ($\Lambda = 0$), the radial acceleration may be positive $\left(\ddot{R}'(t,r) > 0\right)$ if the angular scale $R(t,r)$ is decelerating fast enough, and vice versa. This helps to illustrate that the idea of accelerated expansion is ambiguous in radially inhomogeneous models, which might be important for the correct interpretation of cosmological observations. We elaborate on this issue in more detail in Chap. 2.

1.4 RADIAL NULL GEODESICS AND DISTANCE-REDSHIFT RELATION

In the following chapter, we assume that the space-time geometry of the local Universe is well approximated by an LTB solution and investigate observable consequences of inhomogeneities in the radial matter density profile. To compare such LTB models with current cosmological data, we need to describe the propagation of light and construct a distance–redshift relation. For reasons to be clarified later, we only consider observers that are located at the symmetry centre at $r = 0$, where $R(t, r = 0) = 0$ at all times t. The distance–redshift relation of such observers is determined by the solution of incoming radial null geodesics ($\mathrm{d}\theta = \mathrm{d}\phi = 0$).

The following considerations reproduce the simple derivation given by Bondi (1947). A more general discussion of null geodesics, also valid for off-centre observers, can be found in Alnes & Amarzguioui (2006) or Brouzakis et al. (2007).

From the LTB metric (16), we can directly deduce that the time along radially incoming null geodesics ($\mathrm{d}s^2 = 0$) evolves according to

$$\frac{\mathrm{d}t}{\mathrm{d}r} = -\frac{R'(t,r)}{\sqrt{1+2E(r)}} \,. \tag{22}$$

Consider now two radial light rays emitted by the same source with a short time delay $\tau \ll 1$. Let $T(r)$ and $T(r) + \tau(r)$ denote the time coordinates along these rays. Equation (22) specified to the second, slightly delayed light ray reads

$$\frac{\mathrm{d}}{\mathrm{d}r}\left[T(r)+\tau(r)\right] = -\frac{R'\left[T(r)+\tau(r),r\right]}{\sqrt{1+2E(r)}} \tag{23}$$

$$= -\frac{R'\left[T(r),r\right]}{\sqrt{1+2E(r)}} - \frac{\dot{R}'\left[T(r),r\right]}{\sqrt{1+2E(r)}}\tau(r) + \mathcal{O}\left[\tau^2(r)\right] \,, \tag{24}$$

where we used a first order Taylor expansion in the second step. Taking into account that Eq. (22) for the first ray reads

$$\frac{\mathrm{d}T(r)}{\mathrm{d}r} = -\frac{R'\left[T(r),r\right]}{\sqrt{1+2E(r)}} \,, \tag{25}$$

we can rewrite Eq. (23) to the following differential equation:

$$\frac{\mathrm{d}\tau(r)}{\mathrm{d}r} = -\frac{\dot{R}'\left[T(r),r\right]}{\sqrt{1+2E(r)}}\,\tau(r) \,. \tag{26}$$

Equation (26) describes the evolution of time delays along the PNC – an effect that gives rise to the notion of a cosmological redshift.

Suppose that a central observer measures the frequency $\tau_{\rm obs}$ of a light ray originally emitted by a source at position r with the initial frequency $\tau(r)$. The redshift is then defined by

$$\frac{\tau_{\rm obs}}{\tau(r)} = [1 + z(r)] \ . \tag{27}$$

Radial differentiation of Eq.(27) yields the evolution of redshift along the PNC, and thus also the sought-for distance–redshift relation in LTB models,

$$\frac{1}{1+z(r)}\frac{\mathrm{d}z(r)}{\mathrm{d}r} = \frac{\dot{R}'\left[t(r),r\right]}{\sqrt{1+2E(r)}} \ . \tag{28}$$

Equations (22) and (28) can be numerically integrated. After solving for $t(r)$ and $z(r)$ on the PNC, we can numerically invert these relations to arbitrarily transform between t, r, and z. For instance, given a redshift z, we can infer the corresponding radius $r(z)$ and compute the time $t[r(z)]$ at which an incoming radial null geodesic was at this position.

Finally, as can be seen from the metric (16), the angular-diameter distance in LTB models is simply given by the areal radius function,

$$d_{\rm A}(z) = R(z) = R\left[t(z), r(z)\right] \ . \tag{29}$$

The luminosity distance then follows from the reciprocity theorem (Etherington 1933, 2007; Ellis 2009):

$$d_{\rm L}(z) = (1+z)^2\, d_{\rm A}(z) \ . \tag{30}$$

1.5 NUMERICAL SOLUTION OF EINSTEIN'S FIELD EQUATIONS

The previous section summarises the set of equations needed for determining the distance–redshift relation in LTB models. Obviously, the numerical integration of null geodesics requires the areal radius $R(t,r)$ (and its derivatives) along the PNC. Concerning this, it is perhaps important to note that Eq. (14) fixes $R(t,r)$ and all its derivatives as soon as $M(r)$, $E(r)$, Λ, and $t_{\rm B}(r)$ have been specified. Therefore, we detail the numerical solution of Eq. (14) for two particular cases in the following subsections.

1.5.1 *Without cosmological constant*

If $\Lambda = 0$, the integral in Eq. (14) can be solved parametrically and – depending on the sign of the curvature $E(r)$ – leads to an elliptic ($E < 0$), parabolic ($E = 0$) or hyberbolic ($E > 0$) evolution:

- Elliptic evolution: $E(r) < 0$

$$R(t,r) = -\frac{M(r)}{2E(r)}(1-\cos\eta)\ , \tag{31a}$$

$$\eta - \sin\eta = \frac{[-2E(r)]^{\frac{3}{2}}}{M(r)}\left[t - t_{\mathrm{B}}(r)\right]\ . \tag{31b}$$

- Parabolic evolution: $E(r) = 0$

$$R(t,r) = \left\{\frac{9}{2}M(r)\left[t - t_{\mathrm{B}}(r)\right]^2\right\}^{\frac{1}{3}}\ . \tag{32}$$

- Hyperbolic evolution: $E(r) > 0$

$$R(t,r) = \frac{M(r)}{2E(r)}(\cosh\eta - 1)\ , \tag{33a}$$

$$\sinh\eta - \eta = \frac{[2E(r)]^{\frac{3}{2}}}{M(r)}\left[t - t_{\mathrm{B}}(r)\right]\ . \tag{33b}$$

The elliptic evolution is special in the sense that it first starts to expand at $\eta = 0$, reaches the maximum areal radius $R_{\max}(r) = M(r)/|E|$ at $\eta = \pi$, and recollapses afterwards. In contrast, the other two solutions are ever-expanding, the parabolic solution being the limiting case between the elliptic and hyperbolic evolution. Again, we refer the interested reader to Chap. 18 of Plebański & Krasiński (2006) for more details on these solutions.

For numerical computations to be discussed later (cf. Sect. 2.4.2), it is useful to rewrite the parametric solutions as

$$t = t_{\mathrm{B}} + \frac{M}{(-2E)^{\frac{3}{2}}}\left[\arccos\left(1+\frac{2ER}{M}\right) - 2\sqrt{\frac{-ER}{M}\left(1+\frac{ER}{M}\right)}\right]\ ,$$
$$0 \leq \eta \leq \pi\ , \tag{34a}$$

$$t = t_{\mathrm{B}} + \frac{M}{(-2E)^{\frac{3}{2}}}\left[\pi + \arccos\left(-1-\frac{2ER}{M}\right) + 2\sqrt{\frac{-ER}{M}\left(1+\frac{ER}{M}\right)}\right]\ ,$$
$$\pi \leq \eta \leq 2\pi\ , \tag{34b}$$

for the expanding and collapsing elliptic cases, and

$$t = t_{\mathrm{B}} + \frac{M}{(2E)^{\frac{3}{2}}}\left[2\sqrt{\frac{ER}{M}\left(1+\frac{ER}{M}\right)} - \operatorname{arcosh}\left(1+\frac{2ER}{M}\right)\right] \tag{35}$$

for the hyperbolic case. Equations (34) and (35) can be numerically unstable in the near parabolic limit ($|E| \ll 1$). In this case, we use an inverse series expansion as explained in Appendix B of Hellaby & Krasiński (2006).

Finally, we note that the parametric solutions (31) - (33) can be combined to derive an analytic expression for the radial derivative of the areal radius function,

$$R' = \left(\frac{M'}{M} - \frac{E'}{E}\right) R + \left[\left(\frac{3}{2}\frac{E'}{E} - \frac{M'}{M}\right)(t - t_\mathrm{B}) - t'_\mathrm{B}\right] \dot{R} \,. \tag{36}$$

This relation, together with the radial derivative of Eq. (13),

$$\dot{R}' = \frac{1}{\dot{R}} \left[\left(\frac{M'R - MR'}{R^2}\right) + E'\right] \,, \tag{37}$$

allows us to analytically compute R' and $\dot{R}'$, which renders the numerical integration of radial null geodesics more efficient.

1.5.2 *With cosmological constant*

If $\Lambda > 0$, no general parametric solution exists. Instead, the elliptic integral in Eq. (14) can only be computed numerically, which for certain parameter combinations quickly turns into a difficult numerical problem involving singularities, slow convergence (if at all) and poor precision.

However, Valkenburg (2012) found an elegant method to transform integrals such as the one in Eq. (14) to a special class of elliptic integrals, which can efficiently be computed with specific numerical algorithms. To illustrate this method, we sketch one particular transformation here. The readable work of Valkenburg (2012) contains more examples, extensive derivations and many useful details (such as asymptotic expansions) concerning the numerical implementation.

Let us first repeat Eq. (14) in the new form

$$t - t_\mathrm{B}(r) = \sqrt{\frac{3}{\Lambda}} \int_0^R \frac{\sqrt{\tilde{R}}}{\sqrt{(\tilde{R} - y_1)(\tilde{R} - y_2)(\tilde{R} - y_3)}} \, \mathrm{d}\tilde{R} \,, \tag{38}$$

where we simple rewrote the polynomial in the denominator to

$$2M(r) + 2E(r)\tilde{R} + \frac{\Lambda}{3}\tilde{R}^3 = \frac{\Lambda}{3}(\tilde{R} - y_1)(\tilde{R} - y_2)(\tilde{R} - y_3) \,. \tag{39}$$

The complex roots y_i of Eq. (39) should be computed with specific formulae for depressed[1] cubic functions that were arranged to minimise roundoff errors (Press 2007). If required, the Newton-Raphson method can be used to further improve the numerical accuracy of the y_i's.

1 A depressed cubic function is a cubic function without a quadratic term.

Next, we subsequently perform the substitutions $\tilde{R} \to c = \frac{1}{\tilde{R}}$ and $c \to b = c - \frac{1}{R}$, before we arrive at the final result:

$$t - t_{\mathrm{B}}(r) = \sqrt{\frac{3}{\Lambda}} \int_0^R \frac{\sqrt{\tilde{R}}}{\sqrt{(\tilde{R} - y_1)(\tilde{R} - y_2)(\tilde{R} - y_3)}} \, \mathrm{d}\tilde{R} \tag{40}$$

$$= \sqrt{\frac{3}{\Lambda}} \int_{\frac{1}{R}}^{\infty} \frac{c^{-\frac{5}{2}}}{\sqrt{(\frac{1}{c} - y_1)(\frac{1}{c} - y_2)(\frac{1}{c} - y_3)}} \, \mathrm{d}c \tag{41}$$

$$= \sqrt{\frac{3}{\Lambda}} \frac{(-1)^{-\frac{3}{2}}}{\sqrt{y_1 y_2 y_3}} \int_{\frac{1}{R}}^{\infty} \frac{1}{c\sqrt{(c - \frac{1}{y_1})(c - \frac{1}{y_2})(c - \frac{1}{y_3})}} \, \mathrm{d}c \tag{42}$$

$$= \sqrt{\frac{3}{\Lambda}} \frac{(-1)^{-\frac{3}{2}}}{\sqrt{y_1 y_2 y_3}} \int_0^{\infty} \frac{1}{(b + \frac{1}{R})\sqrt{\prod_{m=1}^{3}(b + \frac{1}{R} - \frac{1}{y_m})}} \, \mathrm{d}b \tag{43}$$

$$= \frac{2}{\sqrt{3\Lambda}} \frac{(-1)^{-\frac{3}{2}}}{\sqrt{y_1 y_2 y_3}} R_{\mathrm{J}}\left(\frac{1}{R} - \frac{1}{y_1}, \frac{1}{R} - \frac{1}{y_2}, \frac{1}{R} - \frac{1}{y_3}, \frac{1}{R}\right) . \tag{44}$$

In Eq. (44), we identified the previous integral with the special function R_{J}, which belongs to the set of Carlson's symmetric forms. This canonical set of elliptic integrals can be solved using iterative algorithms, which are fast, robust, and quickly converge with machine precision (Carlson 1995).

Valkenburg (2012) showed that similar transformations lead to expressions for R' and $\dot{R}$ in terms of Carlson's symmetric forms. We implemented these formulae in our numerical code, which enables us to quickly compute derivatives of the areal radius with machine precision. Again, this is particularly important for the efficient integration of null geodesics.

2

PROBING SPATIAL HOMOGENEITY WITH LTB MODELS

ABSTRACT

Do current observational data confirm the assumptions of the cosmological principle, or is there statistical evidence for deviations from spatial homogeneity on large scales? To address these questions, we developed a flexible framework based on LTB models with synchronous Big Bang. We expanded the (local) matter density profile in terms of flexible interpolation schemes and orthonormal polynomials. A Monte Carlo technique in combination with recent observational data was used to systematically vary the shape of these profiles. In the first part of this chapter, we reconsider giant LTB voids without dark energy to investigate whether extremely fine-tuned mass profiles can reconcile these models with current data. While the local Hubble rate and supernovae can easily be fitted without dark energy, however, model-independent constraints from the Planck 2013 data require an unrealistically low local Hubble rate, which is strongly inconsistent with the observed value; this result agrees well with previous studies. In the second part, we explain why it seems natural to extend our framework by a non-zero cosmological constant, which then allows us to perform general tests of the cosmological principle. Moreover, these extended models facilitate exploring whether fluctuations in the local matter density profile might potentially alleviate the tension between local and global measurements of the Hubble rate, as derived from Cepheid-calibrated type Ia supernovae and CMB experiments, respectively. We show that current data provide no evidence for deviations from spatial homogeneity on large scales. More accurate constraints are required to ultimately confirm the validity of the cosmological principle, however.

The contents of this chapter were published in Redlich et al. (2014a).

2.1 INTRODUCTION

While the discovery of the (apparently) accelerated expansion of the Universe established a non-vanishing dark energy contribution in the framework of the standard cosmological model (Riess et al. 1998; Perlmutter et al. 1999), these observations also motivated many researchers to question the theoretical foundations the standard model is built upon. One of these foundations is the cosmological principle, which asserts that our Universe is spatially isotropic and homogeneous when averaged over sufficiently large scales ($\gtrsim 100\,\mathrm{Mpc}$). Statistical isotropy about our position has been confirmed by the remarkable uniformity of the CMB spectrum (Bennett et al. 2013;

Planck Collaboration et al. 2013). In contrast, statistical homogeneity on large scales (i. e. Gpc scales) is hard to confirm, mainly because it is difficult to distinguish a temporal from a spatial evolution on the past light cone (see Maartens 2011; Clarkson 2012, for reviews).

This uncertainty inspired many to study inhomogeneous cosmologies (see Marra & Notari 2011; Bolejko et al. 2011, for comprehensive reviews), including non-Copernican models that explain the apparent accelerated expansion of the Universe by means of radial inhomogeneities without requiring any form of dark energy. The basic idea behind these alternative models is quite simple because we know from observations and numerical simulations that the large-scale structure of the Universe consists of filaments and voids (Hogg et al. 2005; Springel et al. 2005; Labini 2010; Einasto et al. 2011b,a; Labini 2011; Scrimgeour et al. 2012; Clowes et al. 2013; Nadathur 2013; Nadathur & Hotchkiss 2014; Sutter et al. 2014; Melchior et al. 2014). Einstein's General theory of Relativity tells us that the expansion rate in space-time regions with lower matter density should be higher than in regions with a higher matter density. If we were to live in a large-scale under-density, the local expansion rate around us would be higher than the average expansion rate in the background. Light-rays propagating from distant sources to us – the observer – would therefore feel an accelerated expansion rate along their path. In comparison to the standard cosmological model, these scenarios hence replace a cosmic acceleration in time (due to dark energy) by a spatially varying expansion rate.

One particular, exact inhomogeneous cosmological model that has extensively been studied is the LTB model. The spatial hypersections of LTB models are spherically symmetric only about one point, and to conserve the remarkable uniformity of the CMB spectrum, we would have to live very close to the symmetry centre (Alnes & Amarzguioui 2006; Foreman et al. 2010). Interpreted as a faithful representation of the Universe, these void models breach the Copernican principle and require a tremendous fine-tuning of our position in the Universe. The plausibility of such scenarios is therefore more than dubious (see Célérier 2012, however, for interesting thoughts). The standard cosmological model also requires significant fine-tuning, however, which gives rise to controversial philosophical discussions (see e.g. Durrer & Maartens 2008; Amendola & Tsujikawa 2010). In this chapter, we simply demonstrate that a quite general class of LTB void models without dark energy is inconsistent with current observational data, which allows us to set the philosophical discussion aside.

The vast literature on inhomogeneous cosmologies – in particular LTB models – is summarised in the review articles by Bolejko et al. (2011) and Marra & Notari (2011), which allows us to only focus on the aspects that are particularly relevant for this chapter. For reasons to be clarified later, we only discuss LTB models with synchronous Big Bang throughout, meaning that the bang time function is constant and the Universe has the same global age everywhere. In the first part of this chapter, we additionally set the cosmological constant to zero.

It has long been known that LTB models without dark energy can easily fit supernovae, explaining the apparent acceleration of the Universe by a Gpc-scale void around us (Célérier 2000). In addition, these models can be tuned to fit the small-angle CMB spectrum (Zibin et al. 2008). However, most recent studies agree that a good fit

to the CMB requires an unrealistically low local Hubble rate of $H_0 \lesssim 60\,\mathrm{km\,s^{-1}\,Mpc^{-1}}$ (Biswas et al. 2010; Moss et al. 2011; Bull et al. 2012; Zumalacárregui et al. 2012), which is strongly inconsistent with the observed value of $H_0 = (73.8 \pm 2.4)\,\mathrm{km\,s^{-1}\,Mpc^{-1}}$ measured with Cepheid-calibrated type Ia supernovae (Riess et al. 2011). We here already anticipate that we shall finally arrive at the very same conclusion.

Nevertheless, we believe that our work meaningfully complements the current literature mainly for the following reasons: For the first time, we compare LTB models with the latest Planck 2013 data (Planck Collaboration et al. 2013). This is interesting because the Planck data favour a lower Hubble rate than previous CMB experiments. Moreover, we advocate the use of a recently developed technique for analysing CMB spectra in a model-independent manner, which is particularly useful for investigating alternative cosmological models. Secondly, most recent studies have assumed certain functional forms for the mass or curvature profile of LTB models that may be considered characteristic for voids. These empirical parametrisations might simply be too restrictive, however, and certainly impose artificial constraints on the models when performing maximum-likelihood estimates. To our knowledge, only Zibin et al. (2008) and Moss et al. (2011) considered more flexible spline interpolations for the mass profile of LTB voids.

We extend these ideas and introduce alternative, flexible parametrisations of the local matter density profile, aiming to impose as little a priori constraints on the detailed form as possible. A MC technique in combination with recent observational data allows us to systematically vary the matter density profiles of LTB models and derive statistical constraints on the favoured profile shapes. Moreover, we demonstrate that even the enormous flexibility of radially fine-tuned models does not suffice to simultaneously fit the observed local Hubble rate and the CMB.

After this detailed discussion, we provide simple theoretical arguments that explain why not even heavily fine-tuned LTB models without dark energy can be reconciled with current observational data. We then discuss why it seems most natural to extend our models by a non-zero cosmological constant. The resulting ΛLTB models constitute a powerful framework for conducting general tests of the cosmological principle (Marra & Pääkkönen 2010). Recently, Valkenburg et al. (2014) proposed a new technique, based on ΛLTB models, for placing constraints on violations of the Copernican principle. Furthermore, by marginalising over all possible inhomogeneities, these authors derived first observational constraints on the cosmological constant that are free of the usual homogeneity prior (see also Marra et al. 2013b, for a similar ansatz). Marra et al. (2013a) used ΛLTB models to investigate whether fluctuations in the local matter density profile can alleviate the well-known discrepancy between the high local Hubble rate as measured by Riess et al. (2011) and the lower one derived from the Planck 2013 data. Obviously, our previously developed, flexible parametrisations of the local matter density profile in combination with a MC technique constitute an ideal tool for conducting similar studies. Again, by imposing (almost) no a priori constraints on the detailed shape of the density profiles, our approach is more general than previous works on this field.

The structure of this chapter is as follows: In Sect. 2.2, we explain our general ansatz for the metric of a Universe that may radially be inhomogeneous on large

scales. Section 2.3 describes the observational data used to constrain LTB models and also discusses some ambiguities that have to be taken into account when fitting non-standard cosmological models to these data. In Sect. 2.4, we introduce flexible parametrisations of the local matter density profile and describe the algorithm that allows us to statistically constrain the shape of the profile functions. Section 2.5 summarises our main results of a long series of tests, comparing numerous LTB models without cosmological constant with different combinations of observational data. In Sect. 2.6, we provide some simple theoretical arguments that explain our empirical results from Sect. 2.5. We then extend our models by a non-zero cosmological constant and discuss general probes of the cosmological principle in Sect. 2.7. Finally, we present our conclusions in Sect. 2.8.

2.2 LTB ANSATZ FOR THE METRIC

We make the following simplified ansatz for the metric of the observable Universe: We maintain the standard inflationary paradigm and assume that the early Universe was highly homogeneous at least until the time of decoupling. Given the remarkable uniformity of the CMB spectrum, we assume that spherical symmetry about our position was conserved until the present epoch. However, we breach the cosmological principle by allowing a fine-tuned, radially inhomogeneous matter density profile on large scales. As an example, we could envisage to live at the centre of a Gpc-scale void that emerged from an – admittedly extreme – under-density of the primordial matter distribution.

Mathematically, this can be realised by describing the local Universe around us with a spherically symmetric, but radially inhomogeneous LTB model that is asymptotically embedded in a homogeneous FLRW background. As described in Chap. 1, the LTB model is a dust solution of Einstein's field equations with zero pressure ($p = 0$). This should be an excellent approximation because the local Universe we observe is also a Universe at a late evolutionary epoch, and at this stage, pressure should be completely negligible for describing the large-scale matter distribution. Following the findings of previous work (Biswas et al. 2010; Zumalacárregui et al. 2012), we generally allow the FLRW background to be spatially curved to improve the fit to the CMB.

As explained in Sect. 1.2, LTB models generally depend on three functions: the bang time function $t_{\mathrm{B}}(r)$, the curvature function $E(r)$, and the mass function $M(r)$. However, the metric and all formulae in Sect. 1.2 are invariant by diffeomorphism symmetry, including coordinate transformations of the form $r = f(r')$. This gauge freedom can be used to eliminate one function, implying that the physical evolution of LTB models is fully determined by only two free functions.

In general, the bang time function $t_{\mathrm{B}}(r)$ can be an arbitrary function of r, which means that the Big Bang does not need to occur synchronously, as in FLRW models. It can be shown, however, that fluctuations in the bang time function can be identified with decaying modes in linear perturbation theory (Silk 1977; Zibin 2008). Thus, going back in time, these decaying modes would correspond to inhomogeneities at early times. To conserve the remarkable homogeneity of the CMB spectrum, fluctuations in the age of the Universe must have been smaller than a few hundred years (Bolejko

2009), which is substantially smaller than the present age of the Universe ($t_{\mathrm{B}}(r) \ll t$). Complying with our initial assumption of a homogeneous, early Universe (even in regions from which we do not observe CMB photons), we can thus safely neglect the bang time function and assume that it is zero, $t_{\mathrm{B}}(r) = \mathrm{const} = 0$. This assumption is particularly important for the CMB analysis described in Sect. 2.3.3.

This leaves us with only one arbitrary function. In Sect. 2.4.2, we describe in detail how the curvature and mass functions can be derived from a matter density profile at a given time.

2.3 OBSERVATIONAL DATA

This section outlines what observational data we used to constrain LTB models. In this context, two complications have to be considered.

Firstly, many cosmological data sets are routinely reduced under the implicit assumption that our Universe is, on large scales, properly described by an FLRW metric. When fitting alternative cosmological models to these data, special care has to be taken that only model-independent observational constraints are used.

Secondly, linear perturbation theory in LTB models is substantially more complicated than in FLRW models. This is mainly because scalar and tensorial perturbations can couple on inhomogeneous backgrounds. Although there has been great progress in developing a gauge-invariant linear perturbation theory for LTB models, the problem has yet to be fully solved (Zibin 2008; Clarkson et al. 2009; February et al. 2014). To be conservative, we can therefore only use observables that do not depend on the details of structure formation.

Perhaps we should emphasise this limitation of the present work. The current state of the theory only allows us to explore constraints on the global structure of the smooth, unperturbed space-time geometry on large scales. We cannot yet realistically model the evolution of linear perturbations in radially inhomogeneous space-times because we lack proper theoretical tools for predicting the statistical properties of the perturbed matter density field, for example. Observations of the local matter distribution, the large-scale structure (including voids and filaments), cluster number counts, or galaxy-galaxy correlation functions can therefore not yet be taken into account for constraining the underlying space-time geometry. We also have to exclude constraints from weak-lensing spectra or baryonic acoustic oscillations, for instance, which are widely used to constrain homogeneous and isotropic cosmologies. We are currently working on advancing linear perturbation theory in LTB models and will include some of the observables listed above in future work.

The lack of linear perturbation theory is not important for Sect. 2.5, where we show that only constraints from the local Hubble rate and the CMB are sufficient to rule out LTB models without cosmological constant. For the general probe of the cosmological principle presented in Sect. 2.7, it would certainly be desirable to have more data. On the other hand, Valkenburg et al. (2014) showed that the cosmological observables used in this work are currently the most constraining.

2.3.1 *Local Hubble rate*

Riess et al. (2011) used a nearby sample $(0.023 < z < 0.1)$ of Cepheid-calibrated type Ia supernovae to measure the local Hubble rate with a remarkable precision:

$$H_0 = (73.8 \pm 2.4)\,\mathrm{km\,s^{-1}\,Mpc^{-1}}\,. \tag{45}$$

Up to now, this is probably the most accurate determination of the local expansion rate of the Universe. Although Efstathiou (2014) recently reanalysed the data from Riess et al. (2011) and proposed a corrected, slightly lower value of $H_0 = (72.5 \pm 2.5)\,\mathrm{km\,s^{-1}\,Mpc^{-1}}$; we used the original measurement to constrain our models because the proposed corrections are not significant for our main conclusions.

One essential property of LTB models is their radially dependent expansion rate. More precisely, we can define a longitudinal Hubble rate, $H_\mathrm{L}(t,r) = \dot{R}'(t,r)/R'(t,r)$, which describes the expansion rate along the radial direction, and a transversal Hubble rate, $H_\mathrm{T}(t,r) = \dot{R}(t,r)/R(t,r)$, which describes the expansion rate of the individual spherical shells (cf. Sect. 1.3). It is therefore not a priori clear how LTB models should be compared with the above-mentioned measurement.

To mimic the procedure of Riess et al. (2011), we used the following approach: Independent of the cosmological model, the (local) luminosity distance can be considered an analytic function of redshift z and hence expanded in a Taylor series $(z \ll 1)$,

$$d_\mathrm{L}(z) = \frac{c}{H_0}\left[z + \frac{1}{2}\,(1 - q_0)\,z^2 - \frac{1}{6}\,(1 - q_0 - 3q_0^2 + j_0)\,z^3\right] + \mathcal{O}(z^4)\,, \tag{46}$$

where q_0 and j_0 are the deceleration parameter and the jerk, respectively. Like Riess et al. (2011), we fixed these two parameters to $q_0 = -0.55$ and $j_0 = 1$. To compute the *effective* local Hubble rate of a specific LTB model, we first tabulated the luminosity distance $d_\mathrm{L}(z_i)$ (cf. Eq. (30)) at N equidistantly spaced steps in the considered redshift range, $0.023 < z_1 < \ldots < z_N < 0.1$, and then calculated the best-fitting (least-squares) Hubble rate H_LS through these data points using Eq. (46). The deviation from the observed value is then quantified with a simple chi-square,

$$\chi^2_{H_0} = \frac{(H_\mathrm{LS} - H_0)^2}{\sigma^2_{H_0}} \qquad \left(\sigma_{H_0} = 2.4\,\mathrm{km\,s^{-1}\,Mpc^{-1}}\right)\,. \tag{47}$$

Using this approach, we defined an averaged, effective local Hubble rate for LTB models that closely mimics the one measured with observed type Ia supernovae.

2.3.2 *Supernovae*

To constrain the shape of the luminosity distance at even higher redshifts, we used the Union2.1 compilation released by the Supernova Cosmology Project (Suzuki et al. 2012). This catalogue contains 580 uniformly analysed type Ia supernovae and extends out to redshift $z \sim 1.5$. Currently, the Union2.1 compilation is the largest, and most recent, publicly available sample of standardized type Ia supernovae.

Although the shape of type Ia supernovae light-curves is empirically well understood, their absolute magnitude is essentially unknown and needs to be calibrated. Samples like the Union2.1 compilation are therefore reduced by fixing the Hubble rate to an arbitrary value. It is important to remove this artificial constraint from the data when fitting cosmological models. This can either be achieved by analytically marginalizing over the assumed Hubble rate – or, equivalently, the absolute magnitude – (see Bridle et al. (2002) or Appendix C.2 of Biswas et al. (2010)), or by using the elegant weight matrix formalism described in the appendix of Amanullah et al. (2010). The weight matrix is constructed from the full covariance matrix with systematics (e.g. host mass correction) and incorporates the marginalization over various nuisance parameters. In particular, the marginalization over the Hubble rate is included. We use the weight matrix formalism to perform likelihood estimates in the following sections.

Finally, we note that several authors argued that supernova samples reduced with the SALT-II light-curve fitter from Guy et al. (2007) are systematically biased towards the standard cosmological model and tend to disfavour alternative cosmologies (Hicken et al. 2009; Kessler et al. 2009; Smale & Wiltshire 2011). The Union2.1 compilation was reduced with the SALT-II fitter, and hence this potential penalty would also affect the goodness-of-fit of LTB models. However, we can safely neglect this problem for mainly two reasons. Firstly, we did not conduct a detailed, statistical comparison (e.g. Bayesian model comparison) between the standard cosmological model and LTB models here, and therefore the small, systematic corrections are irrelevant for our main conclusions. Secondly, and more importantly, we demonstrate that the supernova data do not impose tight constraints on LTB models anyway. Instead, supernovae can easily be fitted with a variety of different density profiles and certainly do not cause the tension between observations and LTB models that we focus on.

2.3.3 *Cosmic microwave background*

The standard approach for analysing CMB spectra is inherently based on the assumption of a spatially isotropic and homogeneous Universe (Bennett et al. 2013; Planck Collaboration et al. 2013). Primary anisotropies are calculated by numerically solving the Boltzmann equations on an FLRW background (Lewis et al. 2000; Lesgourgues 2011). Secondary anisotropies are caused by different forms of interactions between cosmic structures and the CMB photons after the time of decoupling, such as the late integrated Sachs-Wolfe (ISW) effect or rescattering during reionisation. As such, all these processes depend on the details of structure formation and are commonly modelled using perturbation theory in FLRW models. It is obvious that our ansatz for the metric in Sect. 2.2 strongly violates these usual assumptions. How then can we self-consistently use CMB spectra to constrain LTB models?

We recall that we wish to retain the inflationary paradigm and assume that the early Universe is highly homogeneous. This means that, even in our approach, the early Universe can effectively be described by a FLRW metric. Thus, the modelling of primary CMB anisotropies does not differ from the standard approach at least until the time of decoupling. This was also the motivation for excluding variations

of the bang time function $t_B(r)$ from Eq. (14). If we were to drop the assumption of a homogeneous early Universe, we would have to develop a general relativistic formalism for calculating CMB anisotropies on inhomogeneous backgrounds. Clearly, this would go far beyond the scope of this work.

Properly treating secondary CMB anisotropies in LTB models is, however, more complicated because linear perturbation theory is still being developed and cannot yet be used to calculate these secondary effects. We can circumvent this problem by following the elegant work of Vonlanthen et al. (2010), which describes a method for analysing the CMB in a manner that is as independent as possible of late-time cosmology. To this end, the authors begin with identifying the three dominant imprints that the late cosmological model leaves on the observed CMB spectrum. Firstly, CMB photons are lensed as they traverse non-linear structures. The late ISW effect dominates the CMB spectrum on large scales ($l \lesssim 40$). Consequently, low multipoles strongly depend on the detailed properties of the late cosmological model. Secondly, the overall amplitude of the CMB spectrum at $l \gg 40$ is reduced by scattering processes during the epoch of reionisation. This suppression is usually parametrised by the factor $e^{-2\tau}$, where τ is the reionisation optical depth. Thirdly, the angular-diameter distance to the last scattering surface (LSS) determines the angular scales of the acoustic peaks. This is a simple projection effect. Variations of the angular-diameter distance shift the CMB spectrum in multipole space.

If large scales ($l \lesssim 40$) are excluded from the CMB analysis, the dominant perturbations of the primordial CMB spectrum due to the late cosmological model can therefore be parametrised by a rescaling factor α of the global amplitude and a shift parameter β. Rephrased more mathematically, the expansion coefficients of the CMB power-spectrum in multipole space transform as $C_l \to \alpha C_{\beta l}$.

This simple approximation is already astonishingly accurate for large parts of the CMB spectrum. But the crucial point is that this insight allowed Vonlanthen et al. (2010) to encode unknown secondary effects in carefully chosen nuisance parameters (e.g. the global amplitude of the CMB spectrum). These additional parameters can be built into standard parameter estimation codes used for analysing CMB spectra. To derive minimal constraints that do not depend on the detailed properties of the late cosmological model, one simply has to marginalise over these newly introduced nuisance parameters.

Except for excluding high multipoles ($l > 800$) from the analysis, Vonlanthen et al. (2010) neglected the impact of gravitational lensing on the CMB spectrum. This was well justified given the accuracy of CMB experiments at the time of publishing. Motivated by the improved accuracy of modern CMB experiments, however, Audren et al. (2013a) extended the original method of Vonlanthen et al. (2010) by introducing a new technique for additionally marginalising over the CMB lensing contamination at all multipole orders. Initially, we used this advanced technique in combination with the publicly available parameter estimation code `Monte Python` (Audren et al. 2013b) to derive model-independent constraints from the latest Planck data (Planck Collaboration et al. 2013). While we prepared this manuscript, Audren (2014) published another slight refinement of their own method and also applied it to the Planck 2013 data. We therefore used the results published in Audren (2014) to estimate likelihoods in the

Table 1: Model-independent constraints from the Planck 2013 data published by Audren (2014). $\omega_b = \Omega_b h^2$ and $\omega_c = \Omega_c h^2$ denote the physical baryon and cold dark matter densities, respectively. $d_A(z_*)$ is the angular-diameter distance to the surface of last scattering.

$100\, w_b$	w_c	$d_A(z_*)$ [Mpc]
2.243 ± 0.040	0.1165 ± 0.0037	12.80 ± 0.068

following sections. The relevant model-independent constraints including one-sigma errors are summarised in Table 1.

Finally, we need to explain how LTB models can actually be fitted to these constraints. We begin by noting that the redshift of decoupling z_* generally is a function of the physical matter densities w_b and w_c. Assuming standard radiation content, however, this dependence is only weak (Hu & Sugiyama 1996). For simplicity, we can thus fix the decoupling redshift to $z_* = 1090$. Following previous works (see e.g. Zibin et al. 2008; Biswas et al. 2010; Moss et al. 2011, for detailed descriptions), we used an effective FLRW observer approach for computing the angular-diameter distance $d_A(z_*)$ to the LSS: Radial null geodesics are numerically integrated in LTB models only up to an embedding redshift z_b. This redshift has to be chosen such that the LTB models are already sufficiently homogeneous (i. e. the gravitational shear $\sigma^2 = \frac{2}{3}(H_L - H_T)$ vanishes) and radiation is still negligible. Typically, $z_b \approx 150$ fulfils these criteria.

After reaching this embedding redshift, we continued to compute the distance-redshift relation in an effective FLRW background model up to the decoupling redshift $z_* = 1090$. The effective FLRW model was chosen such that a fictitious observer in this background model would observe the same CMB spectrum. This approach is beneficial because (1) solving the distance-redshift relation in FLRW models is computationally substantially cheaper, and (2) radiation can be included. Lastly, the appropriately scaled matter densities and the calculated angular-diameter distance can be compared with the model-independent constraints from Table 1 using a simple chi-square.

2.3.4 *Kinetic Sunyaev-Zel'dovich*

Cosmic microwave background photons traversing galaxy clusters interact with the hot intra-cluster gas through inverse Compton scattering. These interactions cause the Sunyaev-Zel'dovich effect, which manifests itself by characteristic distortions of the energy spectrum of the rescattered photons. The dominant contribution in galaxy clusters is due to the thermal Sunyaev-Zel'dovich effect (Sunyaev & Zeldovich 1970, 1972): thermal energy is transferred from the hot intra-cluster gas to the CMB photons, causing a redistribution of photons from lower to higher energy states. A second-order contribution is due to the kinetic Sunyaev-Zel'dovich (kSZ) effect (Sunyaev & Zeldovich 1980): galaxy clusters moving with a non-zero peculiar velocity with respect to the rest frame of the CMB observe an anisotropic CMB spectrum with non-zero dipole moment. This dipole induces a characteristic shift in the spectrum

of the reflected CMB photons, which is similar to the relativistic Doppler effect. In principal, the kSZ effect of galaxy clusters can therefore be used to measure their peculiar velocities relative to the CMB.

As was first shown by García-Bellido & Haugbølle (2008), the kSZ effect can be used as a powerful probe of radially inhomogeneous LTB models. To understand this, we recall that LTB models are isotropic only about the symmetry centre at the coordinate origin. Off-centre observers therefore generally see an anisotropic CMB spectrum (see Alnes & Amarzguioui 2006, for detailed calculations). To first order, the anisotropy can be approximated as a pure dipole, which because of the symmetry of the problem is aligned along the radial direction. This effect is depicted in Fig. 1, which shows an off-centre galaxy cluster that rescatters CMB photons that arrive from the LSS.

The extreme redshifts (as seen from the galaxy cluster) are observed along the radial direction, for CMB photons with redshift z_{in} that propagated through the centre of the inhomogeneity and, in the opposite direction, for CMB photons with redshift z_{out} arriving from outside. In the case of a giant void scenario, for instance, photons arriving from inside the void travelled the longest distance through an underdense region. Consequently, they also spent the longest time in a space-time region with a higher expansion rate, so that their redshift z_{in} reaches the highest possible value. Vice versa, CMB photons arriving from outside the void exhibit the lowest redshift z_{out}.

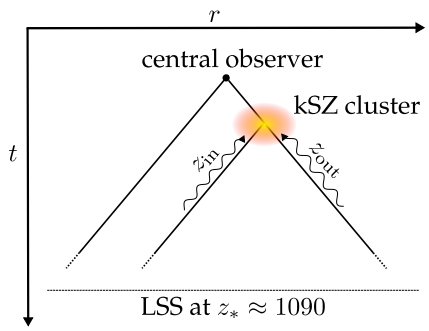

Figure 1: Apparent kinetic Sunyaev-Zel'dovich (kSZ) effect of off-centre galaxy clusters in radially inhomogeneous LTB models. The redshift z_{in} of CMB photons that propagated through the centre of the inhomogeneity generally differs from the redshift z_{out} of CMB photons that arrived from outside.

Note that the kSZ effect described here is only an apparent kSZ effect; it is not caused by real peculiar motions of the galaxy clusters. Instead, the effect only appears because the space-time geometry around off-centre observers is anisotropic. Note also that the kSZ effect has a distinguished feature in comparison with most other cosmological probes. The galaxy clusters act as mirrors for CMB photons, reflecting radiation from all spatial directions. By analysing the spectrum of the reflected light, we can therefore extract information about space-time regions that would otherwise be inaccessible. In this sense, by measuring the difference between the redshift z_{in} and z_{out}, the kSZ effect allows us to (indirectly) look inside our PNC (cf. Fig. 1).

As already mentioned, to first order, the anisotropy observed by off-centre galaxy clusters can be approximated as a pure dipole. This approximation is sufficiently accurate as long as the effective size of the LTB inhomogeneity on the sky, as observed by the galaxy cluster, is larger than $\sim 2\pi$ (Alnes & Amarzguioui 2006). The amplitude of the dipole is then given by

$$\beta = \frac{v}{c} = \frac{\Delta T}{T} = \frac{z_{\text{in}} - z_{\text{out}}}{2 + z_{\text{in}} + z_{\text{out}}} \,. \tag{48}$$

Measurements of the kSZ effect of individual galaxy clusters are extremely difficult and suffer from low signal-to-noise ratios. Current data exhibit very large errors

and therefore still need to be considered premature. However, even though the uncertainties are huge, García-Bellido & Haugbølle (2008) and Bull et al. (2012) showed that the currently available measurements already place tight constraints on the depth and radial size of Gpc LTB voids. In this work, we use the kSZ data of the nine galaxy clusters compiled by García-Bellido & Haugbølle (2008), assuming a conservative scatter of $\sigma_{\rm pv} = 1600\,{\rm km\,s^{-1}}$ and zero systematic shift, $v_{\rm sys} = 0$; see García-Bellido & Haugbølle (2008) and references therein for a detailed discussion of the data, sources of errors, and the modelling of the likelihood.

To compute the expected kSZ effect for a given galaxy cluster, we first determined the cluster coordinates $(t_{\rm cl}, r_{\rm cl}, z_{\rm cl})$ on the PNC of the central observer. Starting from this position, we then solved for ingoing and outgoing radial null geodesics by numerically integrating Eqs. (22) and (28) up to the LSS. This procedure yields the two redshifts $z_{\rm in}$ and $z_{\rm out}$, which quantify the CMB dipole as seen by the off-centre galaxy cluster.

2.4 MONTE CARLO APPROACH FOR CONSTRAINING THE LOCAL DENSITY PROFILE

Most studies published so far have assumed certain functional forms for either the mass profile or the curvature profile of LTB models that may be considered characteristic for voids (see e.g. Garcia-Bellido & Haugbølle 2008; Bolejko & Wyithe 2009; Biswas et al. 2010, for typical profiles). Of course, these empirical functional forms impose artificial constraints on the models when performing maximum likelihood estimates.

Our approach here is different because we parametrise the matter density profile of LTB models as flexibly as possible, imposing few a priori constraints on its detailed shape. To derive statistical constraints, we then use a parameter estimation code to systematically vary the density profile. We wish to determine the shape of the favoured profile, and also how tight the constraints on the detailed shape are. We also investigate whether highly flexible profiles allow us to mitigate the reported tension between measurements of the local Hubble rate and the CMB data (Biswas et al. 2010; Moss et al. 2011; Bull et al. 2012; Zumalacárregui et al. 2012). To this end, we proceed by first discussing our choices for the parametrisation of the local density profile, continue with the algorithm that allows us to derive LTB models from these profiles, and conclude this section by explaining some details of the parameter estimation technique.

2.4.1 *Flexible models for the local density profile*

Broadly speaking, we have two options to parametrise the local density profile in the most flexible way. We can represent the density profile by a general interpolation scheme, or alternatively decompose the void profile function into a series of appropriately chosen, orthonormal basis functions of the radial coordinate. After some initial testing, we decided to use the following parametrisations:

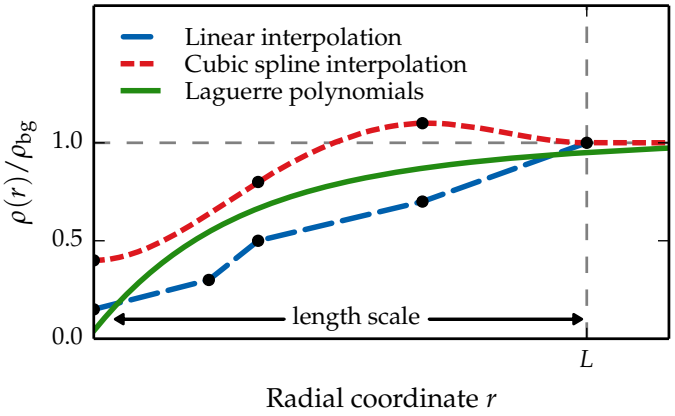

Figure 2: Illustration of the three different parametrisations for the local matter density profile around the observer. The black dots indicate the nodes of the interpolation schemes. Note that the representation by Laguerre polynomials does not have a fixed radial size, but only asymptotes to the homogeneous background density.

1. *Linear interpolation*: The first free model parameter is the radial size L of the inhomogeneity. For radii $r < L$, we use linear interpolation, specified by pairs of radial coordinates and corresponding matter densities: $[(r_0 = 0, \rho_0), (r_1, \rho_1), \ldots, (r_n, \rho_n)]$, where $r_n < L$ and all densities ρ_i are strictly positive. For radii $r \geq L$, the density profile is constant and equals the matter density ρ_{bg} of the homogeneous FLRW background. $M'(r)$ (cf. Eq. (15)), and thereby also radial derivatives of the areal radius function $R(t,r)$ (cf. Eq. (36)) are not smooth if the density profile is linearly interpolated. All functions required for this work remain continuous, however, which is sufficient for the computations.

2. *Cubic spline interpolation*: This model has the same free parameters as the linear interpolation model: a radial size L, pairs of radial coordinates, and corresponding matter densities $[r_i, \rho_i = \rho(r_i)]$. Cubic splines are used to interpolate between these nodes. We chose the boundary conditions $\rho(r \geq L) = \rho_{\mathrm{bg}}$ and $\rho'(r = 0) = \rho'(L) = 0$ to enforce a smooth void profile at the origin and guarantee a smooth embedding into the homogeneous FLRW background. This is essentially equivalent to the spline model used by Zibin et al. (2008) and Moss et al. (2011).

3. *Laguerre polynomials*: Again, the first free model parameter is a radial length scale L. We introduce the scaled radial coordinate $x = r/L$ and define the matter density profile as

$$\rho(t_0, r) = \rho_{\mathrm{bg}} \left[1 + \exp(-x) \sum_i a_i \mathrm{L}_i(x) \right] , \tag{49}$$

where L_i denote the Laguerre polynomials, which are an orthogonal basis with respect to the inner product $\langle \mathrm{L}_i, \mathrm{L}_j \rangle = \int_0^\infty \mathrm{L}_i(x)\, \mathrm{L}_j(x)\, \exp(-x)\, \mathrm{d}x$. In practice, we used Laguerre polynomials up to fifth order, because more degrees of freedom were not constrained by the data. In contrast to the previous interpolation schemes, the Laguerre models do not have a fixed size. Instead, their density profiles only asymptote (characteristic length scale L) to the homogeneous background density.

The different approaches are visualised in Fig. 2. We conducted detailed tests as explained in Sect. 2.5 with each of the three parametrisations, finding qualitatively the

same results. Because the meaning of the free model parameters of the interpolation schemes is quite instructive while on the other hand the geometrical interpretation of expansion coefficients of Laguerre polynomials is not straightforward, we focus our discussion in the subsequent sections on the linear and cubic spline interpolations.

2.4.2 *Algorithm*

In our approach, LTB models are generally determined by the dimensionless Hubble parameter $h = H_0/(100\,\mathrm{km\,s^{-1}\,Mpc^{-1}})$, the density parameter of the cosmological constant Ω_Λ, and the physical densities of baryonic and cold dark matter, $\omega_\mathrm{b} = \Omega_\mathrm{b}h^2$ and $\omega_\mathrm{c} = \Omega_\mathrm{c}h^2$, of the homogeneous FLRW background, as well as a list of model parameters $(a_1, ..., a_n)$ that parametrise the local matter density profile $\rho(t_0, r)$ at the present time t_0. If not stated otherwise, these are the base parameters that are later sampled by the MC method that was used for fitting LTB models to observational data. Given these base parameters, our algorithm for computing observables in the LTB metric can be outlined as follows:

1. *Age of the Universe*: As emphasised before, we demand a homogeneous early Universe and thus set the bang time function $t_\mathrm{B}(r)$ to zero. Therefore, the LTB patch and the homogeneous background have the same global age t_0, which we compute using the standard FLRW relation,

$$t_0 = \frac{1}{H_0}\int_0^1 \frac{\sqrt{a}}{\sqrt{\Omega_\mathrm{m} + \Omega_\mathrm{k}a + \Omega_\Lambda a^3}}\,\mathrm{d}a\,, \tag{50}$$

   where the curvature parameter is given by $\Omega_\mathrm{k} = 1 - \Omega_\mathrm{m} - \Omega_\Lambda$.

2. *Gauge freedom*: All formulae given in Sect. 1.2 are invariant under coordinate transformations of the form $\tilde{r} = g(r)$. We exploit this gauge freedom to scale the radial coordinate r such that it equals the areal radius function at the present time: $R(t_0, r) = r$.

3. *Mass profile*: Given the parameters $(a_1, ..., a_n)$, we construct the matter density profile at the present time $\rho(t_0, r)$. We reject combinations of parameters that induce negative matter densities. This is important for the cubic spline interpolation and the Laguerre polynomials. In our gauge, the effective gravitational mass $M(r)$ then directly follows from integrating Eq. (15),

$$M(r) = 4\pi G\int_0^r \rho(t_0, \tilde{r})\,\tilde{r}^2\,\mathrm{d}\tilde{r}\,. \tag{51}$$

4. *Curvature profile*: The curvature function $E(r)$ is implicitly defined by Eq. (14) and can only be computed numerically. We use the TOMS 748 root-bracketing algorithm from Alefeld et al. (1995) to determine $E(r)$ as a function of t_0, r, and $M(r)$, see Krasiński & Hellaby (2002) for details on choosing the initial bracket.

We reject mass models that require $E(r) \leq -1/2$ because this would cause singular line-elements (cf. Eq. (16)). The radial derivative $E'(r)$ is numerically computed using a standard fourth-order finite differencing scheme.

5. *Distance–redshift relation*: We use a fifth order Dormand-Prince method – which is essentially a Runge-Kutta scheme with error control and adaptive step size (Ahnert & Mulansky 2011) – to numerically integrate the ordinary differential equations describing radial null geodesics on the PNC of a central observer (cf. Eqs. (22) and (28)). The resulting relations $t(r)$ and $z(r)$ are then interpolated and numerically inverted using smooth Akima splines (Akima 1970). This allows us to arbitrarily transform between t, r, and z and, in particular, to compute angular-diameter and luminosity distances (see Sect. 1.4). We discard LTB models that exhibit shell-crossings or multivalued redshifts on the PNC (Hellaby & Lake 1985).

This algorithm allowed us to compute all observable quantities that are required for performing likelihood estimates of LTB models.

2.4.3 *Efficient statistical sampling*

We are confronted with a typical parameter estimation problem. Given observational data, we need to explore the posterior distribution in a high-dimensional parameter space to estimate the most likely values of the free model parameters $(h, \Omega_\Lambda, \omega_\mathrm{b}, \omega_\mathrm{c}, a_1, ..., a_n)$. Monte Carlo methods are the standard approach for solving this kind of problem, and most commonly, variants of the simple Metropolis-Hastings algorithm are used (Hastings 1970).

The Metropolis-Hastings algorithm has an important drawback, however: it requires a fine-tuned proposal distribution to efficiently sample the posterior. If the proposal distribution is thought of as a multivariate Gaussian, this means that each entry of the covariance matrix needs to be tuned. In our case, the matter densities at different radial coordinates can be correlated and hence the covariance matrix is non-diagonal. Consequently, we would have to hand-tune $N(N+1)/2$ unknown parameters (where N is the dimension of the parameter space). This is an extremely time-consuming task, in particular because the fine-tuned parameters strongly depend on the precise parametrisation (e.g. number and position of interpolation nodes) of the matter density profile.

After some testing, we decided to use an alternative MC sampler: the so-called stretch-move technique, which was first introduced by Goodman & Weare (2010). This technique is affine-invariant, meaning that it performs equally well under all linear transformations of the parameter space. In particular, it is insensitive to covariances between parameters and therefore requires no fine-tuning. Goodman & Weare (2010) demonstrated the excellent performance of their algorithm (as measured by the auto-correlation time) for several pathological posterior distributions.

In addition, the stretch-move sampler simultaneously explores the parameter space with a whole ensemble of MC walkers. The time evolution of this ensemble can easily be parallelised, which greatly reduces the required computing time (wall-clock time)

on multi-core machines or large computing clusters (Akeret et al. 2013). Foreman-Mackey et al. (2013) provided an excellent discussion of the stretch-move technique and described a parallelised implementation in detail. Following this, we implemented the ensemble sampler in `C++` and parallelised it with the message-passing interface (MPI) system. This enabled us to perform likelihood estimates of many different LTB models within a significantly shorter computing time.

All parameter estimations in the remainder of this chapter were performed with the stretch-move technique, typically using hundreds of walkers. The length of the burn-in period was estimated by means of the *exponential* auto-correlation time τ_{exp}. Convergence of the samples was ensured by letting the random walks proceed for multiple *integrated* auto-correlation times τ_{int} after removing all samples drawn during the initial burn-in period. This procedure was advocated by Akeret et al. (2013) and Allison & Dunkley (2014), who provided a detailed discussion of convergence diagnostics with the auto-correlation times described above.

2.5 COMPARING LTB MODELS WITHOUT COSMOLOGICAL CONSTANT WITH OBSERVATIONAL DATA

We now compare LTB models with consecutively different combinations of observational data. This stepwise analysis allows us to carefully explain why LTB models with a constant bang time function and zero cosmological constant are inconsistent with current data. The following results are representative. For each scenario discussed, we fitted numerous different LTB models, varying the radial size of voids, changing the numbers and positions of interpolation nodes, or considering different orders of the expansion in terms of the Laguerre polynomials. Our findings with the different approaches agreed qualitatively well, therefore we only discuss simple parametrisations that already show all important characteristics.

2.5.1 *Constraints: H_0 + supernovae*

To begin with, we only analysed the constraints imposed by the local Hubble rate and supernovae. We therefore considered LTB models of fixed radial size $L = 3\,\mathrm{Gpc}$ and parametrised the matter density profiles with linear and cubic spline interpolation schemes with three equidistant nodes at radii $r_1 = 0$, $r_2 = 1\,\mathrm{Gpc}$, $r_3 = 2\,\mathrm{Gpc}$. It is convenient to express the matter densities at these nodes with respect to the matter density ρ_{bg} of the FLRW background model, viz $a_i = \rho(r_i)/\rho_{\mathrm{bg}}$. The priors for the parameters a_i were only bounded from below ($a_i \geq 0$), so that the stretch-move walkers could essentially freely explore the physically relevant parameter space.

Anticipating the following results, we asymptotically embedded the LTB models in Einstein-de-Sitter (EdS) backgrounds for this particular test, meaning that we explicitly set the spatial curvature of the homogeneous background to zero ($\Omega_{\mathrm{k}} = 0$). We did this to demonstrate that good fits to the data can be achieved even with asymptotically flat backgrounds. As can easily be verified, the models considered are fully determined by the physical matter density ω_{m} of the EdS background and the profile parameters (a_1, a_2, a_3).

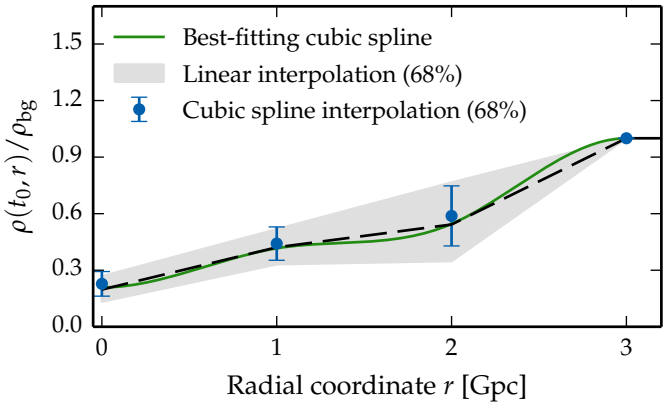

Figure 3: Statistical constraints on the shape of the local matter density profile at the present time. LTB models with fixed radial size $L = 3$ Gpc and three equidistant interpolation nodes were constrained by measurements of the local Hubble rate and supernovae. The blue error bars and the grey-shaded band indicate the 68% confidence intervals for the cubic spline and linear interpolation schemes, respectively. The black dashed line connects the means of the best-fitting nodes for the linear interpolation scheme. The green solid curve shows the best-fitting cubic spline density profile.

Figure 3 illustrates the preferred shape of the local matter density profile given the local Hubble rate and supernova data. More precisely, we show the 68% confidence intervals for the best-fitting linear and cubic spline interpolation models. Note that the constraints for the two different approaches are almost identical. As expected, the data clearly favour large and deep voids whose density profiles gradually decrease towards the origin. This shape is required to account for the apparent acceleration suggested by the supernova data. Typically, the density contrast at the origin is $\delta\rho(t_0, r = 0)/\rho_{\mathrm{bg}} \approx -0.75$. It can also be seen that the constraints on the matter density profile weaken at larger radii. This is naturally caused by the quality of the data. Small radii correspond to low redshifts. In this range, the profiles are simultaneously constrained by the measurement of the local Hubble rate ($z < 0.1$) and also by many supernovae with comparably small error bars. At higher redshifts, the amount of observed supernovae decreases, and at the same time, their errors increase (mainly because the supernovae become fainter). Therefore, the matter density profile can substantially fluctuate at larger radii without being penalised too strongly. This freedom also demonstrates that the LTB models considered can easily fit the data without a cosmological constant and zero background curvature. The best-fitting cubic spline model has an excellent log-likelihood value of $\log(\mathcal{L}) = -272.27$ and fits the data just as well as the best-fitting ΛCDM model with $\log(\mathcal{L}) = -272.56$.

Figure 4 reveals more details of the Markov Chain Monte Carlo (MCMC) simulation specifically for the cubic spline model. While the marginalised posterior distributions, the means, and the standard deviations of the density profile parameters a_i confirm the above discussion, the almost perfect linear correlations between the parameters enforce the idea of a gradually decreasing density profile towards the symmetry centre: If a_i is increased, also a_{i+1} has to grow to generate the gradient of the expansion rate required by the data. The physical matter density ω_{m} determines the expansion

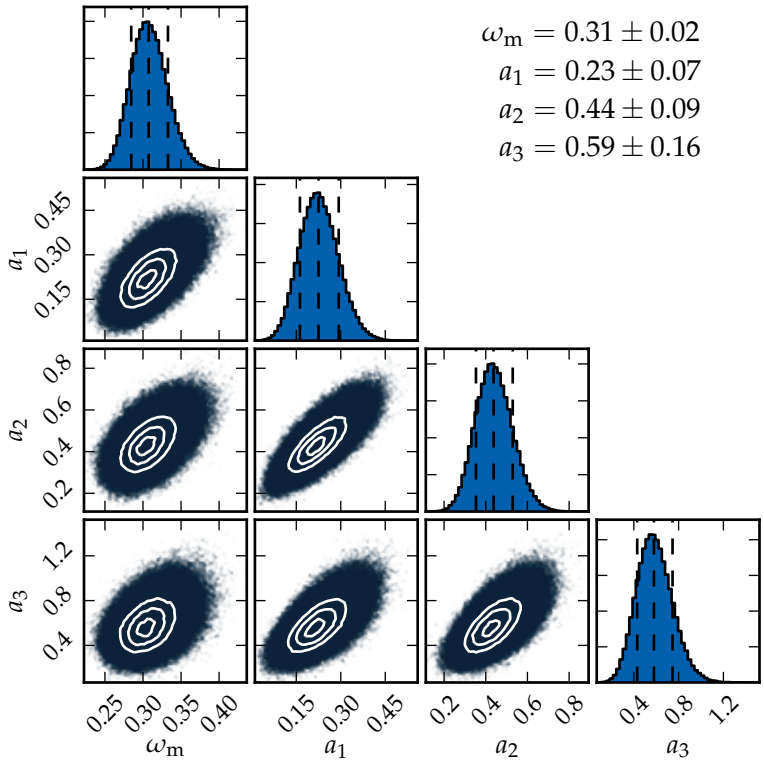

Figure 4: Statistical constraints on the shape of the local matter density profile imposed by measurements of the local Hubble rate and supernovae. ω_m denotes the physical matter density of the EdS background model. The local density profile was parametrised by a cubic spline interpolation with three equidistant nodes at radii $r_1 = 0$, $r_2 = 1\,\mathrm{Gpc}$, $r_3 = 2\,\mathrm{Gpc}$ and a fixed radial size of $L = 3\,\mathrm{Gpc}$. The matter density at these nodes was normalised with respect to the background density today, viz $a_i = \rho(t_0, r_i)/\rho_\mathrm{bg}(t_0)$.

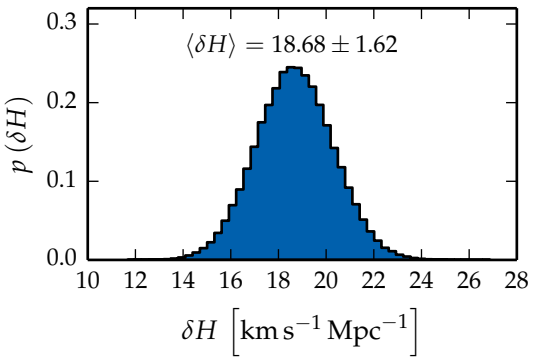

Figure 5: Marginalised posterior distribution of the increase of the local Hubble rate H_LS (Eq. (45)) at the origin (due to the under-density) with respect to the Hubble rate H_bg of the homogeneous background model, $\delta H = H_\mathrm{LS} - H_\mathrm{bg}$. LTB models with fixed radial size $L = 3\,\mathrm{Gpc}$ and a local matter density profile represented by cubic splines with three equidistant interpolation nodes were fitted to observational data of the local Hubble rate and supernovae.

rate of the background EdS model through $h = \sqrt{\omega_\mathrm{m}}$. This is why ω_m and the profile parameters a_i are correlated: If ω_m decreases, so does the expansion rate of the background model, which means that the voids need to become even deeper to maintain the required high local Hubble rate at the origin.

The average increase of the expansion rate around the central observer due to the large-scale under-density is the last aspect worth being considered in more detail. We therefore defined $\delta H = H_\mathrm{LS} - H_\mathrm{bg}$, which measures the difference between the effective local Hubble rate H_LS (cf. Eq. 45) at the void centre and the global Hubble rate H_bg of the background model. From the mean value of the physical matter density ω_m in Fig. 4, we extracted that the data favour $H_\mathrm{bg} \approx 56\,\mathrm{km\,s^{-1}\,Mpc^{-1}}$, which requires an average shift of $\delta H \approx 18\,\mathrm{km\,s^{-1}\,Mpc^{-1}}$ to fulfil the observationally measured Hubble rate of $H_0 \approx 74\,\mathrm{km\,s^{-1}\,Mpc^{-1}}$. The magnitude of this shift agrees well with previous works (Enqvist & Mattsson 2007). The marginalised posterior distribution of δH is plotted in Fig. 5. Even though the voids can become extremely deep, the local Hubble rate rarely increases by more than $\sim 24\,\mathrm{km\,s^{-1}\,Mpc^{-1}}$. This tendency is also important for Sect. 2.5.3.

2.5.2 *Constraints: Cosmic microwave background*

We proceed by analysing the implications of only the model-independent CMB constraints from Table 1. As reference, we first ran an MCMC simulation to fit curved FLRW models with vanishing cosmological constant to the data. These models can fit the CMB constraints just as well as flat FLRW models with non-vanishing cosmological constant. The data favour closed FLRW models with dimensionless Hubble parameter $h = 0.33 \pm 0.01$, matter density parameter $\Omega_\mathrm{m} = 1.26 \pm 0.04$, and consequently a curvature parameter of $\Omega_\mathrm{k} \approx -0.26$. It is important to note that although curved FLRW models can easily fit the minimal CMB constraints without a cosmological constant, the required Hubble rate is extremely low and strongly contradicts the expansion rate measured by Riess et al. (2011).

Next, we compared the same LTB models as in the previous section ($L = 3\,\mathrm{Gpc}$; three equidistant interpolation nodes) with the CMB data. This time, however, we asymptotically embedded the LTB models into curved FLRW backgrounds. Of course, these cosmological models fit the data perfectly as well. The constraints on the physical matter density $\omega_\mathrm{m} = \omega_\mathrm{b} + \omega_\mathrm{c}$ and the dimensionless Hubble parameter h of the background model are essentially identical to those found without an LTB inhomogeneity around the observer. Again, an extremely low expansion rate of $h = 0.33 \pm 0.01$ is favoured. The shape of the local matter density profile is not constrained at all. The posteriors of the densities $\rho(r_i)$ at the interpolation nodes are constant over the whole prior ranges, indicating that the MC walkers can vary the shape of the local matter density profile without notably deteriorating the fit to the CMB. Moreover, the best-fitting LTB models show almost arbitrarily shaped local density profiles. These results are the same for LTB models with different radial sizes, more or less interpolation nodes, or density profiles represented by Laguerre polynomials.

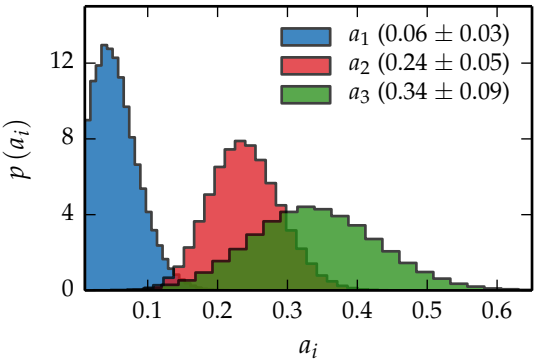

Figure 6: Constraints on the linearly interpolated matter density profile of LTB models with fixed radial size $L = 3\,\mathrm{Gpc}$ and three equidistant interpolation nodes at $r_1 = 0$, $r_2 = 1\,\mathrm{Gpc}$ and $r_3 = 2\,\mathrm{Gpc}$. The coefficients a_i denote the matter densities at these nodes normalised with respect to the background density today, viz. $a_i = \rho(t_0, r_i)/\rho_{\mathrm{bg}}(t_0)$. The LTB models were constrained by observational data of the local Hubble rate, supernovae, and the CMB.

We conclude that the CMB data alone only constrain the global properties of the background FLRW model. In particular, good fits without a cosmological constant require an extremely low Hubble parameter of $h < 0.4$. The exact functional form of the local curvature and the matter density profiles are essentially irrelevant. These results agree well with the work of Clifton et al. (2009), who found that the small angle fluctuations of the CMB spectrum only constrain spatial curvature near the surface of last scattering.

2.5.3 *Constraints: H_0 + supernovae + cosmic microwave background*

Finally, we simultaneously fitted LTB models to the local Hubble rate, supernovae, and the CMB data. Before that, however, we fitted spatially flat FLRW models with non-vanishing cosmological constant to the data. The best-fitting model has the cosmological parameters $(h, \Omega_{\mathrm{m}}, \Omega_\Lambda) = (0.719, 0.265, 0.735)$ and a log-likelihood value of $\log(\mathcal{L}) = -273.45$. This model – and in particular its log-likelihood value – serves as a reference point for the following discussion.

We now considered LTB models with fixed radial size $L = 3\,\mathrm{Gpc}$ and linearly interpolated matter density profile with three equidistant interpolation nodes at the radial coordinates $r_1 = 0$, $r_2 = 1\,\mathrm{Gpc}$ and $r_3 = 2\,\mathrm{Gpc}$. For these models, the data favour an FLRW background with dimensionless Hubble parameter $h = 0.39 \pm 0.01$ and matter density parameter $\Omega_{\mathrm{m}} = 1.09 \pm 0.03$, demonstrating that curved FLRW backgrounds can indeed improve the fit to the CMB. The statistical constraints on the local matter density profile at the present time t_0 are shown in Fig. 6. While the overall shape of the favoured profiles agrees well with our previous results from Sect. 2.5.1, the voids become noticeably deeper when including the constraints from the CMB. This change becomes most apparent for the matter density at the origin, $a_1 = \rho(t_0, r = 0)/\rho_{\mathrm{bg}}(t_0)$, indicating that the best agreement with the data can be achieved with an almost vacuum solution around the observer at the coordinate centre.

This tendency demonstrates the problem of LTB models with a constant bang time function and zero cosmological constant: A reasonable fit to the CMB – most importantly the angular-diameter distance to the LSS – requires an unrealistically low background Hubble parameter of $H_0 \approx 39\,\mathrm{km\,s^{-1}\,Mpc^{-1}}$. On the other hand, the LTB

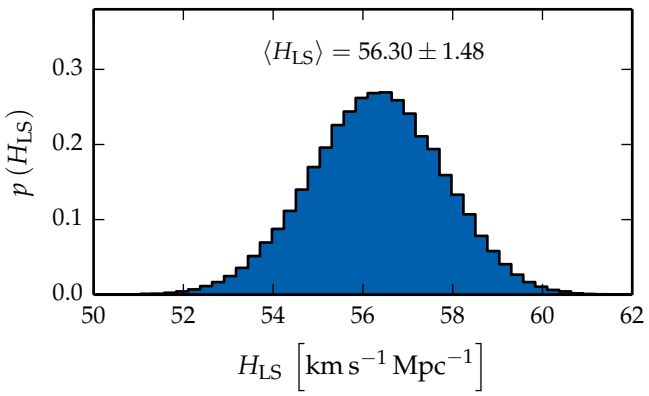

Figure 7: Marginalised posterior distribution of the effective local Hubble rate H_{LS} (Eq. (45)) of LTB models with radial size $L = 3\,\mathrm{Gpc}$ and linearly interpolated (using three equidistant nodes) matter density profile. The models were fitted to observational data of the local Hubble rate, supernovae, and the CMB.

models also need to comply with the observationally measured, high local Hubble rate of $H_0 \approx 73.8\,\mathrm{km\,s^{-1}\,Mpc^{-1}}$. The MC walkers therefore minimise the matter density at the origin to maximise the local expansion rate. However, Fig. 7 shows that even though the voids can become extremely deep, the effective local Hubble rate never exceeds $\sim 62\,\mathrm{km\,s^{-1}\,Mpc^{-1}}$. The best-fitting model, for instance, has the profile parameters $(a_1, a_2, a_3) = (0.04, 0.22, 0.32)$, which means that the matter density almost vanishes at the origin. The local Hubble rate still is much too low, $H_{\mathrm{LS}} = 56.83\,\mathrm{km\,s^{-1}\,Mpc^{-1}}$, however, and the log-likelihood value of $\log(\mathcal{L}) = -318.55$ indicates that the model clearly cannot compete with simple, spatially flat FLRW models with cosmological constant.

As discussed in Sect. 2.3.1, we computed the effective local Hubble rate H_{LS} by means of a least-squares fit to the Taylor-expanded luminosity distance for small redshifts, $z < 0.1$. Legitimately, one might therefore ask whether a radially fine-tuned matter density profile in the nearby range $(0 < z(r) < 0.1)$ might be capable of solving the above tension. We refute this idea by adding one additional interpolation node at $r = 500\,\mathrm{Mpc}$ and re-running the fitting procedure. The best-fitting model improves only marginally, with a slightly higher effective local Hubble rate of $H_{\mathrm{LS}} = 57.26\,\mathrm{km\,s^{-1}\,Mpc^{-1}}$ and a still inacceptable log-likelihood value of $\log(\mathcal{L}) = -317.30$. Consequently, we note that even radial fine-tuning of the matter density profile cannot mitigate the tension between the required high local Hubble rate and a good fit to the CMB.

Lastly, we discuss the impact of the radial void size on the fit to the data. We considered LTB models whose density profiles are represented by cubic spline interpolations with three equidistant nodes at the radial coordinates $r_i = (i-1) \times L/3$. Table 2 summarises the best-fitting models for ascending radial sizes, $L = 3\,\mathrm{Gpc}$, $L = 4.5\,\mathrm{Gpc}$, and $L = 7.5\,\mathrm{Gpc}$. Obviously, the fit to the data significantly improves as the voids become larger. The favoured scenarios are extremely deep Gpc-scale under-densities, which are asymptotically embedded into increasingly dense FLRW backgrounds.

This antipodal behaviour is caused by the constraints from the CMB; the background FLRW models need to increase the convergence to decrease the angular-diameter distance to the LSS. Again, even though the best-fitting models are essentially empty at the origin, the effective local Hubble rate is clearly too low compared with the

Table 2: Evolution of the best-fitting LTB models for varying radial size L in Gpc. h and Ω_{m} denote the dimensionless Hubble parameter and the matter density parameter of the background FLRW model, respectively. The matter density profiles were parametrised by cubic spline interpolation schemes with three equidistant nodes at the radial coordinates $r_i = (i-1) \times L/3$. The coefficients a_i denote the matter densities at these nodes normalised with respect to the background density today, viz. $a_i = \rho(t_0, r_i)/\rho_{\mathrm{bg}}(t_0)$. H_{LS} is the effective Hubble rate measured at the origin. The last column shows the log likelihood values. The LTB models were fitted to observational data of the local Hubble rate, supernovae, and the CMB.

L	h	Ω_{m}	a_1	a_2	a_3	H_{LS}	$\log(\mathcal{L})$
3	0.39	1.10	0.07	0.27	0.45	56.01	-320.14
4.5	0.39	1.18	0.01	0.12	0.17	60.13	-299.95
7.5	0.39	1.37	0.01	0.12	0.44	62.52	-293.26

observed value. We thus note that even gigantic voids of radial size 7.5 Gpc with radially fine-tuned matter density profile are inconsistent with current data. Clearly, these models cannot compete with the standard cosmological model, which has a log-likelihood value of $\log(\mathcal{L}) = -273.45$.

We could continue this procedure and construct ever larger voids with more free interpolation nodes. Indeed, while testing our code, we observed that LTB voids with radial sizes $\gtrsim 12$ Gpc slowly converge to the same log-likelihood value as the standard cosmological model. It does not make much sense, however, to seriously consider even larger voids than those presented in Table 2 as faithful representations of the observable Universe for mainly two reasons. Firstly, these models become yet more implausible with growing size. We recall that we envisaged voids that emerged from fluctuations of the primordial matter distribution. For these voids to reach a size of several Gpc today, the primordial under-densities must have been extreme. These scenarios are therefore highly unlikely within the standard inflationary paradigm (see also Marra et al. 2013a). Secondly, as was shown for example by García-Bellido & Haugbølle (2008), Zibin & Moss (2011) or Bull et al. (2012), large voids generate a pronounced kSZ effect that is strongly inconsistent with current observational data.

The results of this section agree qualitatively well with previous works, which consistently found that LTB models that fit the CMB data exhibit unrealistically low local Hubble rates (e.g. Biswas et al. 2010; Moss et al. 2011; Bull et al. 2012). We now seek a theoretical explanation for this empirical result.

2.6 THEORETICAL ARGUMENTS FOR CONSIDERING ΛLTB MODELS

2.6.1 *Why vacuum solutions maximise the local Hubble rate*

In the previous section, we found that huge Gpc-scale voids with almost constant vacuum solution around the origin are favoured when the local Hubble rate and the CMB data are to be fitted simultaneously. Intuitively, it is comprehensible that such vacuum solutions indeed maximise the local Hubble rate. However, we can also

understand this result using Raychaudhuri's equation (Raychaudhuri 1955), which in LTB models is

$$\dot{H}_\mathrm{L} + 2\dot{H}_\mathrm{T} = -\frac{1}{3}\theta^2 - \sigma^2 - 4\pi G\,\rho \ , \tag{52}$$

with expansion $\theta^2 = (H_\mathrm{L} + 2H_\mathrm{T})^2$, shear $\sigma^2 = \frac{2}{3}(H_\mathrm{L} - H_\mathrm{T})^2$, and a dot indicating the derivative with respect to an appropriately chosen affine parameter. Generally, the shear in LTB models vanishes as $r \to 0$, implying that the longitudinal and transversal Hubble rates become identical close to the origin (Plebański & Krasiński 2006). For Gpc-scale voids with almost constant density profile, however, the approximation $H_\mathrm{L} \approx H_\mathrm{T}$ is accurate even for larger radii, in particular in the redshift interval ($z < 0.1$) in which we determine the effective local Hubble rate (cf. Sect. 2.3.1). In the region around a central observer, LTB solutions are then practically indistinguishable from simple FLRW models, and Eq. (52) simplifies to

$$3\dot{H} = -3H^2 - 4\pi G\,\rho \ . \tag{53}$$

Equation (53) describes the time evolution of the Hubble rate as a function of the matter density. Starting from an initial Hubble rate H_i at an early time t_i (e.g. a time t_i at which the Universe was still homogeneous), we can readily integrate Eq. (53) to compute the expansion rate at a later time t_f

$$H(t_\mathrm{f}) = \frac{1}{\frac{1}{H_\mathrm{i}} + \int_{t_\mathrm{i}}^{t_\mathrm{f}} \left(1 + \frac{1}{2}\Omega_\mathrm{m}(t')\right)\,\mathrm{d}t'} \ , \tag{54}$$

where we introduced the common matter density parameter $\Omega_\mathrm{m} = \frac{8\pi G\rho}{3H^2}$. Clearly, the final Hubble rate is maximised by minimising the denominator of Eq. (54), which is achieved by setting Ω_m to zero. The local expansion rate of Gpc-scale voids with slowly varying density profile is thus indeed maximised by vacuum solutions.

2.6.2 *Why not even vacuum LTB solutions exhibit a sufficiently high local Hubble rate*

Given the result of the previous section, we can now introduce a vast simplification that helps us explain why not even empty LTB models (that simultaneously fulfil the model-independent constraints from the CMB) exhibit an effective local Hubble rate that comes close to the observationally measured value of $H_0 \approx 73.8\,\mathrm{km\,s^{-1}\,Mpc^{-1}}$. We recall that we work in the synchronous time gauge and with a constant bang time function, meaning that the Universe has the same global age t_0 everywhere. We can now envisage a simplified top-hat scenario in which the Universe is globally described by a curved FLRW model, but the observer is located at the centre of an empty sphere ($\Omega_\mathrm{m} = 0$, i. e. a Milne model) that was carved out of the homogeneous background. For the purpose of this simplified scenario, technical details concerning the embedding or smooth junction conditions are not relevant. The Hubble function in both regions is given by

$$H^2(a) = H_0^2\left(\Omega_\mathrm{m} a^{-3} + \Omega_\mathrm{k} a^{-2}\right) \ , \tag{55}$$

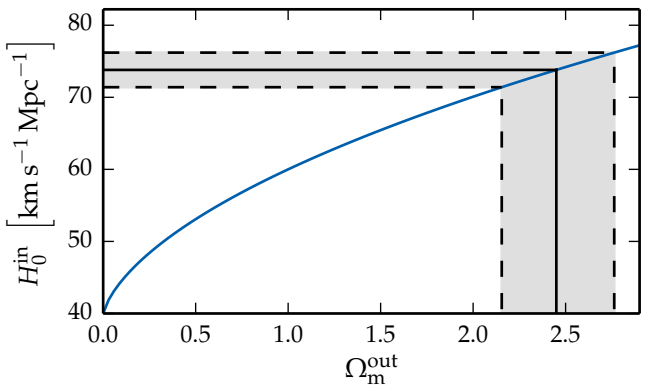

Figure 8: Hubble rate H_0^{in} inside an empty sphere around the observer as a function of the matter density parameter $\Omega_{\mathrm{m}}^{\mathrm{out}}$ of the background FLRW model. The black solid line and the grey-shaded area indicate the local Hubble rate and the corresponding 68% confidence interval as measured by Riess et al. (2011).

where a denotes the usual scale factor (with $a(t_0) = 1$) and the curvature parameter is determined by $\Omega_{\mathrm{k}} = 1 - \Omega_{\mathrm{m}}$. Integrating Eq. (55) in time yields the standard FLRW relation for the age of the Universe

$$t_0 = \frac{1}{H_0} \int_0^1 \frac{1}{\sqrt{\Omega_{\mathrm{m}} a^{-1} + \Omega_{\mathrm{k}}}} \, \mathrm{d}a \, . \tag{56}$$

As this age is assumed to be globally the same, we can directly relate the Hubble rate H_0^{in} inside the empty sphere surrounding the observer to the Hubble rate H_0^{out} of the curved background,

$$H_0^{\mathrm{in}} = \frac{H_0^{\mathrm{out}}}{f\left(\Omega_{\mathrm{m}}^{\mathrm{out}}\right)} \, , \quad f\left(\Omega_{\mathrm{m}}^{\mathrm{out}}\right) = \int_0^1 \frac{1}{\sqrt{\Omega_{\mathrm{m}}^{\mathrm{out}} a^{-1} + \left(1 - \Omega_{\mathrm{m}}^{\mathrm{out}}\right)}} \, \mathrm{d}a \, . \tag{57}$$

Figure 8 shows the resulting relation between the Hubble rate H_0^{in} and the matter density parameter $\Omega_{\mathrm{m}}^{\mathrm{out}}$ for a fixed background Hubble rate $H_0^{\mathrm{out}} = 40\,\mathrm{km\,s^{-1}\,Mpc^{-1}}$, which is the value that was favoured by the CMB data in Sect. 2.5.3. For instance, if we embed the empty sphere into an Einstein-de Sitter (EdS) background, we find $f\left(\Omega_{\mathrm{m}}^{\mathrm{out}} = 1\right) = 2/3$, such that the Hubble rate at the observer position becomes $H_0^{\mathrm{in}} = 60\,\mathrm{km\,s^{-1}\,Mpc^{-1}}$. This agrees well with several previous works, which empirically found that large and deep voids that are embedded into EdS backgrounds cannot increase the local Hubble rate by more than $\sim 20\,\mathrm{km\,s^{-1}\,Mpc^{-1}}$ (Marra & Notari 2011). Our simple approximation also agrees surprisingly well with the results from Table 2. Most importantly, however, Fig. 8 shows that unrealistically high values for the matter density parameter $\Omega_{\mathrm{m}}^{\mathrm{out}}$ are required to reach the observationally measured local Hubble rate. These theoretical solutions are excluded by current observational data (e.g. constraints from the CMB).

We can thus safely conclude that not even giant LTB voids with radial sizes of several Gpc and vanishing matter density at the origin can simultaneously fit the observed local Hubble rate and the CMB.

2.6.3 *Inhomogeneous Big Bang or cosmological constant?*

The decisive property that we exploited in the previous section to link the local Hubble rate around the observer to the Hubble rate of the background model was the

assumption of a constant global age throughout the whole Universe. The problem of a too low local Hubble rate can easily be solved by dropping this assumption. To see this very clearly, we used some trivial substitutions to rewrite Eq. (14) in the standard form

$$t - t_{\mathrm{B}}(r) = \frac{1}{H_0(r)} \int_0^1 \frac{\sqrt{a}}{\sqrt{\Omega_{\mathrm{m}}(r) + \Omega_{\mathrm{k}}(r)a + \Omega_\Lambda a^3}} \, \mathrm{d}a \,, \tag{58}$$

where the density parameters $\Omega_x(r)$ can have an explicit radial dependence in LTB models. Obviously, the local Hubble rate can be increased by decreasing the age of the local Universe. Varying bang time functions that increase towards the origin ($r = 0$) are thus yet another mechanism to mimic the apparent acceleration of the Universe. In fact, Krasiński (2014) showed that the bang time function can be calibrated such that LTB models exactly reproduce the distance–redshift relation of the standard cosmological model (with dark energy).

These models have previously been discussed in the literature (Clifton et al. 2009; Bull et al. 2012). They were shown to solve the tension between the local Hubble rate and the CMB data. However, Bull et al. (2012) demonstrated that models with the required fluctuations in the bang time function produce a pronounced kSZ effect in galaxy clusters, which is strongly inconsistent with current data.

In addition, we have fundamental objections against LTB models with both flexible density profile and fine-tuned bang time function. As we explained in Sect. 2.5, the tension between the considered LTB models and current observational data arises as soon as constraints from the CMB are taken into account. In Sect. 2.2, we briefly discussed that variations in the bang time function can be identified with decaying modes in linear perturbation theory, which in turn would imply (strong) inhomogeneities at early times. However, such features strongly contradict the standard CMB analysis, which is inherently based on the assumption of a spatially isotropic and homogeneous early Universe. We do not believe that it makes sense to introduce a new feature – the varying bang time function – only to reconcile our theoretical model with the CMB, while at the same time this new feature violates the basic assumptions the CMB analysis is based upon. Furthermore, from a statistical point of view, LTB models with varying bang time function become yet more complex, with additional degrees of freedom. Given current observational data, Ockham's razor would clearly favour the standard cosmological model.

These complications can be partially avoided by extending the considered LTB models in a more natural way. Lovelock (1971; 1972) proved two remarkable, but often overlooked theorems concerning the uniqueness of Einstein's field equations. Among other things, he showed that under very general simplicity conditions and in four dimensions, any metric theory of gravity locally conserving energy-momentum must have two coupling constants, and its metric must satisfy Einstein's field equations,

$$G_{\mu\nu} = \kappa T_{\mu\nu} + \Lambda g_{\mu\nu} \,, \tag{59}$$

where $G_{\mu\nu}$, $T_{\mu\nu}$ and $g_{\mu\nu}$ are, respectively, the Einstein tensor, the energy-momentum tensor, and the metric tensor. κ and Λ are the two coupling constants, which we identify with Newton's gravitational constant and with the cosmological constant.

According to Lovelock's theorems, the cosmological constant Λ thus appears naturally not only in Einstein's field equations, but also in the field equations of any other metric theory of gravity. It could (and perhaps should) therefore be interpreted as a second coupling constant of the metric to matter, on a par with Newton's gravitational constant. Numerous alternative cosmological models – such as LTB voids – have been constructed to avoid the cosmological constant or dark energy. Nonetheless, from the point of view of Lovelock's theorem, such models must be considered incomplete unless they justify why the cosmological constant should vanish.

Following this line of reasoning, we believe that considering LTB models with non-zero cosmological constant is the most natural extension of our approach. This is an interesting step because it slightly shifts the research focus away from the dark energy problem to more general tests of the Copernican principle. For example, using flexible parametrisations of the local matter density profile, ΛLTB models allow us to derive statistical constraints on possible deviations from spatial homogeneity. In addition, effects of varying spatial curvature along the PNC can be explored. Finally, we can investigate whether fluctuations of the local matter density profile can noticeably influence the statistical inference of the best-fitting parameters of the standard cosmological model (see e.g. Marra et al. 2013b; Valkenburg et al. 2014). We briefly discuss these applications of ΛLTB models in the next section.

2.7 PROBING SPATIAL HOMOGENEITY WITH ΛLTB MODELS

In this section, we constrain the cosmological models considered by all data sets mentioned in Sect. 2.3, that is, we compute the likelihood given the local Hubble rate, supernovae, model-independent CMB constraints and kSZ data. Again, as a point of reference, we first detail the goodness-of-fit of the standard cosmological model, which is usually assumed to be a spatially flat FLRW model with non-zero cosmological constant. The best-fitting model with cosmological parameters $h = 0.72$, $\Omega_\mathrm{m} = 0.263$, and $\Omega_\Lambda = 0.737$ exhibits a log-likelihood value of $\log(\mathcal{L}) = -275.1$, with the individual contributions $\log[\mathcal{L}_{H_0}(1)] \approx -0.3$, $\log[\mathcal{L}_\mathrm{SNe}(580)] \approx -272.9$, $\log[\mathcal{L}_\mathrm{CMB}(3)] \approx -0.3$ and $\log[\mathcal{L}_\mathrm{kSZ}(9)] \approx -1.6$, where we explicitly indicated the number of fitted data points in parenthesis. It is remarkable how well the standard cosmological model agrees with these data. The goodness-of-fit, which can be quantified in terms of the chi-squared per degree of freedom, is truly impressive and hard to improve.

On the other hand, it is well-known that – even within the framework of the standard cosmological model – there seems to be a slight tension concerning the Hubble rate: While measurements with Cepheid-calibrated supernovae yield a local Hubble rate of $H_0 = (73.8 \pm 2.4)\ \mathrm{km\,s^{-1}\,Mpc^{-1}}$, the Planck CMB data (full analysis including secondary anisotropies) favour a value of $H_0 = (67.3 \pm 1.2)\ \mathrm{km\,s^{-1}\,Mpc^{-1}}$ (Riess et al. 2011; Planck Collaboration et al. 2013). This discrepancy is still debated, but it could be taken as a further motivation to explore more complicated, radially inhomogeneous ΛLTB models with spatially varying Hubble rates (Marra et al. 2013a). Moreover, we can address questions concerning the assumption of spatial homogeneity, such as:

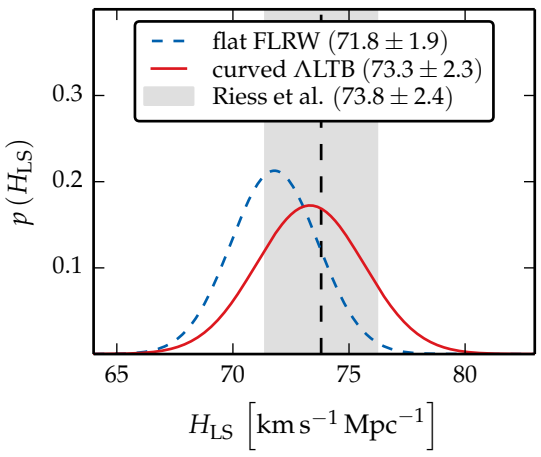

Figure 9: Marginalised posterior distributions of the effective locale Hubble rate as measured by a central observer. The blue dashed curve indicates the constraints assuming a flat FLRW model. The red curve shows the constraints assuming a ΛLTB model, with radial inhomogeneities in the range $r < 3\,\mathrm{Gpc}$, asymptotically embedded into a curved FLRW background. The grey-shaded band indicates the local Hubble rate ($\pm 1\sigma$) measured by Riess et al. (2011). The models were constrained by data from the local Hubble rate, supernovae, the CMB, and kSZ clusters.

- Can inhomogeneous cosmological models fit the data even more accurately?
- What limits do current data impose on fluctuations of the local matter density profile? How strongly can we deviate in our assumptions from spatial homogeneity?
- How do the constraints on dark energy or spatial curvature change if we drop the assumption of spatial homogeneity and marginalise over all possible radial inhomogeneities?

As discussed in Sect. 2.5.2, the CMB data do not constrain the detailed shape of the local matter density profile, but primarily the global properties of the background model and the spatial curvature close to the LSS. The kSZ data constrain the allowed depth of radial inhomogeneities, but since we assumed large errors for the individual measurements, current constraints are rather weak, at least when considering only moderate deviations from homogeneity. We would therefore expect that fine-tuned local matter density profiles can mainly improve the fit to the local Hubble rate and supernovae. As the constraining power of supernovae decreases with increasing redshift (cf. Sect. 2.5.1), it only makes sense to consider fluctuations well inside the redshift range $z < 1.5$.

For these reasons, and also for a comparison with the previous sections, we now exemplarily consider ΛLTB models whose density profile is represented by cubic splines with three flexible nodes and a fixed radial size of $L = 3\,\mathrm{Gpc}$. While testing, we also tried to treat the radial size L as a free parameter and vary it with the MC sampler, but the observational constraints are too weak so that the MC chains did not converge. We asymptotically embedded these ΛLTB models into curved FLRW backgrounds.

In summary, the considered ΛLTB models are described by the cosmological parameters h, Ω_m, Ω_Λ, $\Omega_\mathrm{k} = 1 - \Omega_\mathrm{m} - \Omega_\Lambda$ of the background, and the three spline nodes (a_1, a_2, a_3) parametrising possible fluctuations of the matter density profile. In contrast to the flat FLRW model, we hence introduced one new degree of freedom for the cosmological background (Ω_Λ free instead of setting $\Omega_\Lambda = 1 - \Omega_\mathrm{m}$) and three additional parameters for radial inhomogeneities. This way, our framework for testing

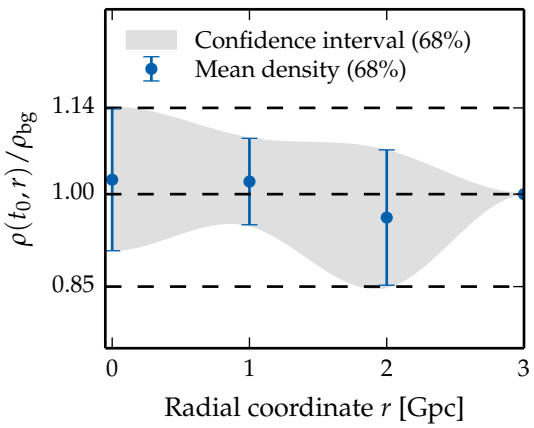

Figure 10: Statistical constraints on deviations from spatial homogeneity on radial scales $r < 3\,\mathrm{Gpc}$. The fluctuations in the matter density profile were modelled in terms of cubic splines with three equidistant nodes at $r_1 = 0$, $r_2 = 1\,\mathrm{Gpc}$ and $r_3 = 2\,\mathrm{Gpc}$. Constraints approaching $r = 3\,\mathrm{Gpc}$ should be considered artificial, since the models are forced to converge to the background density at this radius. The models were constrained by data from the local Hubble rate, supernovae, the CMB, and kSZ clusters.

the cosmological principle is most general and able to parametrise a broad class of space-time geometries.

We now sequentially discuss these questions. The best-fitting ΛLTB model has a log-likelihood value of $\log(\mathcal{L}) = -274.7$, which is only marginally better than that of the FLRW model. The fits to all observables slightly improve. There is no distinguished data set that is described significantly better. As an example, we show a comparison of the marginalised posterior distribution of the effective local Hubble rates in Fig. 9. As expected, the more flexible ΛLTB models fit the observed value better than the flat FLRW models. More surprisingly, the best-fitting model is almost perfectly homogeneous, with spline nodes $a_1 = 0.99$, $a_2 = 1.01$ and $a_3 = 0.99$. The cosmological parameters are also very similar to those of the standard model, with $h = 0.73$, $\Omega_\mathrm{m} = 0.25$, $\Omega_\Lambda = 0.74$, and $\Omega_\mathrm{k} = 0.01$.

In summary, we can conclude that, of course, the more flexible models fit the data even better. The improvement is almost negligible ($\Delta \log(\mathcal{L}) \sim 0.4$) , however, and comes at the high price of introducing four additional free parameters. Ockham's razor penalises more complicated models and can be approximated for instance by the Akaike information criterion or the Bayesian information criterion (Akaike 1974; Schwarz 1978). In our case, these criteria suggest that not even one additional free parameter would be justified. More meaningfully, we can thus conclude that the data used in this work statistically favour the standard cosmological model.

The second question concerns statistical constraints on deviations from spatial homogeneity. The mean values of the spline parameters are given by $a_1 = 1.02 \pm 0.12$, $a_2 = 1.02 \pm 0.07$ and $a_3 = 0.96 \pm 0.11$. The corresponding variations of the density profiles are depicted in Fig. 10. The density profiles were forced to converge to the background value at $r = 3\,\mathrm{Gpc}$ by construction, so the apparent constraints at $r > 2\,\mathrm{Gpc}$ are artificial. Clearly, the results agree well with the assumption of spatial homogeneity. However, the scatter of $\sim 15\,\%$ indicates that we need more accurate data to safely confirm the cosmological principle. This demonstrates the importance of fully solving linear perturbation theory in LTB backgrounds (such that it can be applied to predict cosmological observables), since this would allow us to include more cosmological observables.

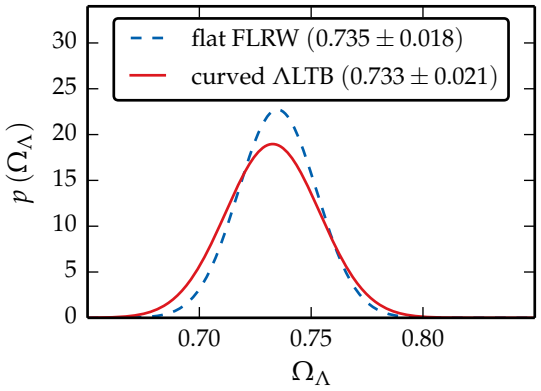

Figure 11: Marginalised posterior distributions of the energy contribution due to the cosmological constant. The blue dashed curve indicates the constraints assuming a flat FLRW model. The red curve shows the constraints assuming a ΛLTB model, with radial inhomogeneities in the range $r < 3\,\mathrm{Gpc}$, asymptotically embedded into a curved FLRW background. The models were constrained by data from the local Hubble rate, supernovae, the CMB, and kSZ clusters.

For instance, it would be natural to expect that Gpc-scale variations of the matter density profile leave a characteristic imprint on the large-scale structure of the local Universe. Such imprints could create non-vanishing amplitudes of the galaxy-galaxy correlation function on Gpc-scales, which would be at odds with data from current spectroscopic surveys (Labini 2011; Scrimgeour et al. 2012). Furthermore, Gpc-variations of the local matter distribution should be well measurable with tomographic weak-lensing methods (Schäfer & Heisenberg 2012). There are other promising observables related to cosmic structures that might help constrain deviations from spatial homogeneity, but we need to advance the numerical algorithms for solving the linear perturbation equations on LTB backgrounds before we are able to reliably calculate these phenomena.

To answer the last question, in Figs. 11 and 12 we show the statistical constraints on the cosmological constant and spatial curvature. It is important to stress that these posterior distributions were marginalised over all possible fluctuations of the matter density profile. In other words, these posteriors show constraints that are independent of the assumption of spatial homogeneity, at least within the limits of our framework. The constraints on the cosmological constant are essentially invariant, with a negligibly larger scatter. This result differs from the findings of Valkenburg et al. (2014), who calculated a shift of $\Delta\Omega_\Lambda \sim 0.05$ when marginalising over inhomogeneities. However, these authors constrained their models by different data, chose another approach for modelling spatial variations of the density profile and additionally included a so-called Copernican prior. Amongst other details, these are important issues that could well explain the difference with respect to our results. Finally, it is remarkable how tightly the spatial curvature of the background model is constrained, even though we considerably relaxed our prior assumptions. The constraints are consistent with a flat background Universe, which agrees very well with the Planck results (Planck Collaboration et al. 2013).

2.8 CONCLUSIONS

What do cosmological observations tell us about the shape of the local matter density profile? Can current data confirm the cosmological principle? These were two central questions that we discussed in this chapter.

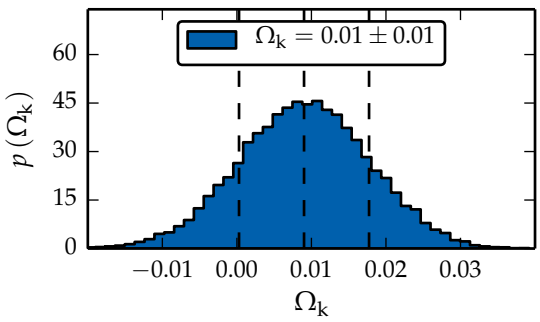

Figure 12: Posterior distribution of the spatial curvature of the background model, marginalised over fluctuations in the matter density profile at radii $r < 3\,\mathrm{Gpc}$. The black dashed lines indicate the mean value and the corresponding $\pm 1\sigma$ boundaries. The models were constrained by data from the local Hubble rate, supernovae, the CMB, and kSZ clusters.

First, we reconsidered LTB models without cosmological constant to investigate whether highly flexible, radially fine-tuned mass profiles allow us to simultaneously fit the high local Hubble rate and the CMB data from the Planck satellite (Riess et al. 2011; Planck Collaboration et al. 2013). To this end, we consecutively compared numerous LTB models with different combinations of observational data. The main results of this first part can be summarised as follows:

1. H_0 + *supernovae*: As was already well-known, LTB models without cosmological constant can easily fit the observed local Hubble rate and supernovae just as well as the standard cosmological model. These models mimic the apparent acceleration of the Universe by means of large Gpc-scale voids whose matter density profile gradually decreases towards the observer. Having said that, we would like to stress an important issue concerning the interpretation of supernova observations. Interpreted in the framework of a *spatially homogeneous* FLRW model, supernovae favour a non-zero cosmological constant. Similarly, supernovae favour Gpc-scale LTB voids if and only if we set the cosmological constant to zero and require a synchronous Big Bang. In fact, Célérier et al. (2010) demonstrated that local over-densities (i. e. giant local humps) are favoured if the bang time function is allowed to vary. We mention these ambiguities only to emphasise that the interpretation of supernovae is strongly biased by prior assumptions about the underlying cosmological model.

2. *Cosmic microwave background*: The CMB data alone do not constrain the shape of the local matter density profile. Indeed, the density profiles can substantially be varied without notably deteriorating the fit to the data. However, current CMB data impose tight constraints on the geometry and expansion rate of the asymptotic background models. Without a cosmological constant, good fits to the data require asymptotically curved FLRW backgrounds with an unrealistically low Hubble rate of $H_0 \approx 33\,\mathrm{km\,s^{-1}\,Mpc^{-1}}$.

3. H_0 + *supernovae* + *CMB*: The separate CMB analysis clearly highlighted the problem of the considered class of LTB models: A good fit to the CMB requires an extremely low background Hubble rate, which is in strong tension with the observed local Hubble rate of $H_0 = (73.8 \pm 2.4)\,\mathrm{km\,s^{-1}\,Mpc^{-1}}$ (Riess et al. 2011). In the last part of our analysis, we thus focused on the question whether or not radially tuned matter density profiles can be found that simultaneously comply

with all observational constraints. However, even though we considered a wide variety of huge, extremely deep and heavily fine-tuned void profiles, the effective local Hubble rate remained too low, $H_0 \lesssim 62\,\mathrm{km\,s^{-1}\,Mpc^{-1}}$. To make matters worse, we note that we merely used minimal, model-independent constraints from the CMB data to arrive at these conclusions (see Sect. 2.3.3, for details). We did not even use the complete information contained in the full CMB spectra, which appear to be even more problematic for void models (Moss et al. 2011).

After this detailed analysis, we presented simple theoretical arguments that explain why not even heavy fine-tuning of the radial matter density profile can solve the tension between the local Hubble rate and the CMB. Various solutions, such as varying bang time functions, dynamical effects of radiation, or modifications of the primordial curvature power-spectrum, were proposed to reconcile giant void scenarios with current data (Clarkson & Regis 2011; Nadathur & Sarkar 2011; Bull et al. 2012). However, all these modifications require deviations from the standard inflationary paradigm or introduce more complexity, resulting in fine-tuned, alternative cosmological models. Ockham's razor would clearly favour the standard cosmological model. In addition, according to Lovelock's theorems, the cosmological constant appears naturally in the field equations of general relativity and of any other metric theory of gravity (Lovelock 1971, 1972). We thus argued that considering LTB models with non-zero cosmological constant seems to be the most natural step.

In the final part, we therefore analysed LTB models with non-zero cosmological constant, which can be considered as the simplest, spatially isotropic, but radially inhomogeneous extension of the standard cosmological model. ΛLTB models are a valuable framework to systematically study deviations from spatial homogeneity, verify or falsify the cosmological principle, or simply explore effects of varying curvature along the PNC. We showed that the data used in this chapter provide no evidence for radial inhomogeneities on Gpc-scales. Instead, spatially flat FLRW models with homogeneous matter distribution are favoured. These results statistically support the Copernican principle. However, we also showed that fluctuations of $\sim 15\%$ with respect to a homogeneous matter density profile are still compatible with current data.

As emphasised in the previous sections (cf. Sects. 2.3 and 2.7), our analysis was limited by the fact that substantial additional efforts are required before linear perturbations on LTB backgrounds can reliably be computed in realistic cosmological settings. We therefore had to neglect all cosmological observables that depend on the details of linear structure formation. For instance, we had to neglect important cosmological probes such as baryonic acoustic oscillations and weak-lensing spectra, which are widely (and successfully) used to constrain homogeneous and isotropic cosmologies. We will focus our research on advancing linear perturbation theory in LTB models to tighten observational constraints on the shape of the local matter density profile in future works.

3

WEAK GRAVITIONAL LENSING IN LTB SPACE-TIMES

ABSTRACT

This chapter outlines a simple approach that could serve as a starting point for future weak-lensing studies in perturbed LTB space-times. At first, we recall the equation of geodesic deviation and derive the Sachs equation for the evolution of the Jacobi map along a fiducial null geodesic. We explain the link between the Jacobi map and the weak lensing magnification matrix. Next, as a preparatory step, we sketch the standard solution of the Sachs equation in linearly perturbed FLRW models. During the derivation, we highlight the most important simplifications that are commonly made before arriving at a closed-form expression for the Jacobi map. After that, we explain how the evolution of the Jacobi map can be calculated in linearly perturbed LTB models, particularly emphasising the main complications that arise due to the LTB metric being radially inhomogeneous. To give an explicit example, we calculate the Sachs equation for the Jacobi map in a linearly perturbed LTB metric. Finally, we conclude with a short outlook for future studies.

3.1 INTRODUCTION

The results of the previous chapter clearly demonstrated the need to include more observational data in our analysis of ΛLTB models to ultimately confirm the validity of the Copernican principle. As repeatedly emphasised, we were mainly limited by the fact that linear perturbation theory in LTB models is quite demanding, and we still lack the proper tools for numerically solving the linear perturbation equations.

To make progress in this direction, we considered the remarkable work by Clarkson et al. (2009), in which the authors developed a fully gauge-invariant linear perturbation theory in LTB models. Within their framework, the evolution of linear perturbations is described by a complicated set of partial differential equations, which reveal that scalar, vectorial, and tensorial modes are coupled on inhomogeneous backgrounds. Recently, February et al. (2014) for the first time proposed a method for solving these equations numerically and calculated the evolution of linear perturbations for simplified toy models. Independently of these authors, we also developed a new framework for numerically solving the linear perturbation equations derived by Clarkson et al. (2009). Our code successfully reproduces the results published by February et al. (2014). Furthermore, we implemented a technique that allows us to seed the perturbation equations with realistic cosmological initial conditions for the Bardeen potentials

shortly after the time of decoupling. This step is almost finished and will soon be presented in a separate work (Meyer et al., in preparation).

Our numerical algorithm allows us to compute the linearly perturbed LTB metric at any space-time point (t, r, θ, ϕ) and, in particular, along the PNC of a fictitious observer placed in a LTB cosmology. We shall therefore be able to include additional cosmological observables that depend on the details of structure formation in future analyses of ΛLTB models.

One particular phenomenon that we have in mind is weak gravitational lensing. To our knowledge, up to now, there are no numerical studies of weak gravitational lensing in perturbed LTB backgrounds. A few works studied aspects of gravitational lensing in unperturbed LTB models (see e.g. Brouzakis et al. 2007; Fanizza & Nugier 2014). Only Dunsby et al. (2010) briefly discuss weak gravitational lensing in perturbed LTB models in the appendices of their work, but these authors do not present a numerical solution either. More importantly, their formalism for describing the evolution of linear perturbations in LTB cosmologies is substantially different from the perturbation theory developed by Clarkson et al. (2009).

In this chapter, we aim to sketch a simple framework for numerically studying weak gravitational lensing in perturbed LTB models. However, already here, we would like to stress that this chapter describes work in progress and should rather be considered as a preparatory step for future studies. We cannot yet numerically compute weak lensing spectra because we first need to finalise the code for solving the linear perturbation equations on LTB backgrounds. However, as soon as this goal has been accomplished, the formalism outlined below can readily be employed.

3.2 EQUATION OF GEODESIC DEVIATION

This section briefly discusses the evolution of optical properties along a bundle of null geodesics. We begin with the equation of geodesic deviation and finally arrive at the Sachs equation for the Jacobi map. Our presentation closely follows the articles by Bartelmann (2010b) and Clarkson et al. (2012), both of which are more rigorous and contain interesting additional details that we skipped for brevity.

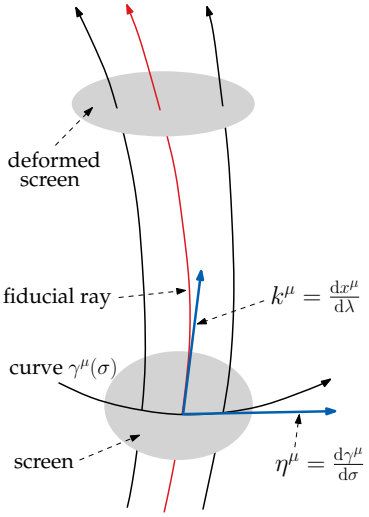

Figure 13: Evolution of a bundle of null geodesics.

Let us consider the evolution of a bundle of null-geodesics in an arbitrary space-time as illustrated in Fig. 13 and suppose that the light rays converge at a freely falling observer with four-velocity u^μ_{obs}. We select one of the light rays as a fiducial ray and parametrise it by the affine parameter λ, which can always be chosen such that the projection of the tangent vector $k^\mu = \frac{\mathrm{d}x^\mu}{\mathrm{d}\lambda}$ on the four-velocity u^μ_{obs} is unity at the time of observation, viz. $k_\mu u^\mu_{\mathrm{obs}} = 1$. This choice is beneficial mainly because then (a) the affine parameter coincides in an infinitesimal neighbourhood of the observation point with the Euclidean distance in the

rest frame of the comoving observer (which is important for the definition of observation angles; see below), and (b) the redshift with respect to the observer is given by $1+z = k_\mu u^\mu$, where u^μ is the four-velocity of a fictitious light source along the fiducial ray.

The space-like plane perpendicular to the four-velocity $u^\mu_{\rm obs}$ and the tangent vector k^μ defines the screen in the rest frame of the observer. The screen is spanned by the orthonormal vectors n^μ_a $(a = 1, 2)$, which are commonly called the Sachs basis. The basis vectors n^μ_a are parallel-transported along the fiducial ray $\left(k^\mu \nabla_\mu n^\nu_a = 0\right)$ and satisfy the relations $g_{\mu\nu} n^\mu_a n^\nu_b = \delta_{ab}$, $k_\mu n^\mu_a = 0$, $u_\mu n^\mu_a = 0$ (where u^μ denotes the four-velocity of comoving observers) for all λ.

Let us now envisage a curve $\gamma^\mu(\sigma)$ in the screen space and suppose that this curve connects the fiducial ray with its neighbouring geodesics. Since the Sachs basis is parallel-transported along the fiducial ray, the curve also remains in the screen space for all λ. The tangent vector $\eta^\mu = \frac{{\rm d}\gamma^\mu}{{\rm d}\sigma}$ measures the distance to neighbouring geodesics and hence also the physical size and shape of the bundle as one follows the fiducial light ray. The *equation of geodesic deviation* determines the evolution of the connecting vector η^μ along the fiducial ray,

$$k^\alpha k^\beta \nabla_\alpha \nabla_\beta \eta^\mu = R^\mu{}_{\nu\alpha\beta} k^\nu k^\alpha \eta^\beta \,, \tag{60}$$

where $R^\mu{}_{\nu\alpha\beta}$ denotes the Riemann curvature tensor. We can now expand the vector η^μ in the Sachs basis, $\eta^\mu = \eta_1 n^\mu_1 + \eta_2 n^\mu_2$, and substitute this representation into Eq. (60),

$$\frac{{\rm d}^2 \eta_a}{{\rm d}\lambda^2} = R_{\mu\nu\alpha\beta} n^\mu_a k^\nu k^\alpha n^\beta_b = \mathcal{T}_{ab} \eta_b \,. \tag{61}$$

In the second step, we introduced the optical tidal matrix $\mathcal{T}_{ab}$. It is convenient to decompose the Riemann curvature tensor into

$$R_{\alpha\beta\gamma\delta} = C_{\alpha\beta\gamma\delta} + g_{\alpha[\gamma} R_{\delta]\beta} - g_{\beta[\gamma} R_{\delta]\alpha} + \frac{R}{3} g_{\alpha[\gamma} g_{\delta]\beta} \tag{62}$$

where R, $R_{\alpha\beta}$ and $C_{\alpha\beta\gamma\delta}$ are, respectively, the Ricci scalar, the Ricci tensor and the Weyl curvature tensor (Straumann 2004). Using this decomposition, we rewrite the optical tidal matrix to

$$\mathcal{T}_{ab} = -\frac{1}{2} R_{\mu\nu} k^\mu k^\nu \delta_{ab} + C_{\mu\nu\alpha\beta} n^\mu_a k^\nu k^\alpha n^\beta_b \,. \tag{63}$$

While the Ricci focusing $R_{\mu\nu} k^\mu k^\nu$ is generated by matter inside the bundle, the Weyl focusing $C_{\mu\nu\alpha\beta} n^\mu_a k^\nu k^\alpha n^\beta_b$ is caused by matter outside the bundle, which can generate a non-vanishing Weyl curvature tensor along the fiducial ray (Clarkson et al. 2012).

The linearity of Eq. (61) together with the condition that the bundle of null geodesics converges at the observer $(\eta^\mu(\lambda)\,|_{\lambda=0} = 0)$ imply that the components of the connecting vector η^μ along the fiducial ray are related to the initial values of their derivatives by a linear transformation,

$$\eta_a(\lambda) = \mathcal{D}_{ab}(\lambda) \left.\frac{{\rm d}\eta_b(\lambda)}{{\rm d}\lambda}\right|_{\lambda=0} \,. \tag{64}$$

The *Jacobi map* $\mathcal{D}_{ab}$ describes the deformation of the light bundle as one follows the fiducial ray. From Eq. (61), we deduce that $\mathcal{D}_{ab}$ evolves according to

$$\frac{\mathrm{d}^2\mathcal{D}_{ab}(\lambda)}{\mathrm{d}\lambda^2} = \mathcal{T}_{ac}(\lambda)\,\mathcal{D}_{cb}(\lambda)\,, \qquad \left.\frac{\mathrm{d}\mathcal{D}_{ab}(\lambda)}{\mathrm{d}\lambda}\right|_{\lambda=0} = \delta_{ab}\,. \tag{65}$$

Equation (65) is called the *Sachs equation* for the Jacobi map and is of key importance for the following sections.

3.3 LINK WITH THE WEAK LENSING MAGNIFICATION MATRIX

The Jacobi map $\mathcal{D}_{ab}$ introduced in Eq. (64) is closely related to the Jacobian matrix $\mathcal{A}_{ab}$ of the lens mapping (cf. Bartelmann 2010b, Sect. 1.6), which is also commonly called (weak) lensing magnification matrix. We adopt the latter nomenclature in the following to clearly distinguish between $\mathcal{D}_{ab}$ and $\mathcal{A}_{ab}$.

Given our choice of the affine parameter λ $\left(k_\mu u^\mu_{\mathrm{obs}}\big|_{\lambda=0} = 1\right)$, we define the direction of observation with respect to the fiducial ray in the rest frame of the observer by

$$\theta_a = \left.\frac{\mathrm{d}\eta_a(\lambda)}{\mathrm{d}\lambda}\right|_{\lambda=0}\,. \tag{66}$$

Suppose that the ray observed in the angular direction $\boldsymbol{\theta}$ originated from a light source that, in the unlensed case, would appear at the angle

$$\beta_a = \frac{\eta_a(\lambda_\mathrm{s})}{D_\mathrm{A}(\lambda_\mathrm{s})} = \frac{\mathcal{D}_{ab}(\lambda_\mathrm{s})}{D_\mathrm{A}(\lambda_\mathrm{s})}\,\theta_b\,, \tag{67}$$

where $D_\mathrm{A}(\lambda_\mathrm{s})$ denotes the angular-diameter distance to the source. Equation (67) describes the linear relation between a variation of the viewing angle (with respect to the fiducial ray) and the resulting variation of the source position. Precisely this relation is described by the weak lensing magnification matrix, hence we find

$$\mathcal{A}_{ab} = \frac{\mathcal{D}_{ab}}{D_\mathrm{A}} = \begin{pmatrix} 1-\kappa-\gamma_1 & \gamma_2-\omega \\ \gamma_2+\omega & 1-\kappa+\gamma_1 \end{pmatrix}\,, \tag{68}$$

where we made the common decomposition of $\mathcal{A}_{ab}$ into the convergence κ, the shear (γ_1, γ_2), and the rotation ω. This decomposition (with $\omega = 0$) is applicable for central observers in FLRW and LTB cosmologies, which are the only cases that are discussed in the remainder of this work. In arbitrary space-times, it is more useful to relate the convergence, the shear, and the rotation to the Sachs optical scalars (Sachs 1961); see Clarkson et al. (2012) for a detailed derivation.

The above consideration highlights the importance of the Jacobi map for future weak-lensing studies in LTB cosmologies: the shear components, for instance, are given by $\gamma_1 = (\mathcal{D}_{22} - \mathcal{D}_{11})/(2D_\mathrm{A})$ and $\gamma_2 = (\mathcal{D}_{12} + \mathcal{D}_{21})/(2D_\mathrm{A})$. Therefore, as soon as we have solved for $\mathcal{D}_{ab}$ using Eq. (65) along the PNC, we can statistically correlate the shear at different viewing angles and lookback times λ, and compare the theoretically expected weak-lensing spectra with observed data to constrain LTB models.

3.4 WEAK LENSING IN PERTURBED FLRW MODELS

We now sketch the standard approach for solving the Sachs equation (65) on linearly perturbed FLRW backgrounds. Our presentation is deliberately brief; see Bartelmann (2010b) for a detailed derivation.

As already argued in Sect. 2.2, the large-scale matter distribution of the late Universe should well be described by a dust solution with zero pressure and zero anisotropic stress. Moreover, we restrict the following discussion to scalar perturbations, which are characterised by their (weak) Newtonian gravitational potential ϕ $\left(\phi = \Phi/c^2\right)$. In addition, we assume that the inhomogeneities are slowly moving, that is, their peculiar velocities with respect to the cosmic flow are small compared to the speed of light $(v \ll c)$. Under these assumptions, the linearly perturbed FLRW metric in the Newtonian gauge is

$$\mathrm{d}s^2 = a^2(\tau)\left[-(1+2\phi)\mathrm{d}\tau^2 + (1-2\phi)\left(\mathrm{d}w^2 + f_k^2(w)\mathrm{d}\Omega^2\right)\right] , \tag{69}$$

where τ is the conformal time $(a\mathrm{d}\tau = \mathrm{d}t)$ and the comoving angular-diameter distance $f_k(w)$ as a function of the comoving radial distance w is given by

$$f_k(w) = \begin{cases} \sqrt{k}\sin(\sqrt{k}w) & (k>0) \\ w & (k=0) \\ \frac{1}{\sqrt{-k}}\sinh(\sqrt{-k}w) & (k<0) \end{cases} . \tag{70}$$

Assuming that we can split the optical tidal matrix and the Jacobi map into a background and a first-order contribution, $\mathcal{T}_{ab} = \mathcal{T}^{(0)}_{ab} + \mathcal{T}^{(1)}_{ab}$ and $\mathcal{D}_{ab} = \mathcal{D}^{(0)}_{ab} + \mathcal{D}^{(1)}_{ab}$, the Sachs equation (65) reduces to

$$\frac{\mathrm{d}^2\mathcal{D}^{(0)}_{ab}(\lambda)}{\mathrm{d}\lambda^2} = \mathcal{T}^{(0)}_{ac}(\lambda)\,\mathcal{D}^{(0)}_{cb}(\lambda) , \tag{71}$$

$$\frac{\mathrm{d}^2\mathcal{D}^{(1)}_{ab}(\lambda)}{\mathrm{d}\lambda^2} = \mathcal{T}^{(0)}_{ac}(\lambda)\,\mathcal{D}^{(1)}_{cb}(\lambda) + \mathcal{T}^{(1)}_{ac}(\lambda)\,\mathcal{D}^{(0)}_{cb}(\lambda) . \tag{72}$$

Before we continue, we would like to stress a detail that might first appear trivial but is indeed an important simplification in comparison with radially inhomogeneous LTB models (cf. Sect. 3.5). From $k_\mu k^\mu = 0$ and $k_\mu u^\mu = (1+z) = a^{-1}$, we deduce that radial null geodesics satisfy

$$\mathrm{d}\tau = \mathrm{d}w, \quad \mathrm{d}\lambda = a^2\mathrm{d}\tau \quad \Rightarrow \quad \mathrm{d}\lambda = a^2\mathrm{d}w . \tag{73}$$

These relations show that we can trivially transform between τ, w, a, z, and λ along the fiducial light ray, which allows us to simply rewrite the Sachs equations in terms of either of these parameters. In what follows, we make use of the relation $\mathrm{d}\lambda = a^2\mathrm{d}w$ to rewrite the Sachs equations in terms of the comoving radial coordinate w instead of the affine parameter λ.

Let us first consider the unperturbed Sachs equation (71). Using Einstein's field equations, Eq. (71) can be brought to the form (cf. Bartelmann 2010b, Sect. 1.3)

$$\left(\frac{\mathrm{d}^2}{\mathrm{d}w^2} + k\right)\frac{D^{(0)}_{ab}}{a} = 0 , \tag{74}$$

which can readily be solved using the angular-diameter distance from Eq. (70),

$$D_{ab}^{(0)}(w) = a(w) f_k(w) \delta_{ab} = D_\mathrm{A}(w) \delta_{ab} \,. \tag{75}$$

The physical interpretation of this result is quite intuitive: At background level, the Weyl curvature tensor vanishes due to the symmetries of the FLRW metric. Light rays therefore only experience an isotropic Ricci focusing (if $\rho > 0$), and the diameter of light bundles scales with the angular-diameter distance.

To solve the first-order Sachs equation (72), we use Born's approximation: Complying with our prior assumption of weak gravitational potentials, we assume that the perturbations (e. g. deflection angles) along the line-of-sight are very small, and consequently the linear corrections to the Jacobi map can approximately be calculated by integrating along the unperturbed fiducial ray. Typically, Born's approximation is remarkably accurate (Bernardeau et al. 2010; Schäfer et al. 2012).

Given the solution of the Jacobi map at background level (Eq. (75)), the first-order Sachs equation (72) reduces to the simple form

$$\left(\frac{\mathrm{d}^2}{\mathrm{d}w^2} + k \right) \frac{D_{ab}^{(1)}(w)}{a(w)} = a(w) f_k(w) \mathcal{T}_{ab}^{(1)}(w) \,. \tag{76}$$

Equation (76) is a second-order linear differential equation with constant coefficient k. The Green's function to the linear operator $\left(\mathrm{d}^2/\mathrm{d}w^2 + k\right)$ is

$$G\left(w - w'\right) = \frac{1}{\sqrt{k}} \sin\left[\sqrt{k}\left(w - w'\right)\right] \Theta\left(w - w'\right) = f_k\left(w - w'\right) \Theta\left(w - w'\right) , \tag{77}$$

which allows us to write the solution of Eq. (76) in a closed-form expression,

$$\mathcal{D}_{ab}^{(1)} = \int_0^w f_k\left(w - w'\right) a\left(w'\right) f_k\left(w'\right) \mathcal{T}_{ab}^{(1)}\left(w'\right) \, \mathrm{d}w' \,. \tag{78}$$

The above integral is evaluated along the unperturbed fiducial ray due to Born's approximation. To calculate the linearly perturbed optical tidal matrix $\mathcal{T}_{ab}^{(1)}$ along the line-of-sight, we assume that the inhomogeneities are well localised and their spatial extent is much smaller than the curvature scale of the background universe. Then, spatial curvature does not influence the local perturbations, and the problem reduces to working out the Ricci and Weyl focussing terms in a perturbed FLRW metric (69) with $f_k(w) \approx w$. We find $\mathcal{T}_{ab}^{(1)} = -2\partial_a\partial_b\phi$, where ∂_x indicates differentiation along the Sachs basis vectors (i. e. perpendicular to the line-of-sight). Thus, the final solution for the Jacobi map is

$$\mathcal{D}_{ab} = D_\mathrm{A}(w)\delta_{ab} - 2\int_0^w f_k\left(w - w'\right) D_\mathrm{A}\left(w'\right) \partial_a\partial_b\phi\left(w'\right) \, \mathrm{d}w' \,. \tag{79}$$

This solves the basic lensing problem in perturbed FLRW models and usually serves as a starting point for the weak lensing formalism.

3.5 WEAK LENSING IN PERTURBED LTB MODELS

We can now try to reproduce the same approach as outlined in the previous section to solve for the Jacobi map in a linearly perturbed LTB model. Again, for simplicity, we restrict our discussion to slowly moving, weak scalar perturbations characterised by their Newtonian gravitational potential Φ. Then, the perturbed LTB metric in the Regge-Wheeler gauge is (Clarkson et al. 2009; February et al. 2013)

$$\mathrm{d}s^2 = -\left(1+2\Phi\right)\mathrm{d}t^2 + \left(1-2\Phi\right)\left[\frac{R'^2}{1+2E}\,\mathrm{d}r^2 + R^2\left(\mathrm{d}\theta^2+\sin^2\theta\,\mathrm{d}\phi^2\right)\right] . \tag{80}$$

Fluctuations in the gravitational potential Φ are naturally closely related to perturbations of the matter density field. Correspondingly, the perturbed energy-momentum tensor reads

$$T^{\mu\nu} = \rho\left(1+\Delta\right)u^\mu u^\nu , \tag{81}$$

where the gauge-invariant matter density perturbation Δ can be calculated by means of a generalised Poisson equation in LTB space-times (February et al. 2013).

For simplicity, but also to conserve isotropy, we only consider central LTB observers. Moreover, we again use Born's approximation and assume that the first-order contributions to the Jacobi map can be calculated by integrating along the unperturbed fiducial ray. In particular, we also neglect linear perturbations of the wave vector k^μ and the Sachs basis n_a^μ. As a first step, we thus need to find an appropriate set of differential equations that describes the evolution of the fiducial ray along the line-of-sight. From Sect. 1.4 and $k_\mu u^\mu = 1+z$, we deduce that radial null geodesics satisfy the following differential equations:

$$\frac{\mathrm{d}t}{\mathrm{d}\lambda} = -\left[1+z\left(\lambda\right)\right] , \qquad \left(t\left(\lambda\right)|_{\lambda=0} = t_0\right) \tag{82}$$

$$\frac{\mathrm{d}r}{\mathrm{d}\lambda} = \frac{\sqrt{1+2E\left[r\left(\lambda\right)\right]}}{R'\left[t\left(\lambda\right),r\left(\lambda\right)\right]}\left[1+z\left(\lambda\right)\right] , \qquad \left(r\left(\lambda\right)|_{\lambda=0} = 0\right) \tag{83}$$

$$\frac{\mathrm{d}z}{\mathrm{d}\lambda} = \left[1+z\left(\lambda\right)\right]^2 H_\mathrm{L}\left[t\left(\lambda\right),r\left(\lambda\right)\right] , \qquad \left(z\left(\lambda\right)|_{\lambda=0} = 0\right) \tag{84}$$

where we chose the affine parameter λ such that it increases monotonically as one follows the fiducial ray backwards in time, and $H_\mathrm{L} = \dot{R}'/R'$ is the longitudinal Hubble rate along the radial direction. Equations (82) - (84) highlight the first complication of the lensing formalism in LTB models: By construction, the Sachs equation (65) is a second-order differential equation in the affine parameter λ. In homogeneous FLRW models, we could trivially transform between w and λ along the PNC, which allowed us to simply rewrite the Sachs equation in terms of the comoving radial coordinate w. In radially inhomogeneous LTB models, the differential relations between t, r, z, and λ are more complicated because they depend not only on time, but also on the radial coordinate. There is no simple way to rewrite the Sachs equation in terms of the radial coordinate r, for instance. For the weak-lensing studies intended, it should therefore be beneficial to numerically integrate Eqs. (82) - (84) in terms of the monotonically

increasing affine parameter λ, tabulate intermediate values along the line-of-sight, and interpolate between the parameters t, r, z, and λ on the PNC.

As in the previous section, we now make the fundamental assumption that we can split the Jacobi map and the optical tidal matrix into a background and a first-order contribution. Again, we first solve the unperturbed Sachs equation (65). Just like in FLRW models, the Weyl focusing vanishes at background level. This can easily be understood because for central observers the LTB space-time looks isotropic and consequently, for symmetry reasons, the shear along radial geodesics must vanish. The unperturbed Sachs equation thus reads

$$\frac{\mathrm{d}^2 D^{(0)}_{ab}(\lambda)}{\mathrm{d}\lambda^2} = \mathcal{T}^{(0)}_{ac}(\lambda)\,\mathcal{D}^{(0)}_{cb}(\lambda) = -\frac{1}{2}R_{\mu\nu}k^\mu k^\nu\, D_{ab}(\lambda)\ , \tag{85}$$

which is solved by (see e.g. Dunsby et al. 2010; Clarkson et al. 2012)

$$D^{(0)}_{ab}(\lambda) = D_{\mathrm{A}}(\lambda)\,\delta_{ab}\ . \tag{86}$$

This is the same result as in the previous section: At background level, light bundles only experience an isotropic Ricci focusing. The convergence along the fiducial ray is described by the angular-diameter distance.

Next, we try to solve the first-order Sachs equation,

$$\frac{\mathrm{d}^2 \mathcal{D}^{(1)}_{ab}(\lambda)}{\mathrm{d}\lambda^2} = \mathcal{T}^{(0)}_{ac}(\lambda)\,\mathcal{D}^{(1)}_{cb}(\lambda) + \mathcal{T}^{(1)}_{ac}(\lambda)\,\mathcal{D}^{(0)}_{cb}(\lambda) \tag{87}$$

$$= -\frac{1}{2}R_{\mu\nu}(\lambda)\,k^\mu(\lambda)\,k^\nu(\lambda)\,\delta_{ac}\,\mathcal{D}^{(1)}_{cb}(\lambda) + \mathcal{T}^{(1)}_{ac}(\lambda)\ D_{\mathrm{A}}(\lambda)\,\delta_{cb} \tag{88}$$

$$= -4\pi G\,\rho(\lambda)\,[1+z(\lambda)]^2\,\mathcal{D}^{(1)}_{ab}(\lambda) + D_{\mathrm{A}}(\lambda)\,\mathcal{T}^{(1)}_{ab}(\lambda)\ , \tag{89}$$

where we inserted Einstein's field equations in the last step, which is possible because $k^\mu(\lambda)$ is a null vector. Equation (89) indicates the second complication of the lensing formalism in LTB models: In FLRW models, the Sachs equation could be brought to the simple form (76), which is a second-order linear differential equation with *constant* coefficient k. Such differential equations can be solved by means of analytically constructed Green's functions, which eventually allowed us to write the solution of the first-order Jacobi map as a simple line-of-sight integral (cf. Eq. (78)). In contrast, Eq. (89) is a second-order linear differential equation with *varying* coefficients, for which it is in general difficult to analytically construct a Green's function. Therefore, we cannot write the solution of Eq. (89) as a simple line-of-sight integral. Instead, we can only formulate the problem in terms of a system of coupled differential equations (Eqs. (82) - (84) and Eq. (89)) that need to be solved using an appropriate numerical integration scheme.

To this end, we finally have to calculate the first-order contributions to the optical tidal matrix $\mathcal{T}^{(1)}_{ab}$ along the unperturbed fiducial ray. In the equatorial plane ($\theta = \pi/2$), we find the following first-order components:

$$\mathcal{T}^{(1)}_{11}(\lambda) = 4\,[1+z(\lambda)]^2\left[\frac{4}{3}\pi G\rho(\lambda)\,\Phi(\lambda) - \frac{M(\lambda)}{R^3(\lambda)}\Phi(\lambda) - \pi G\rho(\lambda)\,\Delta(\lambda)\right] \tag{90}$$

$$-\frac{[1+z(\lambda)]^2}{R^2(\lambda)}\left(\frac{\partial^2}{\partial\theta^2} - \frac{\partial^2}{\partial\phi^2}\right)\Phi(\lambda)\ ,$$

$$\mathcal{T}_{22}^{(1)}(\lambda) = 4\left[1+z(\lambda)\right]^2\left[\frac{4}{3}\pi G\rho(\lambda)\Phi(\lambda) - \frac{M(\lambda)}{R^3(\lambda)}\Phi(\lambda) - \pi G\rho(\lambda)\Delta(\lambda)\right] + \frac{\left[1+z(\lambda)\right]^2}{R^2(\lambda)}\left(\frac{\partial^2}{\partial\theta^2} - \frac{\partial^2}{\partial\phi^2}\right)\Phi(\lambda)\ , \tag{91}$$

$$\mathcal{T}_{12}^{(1)}(\lambda) = \mathcal{T}_{21}^{(1)}(\lambda) = -\frac{2\left[1+z(\lambda)\right]^2}{R^2\left[t(\lambda), r(\lambda)\right]}\frac{\partial^2\Phi(\lambda)}{\partial\theta\partial\phi}\ . \tag{92}$$

Equations (90) - (92) reveal that fluctuations in the Newtonian gravitational potential Φ and the matter density Δ contribute to the isotropic focusing, while derivatives of the potential Φ perpendicular to the line-of-sight induce shear. The above components of the first-order optical tidal matrix can readily be substituted into Eq. (89), which shall allow us to numerically solve for the first-order Jacobi map and hence also to determine the convergence κ as well as the shear γ along the line-of-sight of a central observer in a linearly perturbed LTB space-time.

3.6 CONCLUSIONS AND OUTLOOK

In this chapter, we described a simple approach that could serve as a starting point for future studies of weak gravitational lensing in linearly perturbed LTB space-times within the gauge-invariant framework of Clarkson et al. (2009). We emphasised the main complications that arise due to the LTB metric being radially inhomogeneous but also showed that the first-order contributions to the Jacobi map can be calculated by means of a set of coupled ordinary differential equations.

Because we are still in the process of finalising our numerical code for solving the linear perturbation equations on LTB backgrounds with realistic cosmological initial conditions, we cannot yet present first numerical results. However, as soon as our numerical algorithm has been completed, we shall be able to calculate the Newtonian gravitational potential Φ and the matter density perturbation Δ at any space-time point (t, r, θ, ϕ), insert these quantities into Eqs. (90) - (92), and numerically calculate the linear corrections to the Jacobi map.

In future works, we intend to proceed as follows: In Meyer et al. (in preparation), the numerical framework for solving the linear perturbation equations will be presented in detail. Moreover, we intend to study the strength of the coupling between scalar, vectorial, and tensorial perturbation modes. If the coupling is strong, we additionally need to include the contributions due to vectorial and tensorial perturbations in the lensing formalism described in Sect. 3.5. However, this extension is straightforward because it essentially boils down to including vectorial and tensorial modes (at linear order) in the calculation of the perturbed optical tidal matrix (cf. Eqs. (90) - (92)). Alternatively, if the coupling is weak, it is probably well justified to study only the evolution of scalar perturbations (cf. February et al. 2013) and readily solve the system of coupled differential equations presented in Sect. 3.5.

Part II

THE STRONGEST GRAVITATIONAL LENSES

4

STRONG GRAVITATIONAL LENSING IN A NUTSHELL

ABSTRACT

Since the theory of strong gravitational lensing is well-known, we abstain from giving a detailed introduction here. Instead, we merely define the most important quantities required for our discussion of strong-lensing phenomena in the following chapters. First, we summarise the assumptions that justify the thin lens approximation. We then introduce the effective lensing potential and derive the convergence, the shear, and the magnification of the lens mapping. We discuss critical points of the lens mapping, which give rise to critical curves in the lens plane and caustics in the source plane. Finally, we define the lensing cross section and the Einstein radius, both of which are important concepts to characterise the strength of a gravitational lens.

This chapter closely follows the pedagogic lecture notes by Narayan & Bartelmann (1996). See also Schneider et al. (1992); Bartelmann (2010b) for comprehensive introductions to the theory of gravitational lensing.

4.1 THIN LENS APPROXIMATION

The typical strong-lensing scenario is illustrated in Fig. 14: A source (e. g. a galaxy) emits light that first propagates in unperturbed space-time, is then deflected in the vicinity of a gravitational lens (e. g. a galaxy cluster), and continues travelling through unperturbed space-time before reaching the observer, who perceives a (strongly) distorted image of the source. The deflection of light is described by the lens equation,

$$\boldsymbol{\beta} = \boldsymbol{\theta} - \boldsymbol{\alpha}(\boldsymbol{\theta}) \ , \tag{93}$$

where $\boldsymbol{\beta}$ and $\boldsymbol{\theta}$ denote, respectively, the angular position of the source and the distorted image, and $\boldsymbol{\alpha}(\boldsymbol{\theta})$ is the deflection angle at the position of the image.

In line with the assumptions of Sect. 3.4, we assume that the gravitational lens is slowly moving with respect to the reference frame of the CMB (peculiar velocity $v \ll c$) and induces only a weak perturbation of the background metric. Accordingly, the perturbation is well characterised by its Newtonian gravitational potential ϕ. Moreover, the spatial extent of the gravitational lens is typically much smaller than the distances between observer and lens and between lens and source. Most of the light deflection occurs within a tiny fraction Δz of the total line-of-sight. It is therefore well

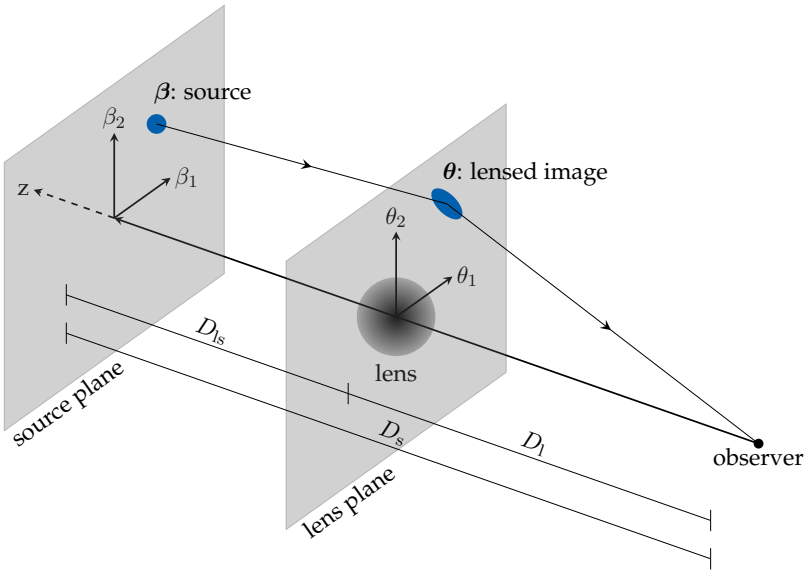

Figure 14: Illustration of light deflection due to the presence of a strong gravitational lens.

justified to use the *thin lens approximation*, which asserts that the spatial extent of the gravitational lens along the line-of-sight is completely negligible, and any deflection of light occurs in the *lens plane*. The gravitational lens is then fully specified by the line-of-sight projection of its Newtonian potential onto the lens plane (see Sect. 4.2). For simplicity, we additionally assume that the sources are located in a single plane, the so-called *source plane*. This is not a severe restriction because extended source redshift distributions can simply be accounted for by multiple source planes. Within these approximations, gravitational lensing essentially reduces to a simple (however non-linear) mapping between the lens plane and the source plane.

4.2 EFFECTIVE LENSING POTENTIAL

It is convenient to introduce the *effective lensing potential* $\psi(\boldsymbol{\theta})$, which is the appropriately scaled, projected Newtonian gravitational potential of the lens. In the thin lens approximation, the effective lensing potential is

$$\psi(\boldsymbol{\theta}) = 2\,\frac{D_{\mathrm{ls}}}{D_{\mathrm{l}} D_{\mathrm{s}}} \int \phi\left(D_{\mathrm{d}}\boldsymbol{\theta}, z\right)\,\mathrm{d}z\;, \tag{94}$$

where D_{l}, D_{s} and D_{ls} are, respectively, the angular-diameter distances to the lens, the source plane, and between lens and source plane. The deflection angle $\boldsymbol{\alpha}$ is the gradient of ψ with respect to $\boldsymbol{\theta}$ (Bartelmann 2010b). Thus, the lens equation (93) can be written as

$$\boldsymbol{\beta} = \boldsymbol{\theta} - \nabla_{\boldsymbol{\theta}}\,\psi(\boldsymbol{\theta})\;. \tag{95}$$

The local properties of the lens mapping are described by its Jacobian matrix $\mathcal{A}_{ij}$,

$$\mathcal{A}_{ij} = \frac{\partial\boldsymbol{\beta}}{\partial\boldsymbol{\theta}} = \left(\delta_{ij} - \frac{\partial^2\psi(\boldsymbol{\theta})}{\partial\theta_i\partial\theta_j}\right) = \begin{pmatrix} 1-\kappa-\gamma_1 & -\gamma_2 \\ -\gamma_2 & 1-\kappa+\gamma_1 \end{pmatrix}\;, \tag{96}$$

where we decomposed the Jacobian matrix into the convergence κ and the shear γ (cf. decomposition of the Jacobi map, Sect. 3.3).

We can use Poisson's equation to relate the *convergence* $\kappa = (\psi_{11} + \psi_{22})/2$ to the projected surface mass density $\Sigma(\boldsymbol{\theta})$,

$$\kappa(\boldsymbol{\theta}) = \frac{1}{2}\nabla_{\boldsymbol{\theta}}^2\psi(\boldsymbol{\theta}) = \frac{D_\mathrm{l}D_\mathrm{ls}}{D_\mathrm{s}}\int \nabla_x^2\phi(D_\mathrm{d}\boldsymbol{\theta}, z)\,\mathrm{d}z \tag{97}$$

$$= \frac{D_\mathrm{l}D_\mathrm{ls}}{D_\mathrm{s}}\int 4\pi G\rho(D_\mathrm{d}\boldsymbol{\theta}, z)\,\mathrm{d}z = \frac{D_\mathrm{l}D_\mathrm{ls}}{D_\mathrm{s}}\,4\pi G\,\Sigma(\boldsymbol{\theta}) \tag{98}$$

$$= \frac{\Sigma(\boldsymbol{\theta})}{\Sigma_\mathrm{crit}}\,, \tag{99}$$

where we first assumed that the z-component of the Poisson equation is negligible when integrating along the line-of-sight (due to the boundary conditions) and introduced the critical surface mass density $\Sigma_\mathrm{crit} \equiv (4\pi G)^{-1} D_\mathrm{s}(D_\mathrm{l}D_\mathrm{ls})^{-1}$ in the last step. The *shear* components can be written as

$$\gamma_1 = \frac{1}{2}(\psi_{11} - \psi_{22}), \quad \gamma_2 = \psi_{12} = \psi_{21} \qquad \Rightarrow \qquad \gamma = \sqrt{\gamma_1^2 + \gamma_2^2}\,. \tag{100}$$

As illustrated in Fig. 15, convergence causes an isotropic focusing of the light rays (cf. Ricci focusing, Sect. 3.2); consequently, the observer perceives an isotropically magnified image of the source. Shear causes an anisotropic distortion of the image along a preferred direction; initially circular sources are imaged as elliptical objects on the observer's sky.

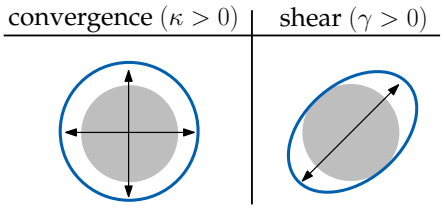

Figure 15: Illustration of image distortions due to convergence and shear.

The *magnification* μ of the lens mapping is given by

$$\mu = \frac{1}{\det \mathcal{A}_{ij}} = \frac{1}{\lambda_t\lambda_r} = \frac{1}{\left[(1-\kappa)^2 - \gamma^2\right]}\,. \tag{101}$$

In Eq. (101), we used the relation $\det \mathcal{A}_{ij} = \lambda_t\lambda_r$, where λ_t and λ_r are, respectively, the the tangential and radial eigenvalues of the Jacobian matrix,

$$\lambda_t = 1 - \kappa - \gamma, \qquad \lambda_r = 1 - \kappa + \gamma\,. \tag{102}$$

4.3 CRITICAL POINTS OF THE LENS MAPPING

Strong gravitational lensing of extended sources gives rise to spectacular image distortions: Originally circular sources can appear as highly elongated, thin arcs, which are commonly called (giant) gravitational arcs. Observers may see multiple images of a single source. Or, in the case of an axially symmetric lens, a source can even be imaged as a closed ring, called Einstein ring (cf. Sect. 4.5).

Strong-lensing phenomena occur close to *critical points* of the lens mapping, which are points in the lens plane where at least one eigenvalue vanishes. Equation (101) indicates that the magnification of the lens mapping formally diverges at these

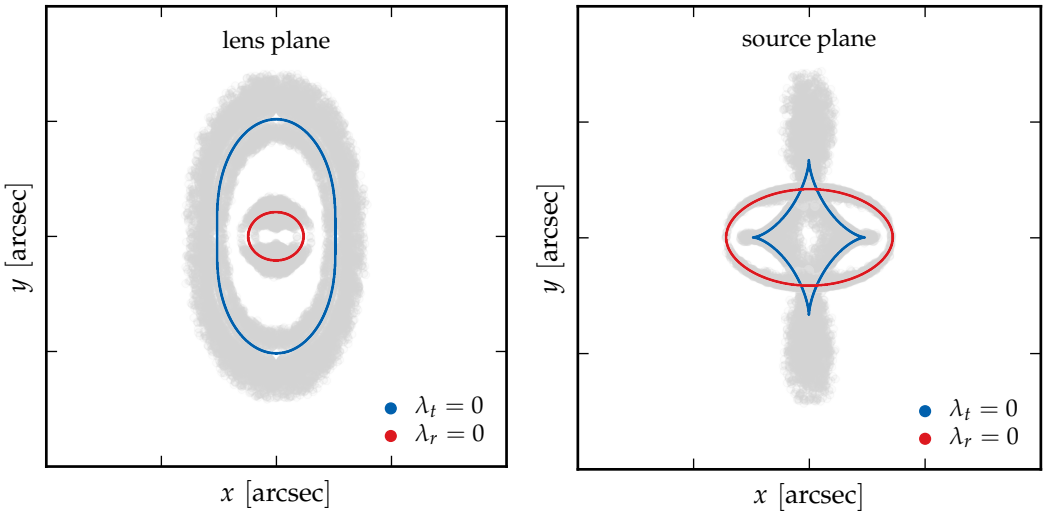

Figure 16: Illustration of the critical curves (left figure) and the caustics (right figure) of an exemplary gravitational lens with an elliptical surface mass density profile. The grey-shaded area in the left figure indicates the region in which gravitational arcs with length-to-width ratio larger than 7.5 can occur. The grey-shaded region in the right figure indicates the lensing cross section $\sigma_{7.5}$ (cf. Sect. 4.4).

points. This is, however, only true for idealised point sources; extended sources may be strongly – but certainly not infinitely – magnified. We can refine the previous definition of critical points by amending that points in the lens plane where the tangential (radial) eigenvalue vanishes are called tangential (radial) critical points. This refined nomenclature was originally introduced for axially symmetric lenses, where images close to the tangential (radial) critical curves are highly elongated along the tangential (radial) direction. Nonetheless, the distinction between tangential and radial critical points is also useful for more general lenses whose mass distribution is not exactly axially symmetric.

As visualised in Fig. 16, the set of critical points forms closed curves, which are called *critical curves*. Their images (under the lens mapping) on the source plane are called *caustics*. Sources located close to caustics are strongly magnified by the lens mapping. A galaxy that lies on top of the tangential caustic, for instance, is likely to appear as highly elongated image in the vicinity of the tangential critical curve (cf. grey-shaded region in Fig. 16).

4.4 LENSING CROSS SECTION

The *lensing cross section* σ_p is an important quantity to measure the strong-lensing efficiency of a lens. It is formally defined as the area of the region on the source plane where a source with given characteristics (morphology, orientation, surface brightness profile, etc.) has to lie in order to produce at least one image with properties p. This definition is obviously quite general and needs to be further specified for applications in the following chapter. Throughout, we exclusively compute the lensing cross section $\sigma_{7.5}$, which measures the efficiency of a gravitational lens to produce highly elongated

images (i. e. giant arcs) with length-to-width ratios exceeding 7.5. Given our remarks of the previous section, the area contributing to the lensing cross section $\sigma_{7.5}$ should be concentrated around the caustics in the source plane; this assumption is indeed confirmed by the grey-shaded region in the right panel of Fig. 16.

In Redlich et al. (2012), we described in detail three different methods for computing the lensing cross section $\sigma_{7.5}$ of a gravitational lens. All results presented in the remainder of this work were computed with a ray-tracing technique, named "method B" in Redlich et al. (2012). Briefly, this method works as follows: The source plane is covered with a Cartesian grid, which is adaptively refined close to the caustics. The algorithm then loops over each grid cell and places an extended elliptical source (with random orientation and random minor-to-major axis ratio) at the cell centre. The lensed image(s) of the source is (are) simulated using a ray-tracing technique, following bundles of light rays through the lens plane. If at least one of the simulated images has a length-to-width ratio exceeding 7.5, the (appropriately weighted) area of the grid cell in the source plane is added to the lensing cross section $\sigma_{7.5}$.

After looping over all grid cells in the source plane, and assuming that the resolution of the adaptive grid was sufficiently high, one ends up with an accurate estimate of the lensing cross section $\sigma_{7.5}$. Since the randomly sampled properties of the individual sources affect the length-to-width ratio of the lensed image – and therefore also whether or not the considered grid cell is added to the lensing cross section – it is perhaps useful to think of the technique as a kind of MC integration of the lensing cross section, which explains the fluctuations visible in Fig. 16.

See Redlich et al. (2012), and references therein, for a detailed introduction of the three different methods for computing lensing cross sections, in particular regarding the algorithmic measurement of the length-to-width ratio of lensed images and the statistical modelling of the source population.

4.5 EINSTEIN RADIUS

The second important concept to characterise the strength of a gravitational lens is the Einstein radius, which measures the size of the tangential critical curve. The statistics of the largest Einstein radii in the observable Universe is a valuable cosmological probe; this is the key issue of the following chapters.

The Einstein radius was originally defined for axially symmetric lenses, which exhibit circular tangential critical curves. Following Schneider et al. (1992), we first write the shear of an axially symmetric lens as

$$\gamma(\theta) = \overline{\kappa}(\theta) - \kappa(\theta) \ , \tag{103}$$

where $\overline{\kappa}(\theta)$ denotes the mean convergence within a circle of radius θ. Substituting this relation into Eq. (102), and recalling that the tangential eigenvalue vanishes at points belonging to the tangential critical curve, we find

$$\lambda_t(\theta_{\mathrm{E}}) = 1 - \overline{\kappa}(\theta_{\mathrm{E}}) \stackrel{!}{=} 0 \ . \tag{104}$$

Accordingly, the Einstein radius θ_{E} is defined as the radius of the circle enclosing a mean convergence of unity. Using the above relation (97) between the convergence and the surface mass density, we can formulate the definition of θ_{E} as

$$\overline{\kappa}\left(\theta_{\mathrm{E}}\right) = \frac{\overline{\Sigma}\left(\theta_{\mathrm{E}}\right)}{\Sigma_{\mathrm{crit}}} = 1\,, \tag{105}$$

implying that the mean surface mass density $\overline{\Sigma}\left(\theta_{\mathrm{E}}\right)$ within the Einstein radius equals the critical surface mass density. This highlights two important details: (1) in the limiting case of axial symmetry, only very massive objects (such as galaxy clusters) with supercritical surface mass density can act as strong gravitational lenses, and (2) generally, the size of the Einstein radius encodes important information about the concentration of the inner surface mass density profile.

While the definition of the Einstein radius is quite natural in the case of axially symmetric lenses, observed gravitational lenses or numerically simulated clusters exhibit highly asymmetric and irregularly shaped tangential critical curves (Zitrin et al. 2011; Meneghetti et al. 2011). It is therefore not obvious how the notion of an Einstein radius can be generalised to more realistic lenses. Amongst the various alternatives proposed in the literature (see e.g. Broadhurst & Barkana 2008; Oguri & Blandford 2009; Zitrin et al. 2011; Meneghetti et al. 2011), the following geometrically motivated definition turned out to be most useful for our purposes.

Let A denote the area enclosed by the tangential critical curve of an arbitrary gravitational lens. The *effective Einstein radius* θ_{eff} of this lens is then defined by

$$\theta_{\mathrm{eff}} \equiv \sqrt{\frac{A}{\pi}}\,, \tag{106}$$

so that a circle with radius θ_{eff} has the same area A. We adopt this definition throughout the remainder of this work.

5

THE STATISTICAL IMPACT OF CLUSTER MERGERS

ABSTRACT

For more than a decade now, it has been controversial whether or not the high rate of giant gravitational arcs and the largest observed Einstein radii are consistent with the standard cosmological model. Recent studies indicate that mergers provide an efficient mechanism to substantially increase the strong-lensing efficiency of individual clusters. Based on semi-analytic methods, we investigate the statistical impact of cluster mergers on the distribution of the largest Einstein radii and the optical depth for giant gravitational arcs of selected cluster samples. Analysing representative all-sky realizations of clusters at redshifts $z < 1$ and assuming a constant source redshift of $z_s = 2$, we find that mergers increase the number of Einstein radii above $10''$ ($20''$) by $\sim$35% ($\sim$55%). Exploiting the tight correlation between Einstein radii and lensing cross sections, we infer that the optical depth for giant gravitational arcs with a length-to-width ratio ≥ 7.5 of those clusters with Einstein radii above $10''$ ($20''$) increases by $\sim$45% ($\sim$85%). Our findings suggest that cluster mergers significantly influence in particular the statistical lensing properties of the strongest gravitational lenses. We conclude that semi-analytic studies must inevitably take these events into account before questioning the standard cosmological model on the basis of the largest observed Einstein radii and the statistics of giant gravitational arcs.

The contents of this chapter were published in Redlich et al. (2012). Sections that were part of the author's diploma thesis were removed here. In some paragraphs, we therefore refer to Redlich et al. (2012) for more details.

5.1 INTRODUCTION

Both the distribution of Einstein radii and the abundance of gravitational arcs probe the strong-lensing efficiency of galaxy clusters and are thus valuable cosmological probes (Bartelmann 2010b). Therefore, the result of Bartelmann et al. (1998), who reported that we observe ten times as many giant gravitational arcs on the sky as theoretically expected, poses a serious challenge. Various aspects of strong gravitational lensing that could potentially mitigate the tension between theory and observations were studied in a long series of subsequent works; see Sect. 5.2 of Bartelmann (2010b) or Meneghetti et al. (2013) for comprehensive reviews. Here, we only summarise those works particularly relevant for this chapter.

Analysing numerically simulated mergers of galaxy clusters, Torri et al. (2004) found that mergers substantially change the shape of the critical curves and can boost a cluster's efficiency to produce giant arcs by an order of magnitude. Fedeli et al. (2006) employed semi-analytic methods to estimate that mergers approximately double the statistical strong-lensing efficiency of clusters at redshifts $z > 0.5$. These authors argued that mergers might possibly explain the excess of gravitational arcs in observed galaxy clusters at moderate and high redshifts. However, Fedeli et al. (2006) made several simplifying assumptions that we revise here: First, galaxy clusters were described by elliptically distorted spherical lens models instead of adopting more realistic triaxial density profiles (Jing & Suto 2002; Oguri et al. 2003). This approximation reduces the required computing time substantially, since the calculation of deflection angles for triaxial density profiles involves numerical integrations (Schramm 1990), while simple analytic expressions exist in the case of elliptically distorted density profiles (Schneider et al. 1992). Second, all mergers were simulated with a fixed direction of motion and relative orientation of the merging clusters, neglecting two important degrees of freedom (Redlich et al. 2012).

Furthermore, recent studies indicate that the distribution of Einstein radii might also be in conflict with theory. More precisely, the largest observed Einstein radii (e.g. Halkola et al. 2008; Umetsu & Broadhurst 2008; Zitrin et al. 2011) were claimed to exceed the maximum possible expectations of the standard cosmological model (Broadhurst & Barkana 2008; Oguri & Blandford 2009; Meneghetti et al. 2011). These conclusions were drawn by either comparing the largest observed Einstein radii to those found in numerical simulations or by semi-analytically estimating the probability of finding the strongest observed lens systems in a ΛCDM universe. While studies of Einstein radii in numerical simulations are probably most realistic, they always suffer from a limited sample size. The simulated boxes might simply be too small to contain a sufficient number of extraordinarily strong gravitational lenses, which forbids solid statistical conclusions. In Chap. 6, we show that this limitation is indeed decisive in the context of extreme value statistics. Semi-analytic methods – admittedly based on a set of simplifying assumptions – can overcome this limitation because they are computationally less demanding and hence can be used to analyse large samples of particularly strong gravitational lenses within a comparably short time. However, we note that so far all semi-analytic studies of cosmological distributions of Einstein radii have only considered samples of isolated galaxy clusters. One important goal of this chapter is to extend these previous approaches and to present a new semi-analytic method for studying distributions of Einstein radii that incorporates the impact of cluster mergers.

Findings of Meneghetti et al. (2011) suggest that the excess of giant arcs and the problem of too large Einstein radii are closely related. Analysing selected samples of strong gravitational lenses in the MareNostrum simulation (Gottlöber & Yepes 2007), Meneghetti and collaborators discovered a remarkably tight correlation between lensing cross sections and Einstein radii of cluster-sized dark matter haloes. The correlation discovered by Meneghetti et al. (2011) plays an important role for the line of reasoning of this work, and eventually justifies why we can focus on the statistics of the largest Einstein radii in Chaps. 6 - 8.

This chapter is structured as follows: In Sect. 5.2, we introduce the semi-analytic model of triaxial gravitational lenses that we adopt in the remainder of this work. In Sect. 5.3, we use a simple toy model to illustrate the importance of mergers for the strong-lensing efficiency of individual clusters. Section 5.4 describes methods for sampling representative cosmological distributions of triaxial dark matter haloes and, in particular, introduces our new semi-analytic method for populating the PNC of a fictitious observer with merging galaxy clusters. In Sect. 5.5, we compute the impact of cluster mergers on the statistics of the largest Einstein radii and the optical depth for giant gravitational arcs of a selected cluster sample. Our conclusions are presented in Section 5.6.

Throughout this chapter, we adopt the best-fitting cosmological parameters obtained from the Wilkinson Microwave Anisotropy Probe seven-year data (WMAP7; Larson et al. 2011), $(\Omega_{\Lambda 0}, \Omega_{\mathrm{m}0}, \Omega_{\mathrm{b}0}, h, \sigma_8) = (0.727, 0.273, 0.0455, 0.704, 0.811)$.

5.2 TRIAXIAL GRAVITATIONAL LENSES

5.2.1 *Density profile of triaxial dark matter haloes*

Jing & Suto (2002, hereafter JS02) performed a detailed analysis of the density profiles of dark matter haloes found in large cosmological simulations. These authors suggested that the universal, spherical density profile discovered by Navarro et al. (1996, hereafter NFW) can be generalized to a triaxial model and showed that this generalization significantly improves the fit to simulated haloes. Moreover, by analysing large cluster populations in their cosmological simulations, JS02 derived probability density functions for the profile concentrations and axis ratios of triaxial dark matter haloes. The statistical description provided in JS02 allows constructing random catalogues of triaxial dark matter haloes that resemble realistic cosmological populations in numerical simulations.

Jing & Suto (2002) parametrized the spatial density profile of a triaxial dark matter halo by means of Cartesian coordinates $\boldsymbol{x'} = (x', y', z')$ in the principal axis frame. Using this parametrisation, they proposed a generalization of the NFW density profile,

$$\rho(R) = \frac{\delta_{\mathrm{ce}}\, \rho_{\mathrm{crit}}(z)}{(R/R_0)^{\alpha}(1 + R/R_0)^{3-\alpha}} \,, \tag{107}$$

$$R^2 \equiv \frac{x'^2}{(a/c)^2} + \frac{y'^2}{(b/c)^2} + z'^2 \qquad (a \leq b \leq c) \,, \tag{108}$$

where z denotes the halo redshift, R_0 is the scale radius (cf. Eq. (117)), δ_{ce} is the characteristic density (cf. Eq. (118)), $\rho_{\mathrm{crit}}(z)$ denotes the critical density of the universe, and a, b, and c are the lengths of the semi-principal axes. The exact numerical value of the inner slope α of the density profile is still being discussed. While NFW originally proposed $\alpha = 1.0$, other authors argued that steeper profiles with values up to $\alpha = 1.5$ provide a better fit to observations and numerical simulations (Moore et al. 1999; Jing & Suto 2000; Power et al. 2003; Navarro et al. 2004; Limousin et al. 2008). In contrast, recent combined strong- and weak-lensing analyses of selected clusters indicate shallower mass profiles with inner slopes $\alpha < 1$ (see Newman et al. 2011, for

instance). Following Oguri et al. (2003), we consider both $\alpha = 1.0$ and $\alpha = 1.5$ to cover a broad range of the predicted values, and to discuss some consequences of varying inner slopes on strong-lensing statistics.

To draw a random triaxial dark matter halo of virial mass M at redshift z, we first sample its axis ratios using the empirically derived probability density functions from JS02,

$$p(a/c) = \frac{1}{\sqrt{2\pi}\sigma_s} \exp\left[-\frac{(a_{sc} - 0.54)^2}{2\sigma_s^2}\right] \frac{da_{sc}}{d(a/c)}\,, \tag{109}$$

$$p(a/b \,|\, a/c) = \frac{3}{2(1 - r_{min})}\left[1 - \left(\frac{2a/b - 1 - r_{min}}{1 - r_{min}}\right)^2\right]\,, \tag{110}$$

where the best-fitting parameter for the width of the axis ratio distribution $p(a/c)$ is $\sigma_s = 0.113$ (JS02), Eq. (110) holds for $a/b \geq r_{min}$ and is zero otherwise, and

$$a_{sc} = \frac{a}{c}\left(\frac{M}{M_*}\right)^{0.07[\Omega_m(z)]^{0.7}}\,, \qquad r_{min} = \max\left(a/c, 0.5\right)\,. \tag{111}$$

Here, M_* is the characteristic non-linear mass scale where $\sigma(M_*, z) = \delta_c(z)$.

The concentration c_e of the halo is defined by $c_e \equiv R_e/R_0$, where R_e is determined such that the mean density within the ellipsoid of the major axis radius R_e equals $\Delta_e(z)\Omega(z)\rho_{crit}(z)$, where

$$\Delta_e(z) = 5\Delta_{vir}(z)\left(\frac{c^2}{ab}\right)^{0.75}\,. \tag{112}$$

$\Delta_{vir}(z)$ is the overdensity of objects virialized at redshift z, which we approximate according to Nakamura & Suto (1997). JS02 found a log-normal distribution for the concentration,

$$p\left(c_e\right) = \frac{1}{\sqrt{2\pi}\sigma_c} \exp\left\{-\frac{[\ln(c_e) - \ln(\bar{c}_e)]^2}{2\sigma_c}\right\}\frac{1}{c_e}\,, \tag{113}$$

with a dispersion of $\sigma_c = 0.3$. Following Oguri et al. (2003), we include a correlation between the axis ratio a/c and the mean concentration,

$$\bar{c}_e = f_c\, A_e \sqrt{\frac{\Delta_{vir}(z_c)}{\Delta_{vir}(z)}}\left(\frac{1 + z_c}{1 + z}\right)^{3/2}\,, \tag{114}$$

$$f_c = \max\left\{0.3, 1.35\exp\left[-\left(\frac{0.3}{a_{sc}}\right)^2\right]\right\}\,. \tag{115}$$

In Eq. (115), we adopted a correction introduced by Oguri & Blandford (2009), forcing $f_c \geq 0.3$ to avoid unrealistically low concentrations for particularly low axis ratios a_{sc}. Additionally, as noted earlier by Oguri & Keeton (2004), triaxial haloes with particularly low axis ratios a_{sc} (and hence also low concentrations c_e) are highly elongated objects whose lens potential is dominated by masses well outside the virial radius. Previous studies tried to avoid these unrealistic scenarios by simply truncating

the density profile outside the virial radius (Baltz et al. 2009; Oguri & Blandford 2009). In contrast, we employ a statistically motivated approach and suppress particularly small axis ratios from the tail of the underlying distribution. More precisely, if not stated otherwise, we force all sampled axis ratios $a_{\rm sc}$ to lie within the 99% confidence interval of the axis ratio distribution (109). We investigate the impact of this truncation on the statistics of the largest Einstein radii in Sect. 6.3.2. The numerical value of the free parameter $A_{\rm e}$ depends on the underlying cosmology. Again, if not stated otherwise, we set $A_{\rm e} = 1.1$, which was proposed by JS02 for a standard ΛCDM model. The above expressions only apply to an inner slope of $\alpha = 1.0$. In the case of $\alpha = 1.5$, we use the simple relation $\bar{c}_{\rm e}(\alpha = 1.5) = 0.5 \times \bar{c}_{\rm e}(\alpha = 1.0)$ (Keeton & Madau (2001); JS02). Finally, $z_{\rm c}$ denotes the typical collapse redshift of a dark matter halo of mass M and is computed using the complementary error function together with the condition

$$\mathrm{erfc}\left\{\frac{\omega(z_{\rm c})-\omega(0)}{\sqrt{2\left[\sigma^2(fM)-\sigma^2(M)\right]}}\right\} = \frac{1}{2}\,. \tag{116}$$

Here, $\sigma^2(M)$ is the top-hat smoothed variance of the power-spectrum extrapolated to the redshift $z = 0$ and $\omega(z) = \delta_{\rm c}(z)/D(z)$, where $D(z)$ is the linear growth factor. Following JS02, we adopt $f = 0.01$. The typical collapse redshift can be derived within the framework of the extended Press-Schechter theory (Lacey & Cole 1993). It corresponds to the typical time when the most massive progenitor of a dark matter halo contained the mass fraction fM. However, note that JS02 defined the typical collapse redshift such that it does not depend on the halo's actual redshift.

All other profile parameters can be inferred from the axis ratios and the concentration. Using an empirical relation (found by JS02) between $R_{\rm e}$ and the spherical virial radius $r_{\rm vir}$, $R_{\rm e}/r_{\rm vir} \approx 0.45$, the scale radius R_0 is given by

$$R_0 = 0.45\,\frac{r_{\rm vir}}{c_{\rm e}} = \frac{0.45}{c_{\rm e}}\left[\frac{3M}{4\pi\Delta_{\rm vir}(z)\Omega_{\rm m}(z)\rho_{\rm crit}(z)}\right]^{1/3}\,. \tag{117}$$

Finally, the characteristic density $\delta_{\rm ce}$ of the density profile (107) is defined in terms of the concentration,

$$\delta_{\rm ce} = \frac{\Delta_{\rm e}(z)\Omega_{\rm m}(z)}{3}\,\frac{c_{\rm e}^3}{m(c_{\rm e})}\,, \tag{118}$$

where

$$m(c_{\rm e}) = \begin{cases} \ln\left(1+c_{\rm e}\right) - \dfrac{c_{\rm e}}{1+c_{\rm e}} & (\alpha = 1.0) \\ 2\ln\left(\sqrt{c_{\rm e}} + \sqrt{1+c_{\rm e}}\right) - 2\sqrt{\dfrac{c_{\rm e}}{1+c_{\rm e}}} & (\alpha = 1.5) \end{cases}\,. \tag{119}$$

5.2.2 *Gravitational lensing by triaxial dark matter haloes*

Equation (107) defines the density profile of a triaxial dark matter halo in its principal axis frame. To evaluate the strong-lensing signal of an arbitrarily oriented halo,

however, we need to project its spatial density profile along the observer's line-of-sight. We therefore need to introduce an appropriate coordinate transformation between the principal axis frame of the halo and the reference frame of the observer.

Adopting the notation of Eq. (107), $\boldsymbol{x'} = (x', y', z')$ denote the Cartesian coordinates in the principal axis frame of the halo, so that the z'-axis lies along the major axis of the ellipsoid. Moreover, we assume that the z-axis is aligned with the observer's line-of-sight direction. Then, we can locally construct another Cartesian frame for the observer's coordinate system, denoted by $\boldsymbol{x} = (x, y, z)$. The origins of both coordinate systems are placed at the centre of the halo. A general coordinate transformation between the two frames can then be parametrised by three Euler angles (ψ, θ, ϕ). We adopt the so-called z-x'-z''-convention: We first rotate about the z-axis by the angle ψ, then about the new x'-axis by the angle θ, and finally about the new z''-axis by the angle ϕ. The transformation is then simply given by $\boldsymbol{x'} = \boldsymbol{R}\boldsymbol{x}$, with

$$\boldsymbol{R} \equiv \begin{pmatrix} \cos\phi & \sin\phi & 0 \\ -\sin\phi & \cos\phi & 0 \\ 0 & 0 & 1 \end{pmatrix} \begin{pmatrix} 1 & 0 & 0 \\ 0 & \cos\theta & \sin\theta \\ 0 & -\sin\theta & \cos\theta \end{pmatrix} \begin{pmatrix} \cos\psi & \sin\psi & 0 \\ -\sin\psi & \cos\psi & 0 \\ 0 & 0 & 1 \end{pmatrix} \tag{120}$$

Using this coordinate transformation, we can express the density profile of an arbitrarily oriented triaxial dark matter halo in terms of the observer's coordinates.

From here on, the derivation of all lensing properties (deflection angles, eigenvalues of the lens map, etc.) of triaxial dark matter haloes is identical to that given by Oguri et al. (2003), hence we refer the reader to their work. We note, however, that the coordinate transformation introduced above is more general than that used by Oguri et al. (2003) because for mergers, the relative orientation of the merging haloes in the x–y-plane is important, while Oguri et al. (2003) only considered isolated haloes whose orientation in the x–y-plane can be fixed at will. Therefore, some algebraic coefficients are more complicated in our approach. See the Appendix of Redlich et al. (2012) for the relevant expressions and a method for speeding up the numeric computation of deflection angles.

In the following sections, we analyse strong-lensing properties of randomly drawn cosmological populations of triaxial dark matter haloes. Therefore, we also need to sample random halo orientations. For that purpose, special care must be taken, since we cannot simply uniformly distribute the three angles (ψ, θ, ϕ) in the corresponding angle bins. Instead, we have to apply the correct *Haar measure* (Haar 1933). Only ψ and ϕ can be uniformly distributed in the range $[0, 2\pi]$. To sample θ, we first draw a uniformly distributed random number r in the range $[0, 1)$ and then compute

$$\theta = \arccos(1 - 2r) \,. \tag{121}$$

5.2.3 *Correlation between Einstein radii and lensing cross sections*

Performing a statistical analysis of strong lenses extracted from the MareNostrum Universe (Gottlöber & Yepes 2007), Meneghetti et al. (2011) found a remarkably tight correlation between lensing cross sections $\sigma_{7.5}$ and Einstein radii θ_{E}. The correlation

is well described by a linear relation in the $\log(\theta_E) - \log(\sigma_{7.5})$ plane, $\log(\sigma_{7.5}) = a \log(\theta_E) + b$, where a and b are free parameters that need to be fitted to the data.

In Redlich et al. (2012), we demonstrated that the tight correlation between lensing cross sections and Einstein radii can be reproduced with the semi-analytic model of triaxial gravitational lenses presented in Sect. 5.2.1. Moreover, we investigated the functional form of the correlation for different cosmologies and varying properties of the triaxial density profile, finding that the simple linear relation was remarkably accurate in all cases considered as long as the lenses were sufficiently strong ($\theta_E \gtrsim 10''$).

As already noted by Meneghetti et al. (2011), the tight correlation between Einstein radii and lensing cross sections clearly indicates the strong connection between the problem of too large Einstein radii and the arc statistics problem. A particularly strong gravitational lens, whose Einstein radius is too large for the ΛCDM model, will most likely also have a lensing cross section that exceeds the maximum theoretical expectations. Hence, if we were to observe too large Einstein radii, we would also expect an excess of gravitational arcs. Vice versa, if the largest observed Einstein radii were consistent with the ΛCDM model, the abundance of gravitational arcs *in the strongest lenses* should not exceed the theoretical expectations either. On the other hand, we note that care must be taken because both problems are not exactly identical. Even if there were a way to explain the *strongest lenses* with particularly large Einstein radii within the ΛCDM model, this would not necessarily solve the arc statistics problem. While the distribution of largest Einstein radii only tests the extreme cases, an arc statistic additionally measures the cumulative lensing efficiency of the entire halo population, so that it is also sensitive to the pure abundance of relatively unspectacular lenses, for instance. Thus, if the observed Universe simply contained more strong gravitational lenses than theoretically predicted, we could hypothetically still observe an excess of gravitational arcs without having the problem of too large Einstein radii.

Moreover, the correlation enables us to compute arc statistics for certain halo samples employing a new approach. The calculation of lensing cross sections for large halo samples is a computationally demanding problem since complete maps of deflection angles have to be computed for each individual lens. In comparison, the calculation of Einstein radii can be fast because only few deflection angles near critical curves need to be computed (cf. Sect. 5.5.1). Hence, it is beneficial to sample cosmological distributions of dark matter haloes, compute their Einstein radii, and finally infer their lensing cross sections by means of the correlation. We employ this new approach in Sect. 5.5.

5.3 IMPORTANCE OF CLUSTER MERGERS

Torri et al. (2004) numerically simulated cluster mergers and found that these events are capable of boosting the lensing cross sections for giant arcs by about one order of magnitude. In a subsequent work, Fedeli et al. (2006) showed that these events are not only important for the lensing cross sections of individual clusters, but also for the overall statistical strong-lensing efficiency of the cosmic cluster population.

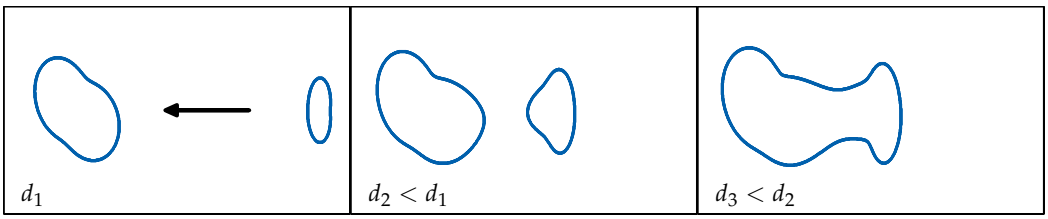

Figure 17: Evolution of the tangential critical curves during a merger of two massive triaxial dark matter haloes. Starting with an initial separation d_1 in the left panel, the distance between the two haloes is successively reduced ($d_1 > d_2 > d_3$).

To illustrate this important mechanism, let us briefly discuss the evolution of the tangential critical curves of two massive triaxial haloes during a merger by means of the following simplified toy model: Suppose that the main halo M_{main} rests at the coordinate origin, while the second halo M_{sub} is placed at an initial starting distance d_1 from the centre of the main halo. Since the precise properties (mass, axis ratios, orientation, etc.) of the two haloes do not matter for the following discussion, we simply state that their shape and orientation were chosen such that both lensing potentials were considerably elliptical. We simulated the merger by successively reducing the separation between the haloes and computed the resulting tangential critical curves at each step.

Figure 17 illustrates the evolution of the tangential critical curves for three intermediate steps of the simulated merger. The main halo rests at the coordinate centre on the left, and the subhalo approaches the main halo coming from the right. In the beginning (left panel), the separation between the haloes is large so that both have their own isolated and almost unperturbed tangential critical curves. As soon as the haloes approach, the shear in the region between them grows and stretches both tangential critical curves along the direction of motion (middle panel) until they finally merge to build one large, highly elongated structure (right panel). Given the tight correlation between Einstein radii and lensing cross sections, these configurations are also particularly efficient in producing thin arcs.

This description of the evolution of critical curves during cluster mergers was first given by Torri et al. (2004), and we refer the reader to their work for more details. It goes without saying that there are more sophisticated studies of cluster mergers that take virialization and other important physical processes properly into account. However, these models clearly go beyond the scope of our fast, semi-analytic approach to investigate the statistical strong-lensing properties of large cosmological populations of triaxial dark matter haloes.

In Redlich et al. (2012), we performed a detailed series of tests to investigate the evolution of strong-lensing properties during mergers of triaxial dark matter haloes. Our most important results can be summarized as follows: A notable enhancement of the strong-lensing efficiency can only be observed during major mergers (i. e. $M_{\text{sub}}/M_{\text{main}} \gg 0.05$). If the mass ratio $M_{\text{sub}}/M_{\text{main}}$ is too low, the elongation of the tangential critical curve enclosing the main halo is negligible. Conversely, the effect is particularly strong for mergers of clusters with comparable mass. Furthermore, the relative orientation of the merging haloes plays a dominant role. The most prominent

enhancement of the strong-lensing efficiency can be observed shortly before the two initially separated tangential critical curves merge to form one large, extremely elongated structure. This effect is especially pronounced when the direction of motion of the subhalo is aligned with the semi-major axis of the ellipsoidal surface mass density profile of the main halo, because then the elongation of the two separated tangential critical curves sets in relatively early and the diameter of the merged critical curve is particularly large. Finally, we could reproduce an increase of the lensing cross section by factors of ~ 2 for typical mass ratios $M_{\mathrm{sub}}/M_{\mathrm{main}} \sim 0.25$ if and only if the most favourable merger configuration (relative halo orientation) was chosen and the surface mass density profiles of both haloes were appreciably elliptical. In all other cases, the enhancement caused by mergers was notably smaller. Clearly, we could not reproduce the order-of-magnitude increase found by Torri et al. (2004). Precisely why this is the case is difficult to answer. Merging clusters in numerical simulations might be substantially more elongated than the semi-analytic triaxial lenses considered here. Furthermore, substructures – which our model neglects – might play an important role. It would certainly be interesting to investigate this discrepancy in future works.

5.4 SAMPLING COSMOLOGICAL POPULATIONS OF DARK MATTER HALOES

In the following sections and chapters, we need to be able to efficiently sample realistic catalogues of dark matter haloes, where realistic means that their mass and redshift distribution should come close to those of halo populations in numerical simulations and the observed Universe. To this end, we first describe a technique for sampling representative populations of individual haloes from a given mass function. After that, we introduce a new semi-analytic method for populating a fictitious observer's PNC with merging galaxy clusters.

5.4.1 *Isolated dark matter haloes*

To sample individual dark matter haloes from a given mass function, we adopt the following common MC approach (cf. Oguri & Blandford 2009). Suppose we intend to draw a random population of dark matter haloes within the mass range $[M_{\mathrm{min}}, M_{\mathrm{max}}]$ and the redshift interval $[z_{\mathrm{min}}, z_{\mathrm{max}}]$. To this end, we first subdivide the mass and redshift range into smaller, equidistant bins, adopting typical bin sizes of $\Delta(\log(M)) = 0.02$ and $\Delta z = 0.02$. Next, we calculate the mean expected number $\bar{N}$ of haloes in each bin using the theoretical mass function $\mathrm{d}n(M,z)/\mathrm{d}M$ (the Press & Schechter (1974) mass function, for instance),

$$\bar{N} = \frac{\mathrm{d}^2 N}{\mathrm{d}M\,\mathrm{d}z}\,\Delta M\,\Delta z = \frac{\mathrm{d}n(M,z)}{\mathrm{d}M}\,\Delta M \times \frac{\mathrm{d}V}{\mathrm{d}z}\,\Delta z\,, \tag{122}$$

where $\mathrm{d}V/\mathrm{d}z$ denotes the differential comoving volume. Finally, we generate a random integer number N from the Poisson distribution with mean $\bar{N}$, and sample N haloes whose masses and redshifts are uniformly distributed in the bin considered.

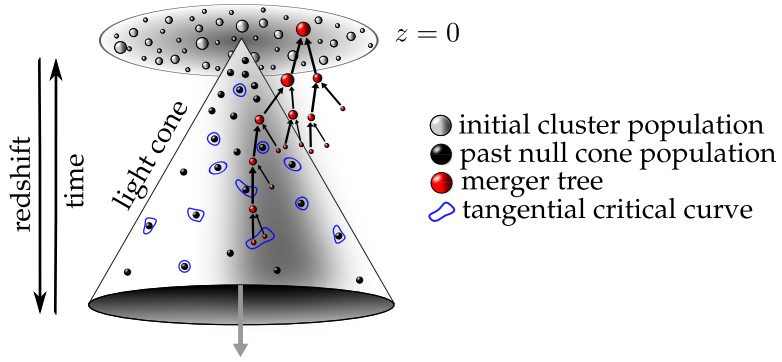

Figure 18: Sketch illustrating our new algorithm for projecting merging galaxy clusters onto the PNC of a fictitious observer.

This MC method is simple and efficient. It reliably generates random halo catalogues whose deviations from the theoretical mass function remain within the limits of Poisson noise.

5.4.2 *Merging dark matter haloes*

While large cosmological N-body simulations are probably the most realistic framework for studying the impact of mergers on the statistical lensing properties of selected cluster samples, they are computationally costly. As an alternative, we now introduce a fast, semi-analytic method that allows us to study the statistical impact of mergers within a fraction of the computing time required for N-body simulations. We follow this approach because we aim to be able to repeat our calculations for large cosmic volumes, varying a multitude of boundary conditions (i. e. different properties of the triaxial density profile, cosmological parameters, etc.), within a reasonably short computing time (cf. Chap. 8).

In this chapter, we require our new approach to be fully self-consistent within the framework of the extended Press-Schechter theory (Lacey & Cole 1993), which means that in particular the predicted merger rates and the Press & Schechter (1974) mass function must be reproduced accurately. This way, results based on our new method should agree reasonably well with those derived from numerical simulations; see the discussion at the end of this section for more details.

Suppose that we intend to analyse the strong-lensing properties of a representative all-sky realization of dark matter haloes in the mass and redshift range $[M_{\mathrm{min}}, M_{\mathrm{max}}]$ and $[z_{\mathrm{min}}, z_{\mathrm{max}}]$, respectively. To do this, we sequentially perform the following steps:

1. *Initial halo population*: We use a slight variation of the MC technique described in the previous section to populate the considered cosmic volume with an initial sample of dark matter haloes at the present time ($z = 0$). We subdivide the mass range into logarithmically equidistant bins of typical size $\Delta\left(\log(M)\right) = 0.02$

and calculate the mean expected number $\bar{N}$ of haloes in each bin using the Press-Schechter mass function $\mathrm{d}n(M, z=0)/\mathrm{d}M$,

$$\bar{N} = \frac{\mathrm{d}n(M, z=0)}{\mathrm{d}M} \Delta M \times V(z_{\mathrm{min}}, z_{\mathrm{max}}) \,. \tag{123}$$

Here, $V(z_{\mathrm{min}}, z_{\mathrm{max}})$ denotes the comoving volume of the spherical shell between the minimum and the maximum redshift (with respect to an observer at the coordinate origin). We then generate a random integer number N from the Poisson distribution with mean $\bar{N}$, and sample N haloes with logarithmically uniformly distributed masses in the corresponding bin. Since strongly lensing clusters are rare objects that are generally separated by large distances, we can neglect any kind of large-scale structure correlation and simply uniformly distribute these N sampled haloes in the considered cosmic volume. To this end, we assign each halo a random position on the sky, generate a uniformly distributed random number x in the range $[0, 1)$ and then compute the comoving distance r with respect to the observer, $r = \left[x r^3(z_{\mathrm{max}}) + (1-x) r^3(z_{\mathrm{min}})\right]^{1/3}$, where $r(z_{\mathrm{min}})$ and $r(z_{\mathrm{max}})$ denote the comoving distance to the minimum and maximum redshift, respectively. This formula takes the varying volume (as a function of radius) of spherical shells into account. Given the comoving radius r, we can readily infer each halo's redshift z_{obs} with respect to the observer.

2. *Reverse time evolution*: We evolve the initial halo population backwards in time. More precisely, we adopt the efficient MC approach proposed by Zhang et al. (2008, see "method B") to simulate a representative merger tree of each individual halo up to its previously determined observation redshift z_{obs}. Since Zhang et al. (2008) provide a nicely written step-by-step description of "method B", we refer the reader to their work for details. Generally, merger tree algorithms generate representative formation histories by evolving the initial halo mass backwards in time taking discrete time steps (typical step size $\Delta z \approx 0.02$). At the first time step, the halo is split into smaller progenitors by means of the conditional mass function (Lacey & Cole 1993). At the next time step, these new progenitors are again split into yet smaller progenitors using the same recipe, and so forth. Applying that scheme to all arising progenitors, this finally yields the full, tree-like formation history (i. e. the merger tree) of the initial halo. Given our predefined mass range, however, we discard all progenitors with masses below M_{min}. We note that we verified that our implementation accurately reproduces the Press-Schechter mass function as well as the theoretically predicted merger rates at any look-back time.

3. *Kinematics of merger trees*: To follow the trajectories of all arising progenitors in the considered cosmic volume, we additionally need to describe the kinematics of the merger trees. For that purpose, we adopt the following simplistic approach, which was first introduced by Fedeli & Bartelmann (2007). Each time a merger

between two haloes of masses M_1 and M_2 occurs, we estimate its duration using the dynamical time scale

$$T_{\mathrm{dyn}} = \sqrt{\frac{\left(r_{\mathrm{vir},1} + r_{\mathrm{vir},2}\right)^3}{G\left(M_1 + M_2\right)}}\,, \tag{124}$$

where $r_{\mathrm{vir},1}$ and $r_{\mathrm{vir},2}$ denote the virial radii of both haloes. These dynamical time scales are typically of the order of a several hundred Myr, which agrees well with merger durations measured in numerical simulations (see Torri et al. 2004, for instance). Assuming a uniform linear motion, we compute the relative velocity of the two haloes, $v_{\mathrm{rel}} = \left(r_{\mathrm{vir},1} + r_{\mathrm{vir},2}\right)/T_{\mathrm{dyn}}$, and finally sample a random direction of motion. We apply this scheme to all mergers. This way, we can easily compute the spatial positions of all progenitors of the considered merger tree at the observation redshift z_{obs}.

The above procedure is illustrated in Fig. 18: We first populate the considered cosmic volume with an initial halo sample at redshift $z = 0$, evolve that sample backwards in time using extended Press-Schechter merger trees combined with a simplistic model to describe the kinematics, and finally project the resulting halo configurations onto the PNC of a fictitious observer.

We would like to emphasise that our kinematic model of cluster mergers is clearly simplistic. For instance, we implicitly assumed central cluster collisions although the centres of merging clusters can typically be separated by up to several hundred kpc (see e.g. Sarazin 2002, for a semi-analytic approximation). Finite impact parameters may certainly influence the detailed evolution of the strong-lensing properties during individual cluster mergers, and it would be interesting to study refinements of our simplified model in future works.

Finally, we comment on the decision to base the above algorithm on the Press & Schechter (1974) mass function, although improved variants of the mass function with better accuracy have been proposed (cf. Jenkins et al. 2001; Sheth & Tormen 2002; Warren et al. 2006; Tinker et al. 2008). The Press-Schechter mass function is based on the theory of spherical collapse and only within this framework exact analytic expressions for the conditional mass function – which is the fundamental quantity for the computation of merger trees – can be derived. In contrast, most improved variants of the mass function are empirical fits to numerical simulations and hence there is no theoretical framework to derive the corresponding expressions for the conditional mass function. Since we aim to compare the statistics of Einstein radii of samples of isolated haloes to those of halo samples that incorporate cluster mergers using two completely independent methods (to cross-check our new merger algorithm) and in a fully self-consistent way, we are restricted to the mass functions based on the spherical collapse. The moderate deviations of the Press-Schechter mass function are negligible for our principal conclusions in this chapter. In contrast, if we were to perform a detailed comparison between our theoretical predictions and observations, the precise choice of the mass function would play an important role (cf. Sect. 6.3.1). We discuss an alternative merger algorithm for generating mass functions that agree well with those found in numerical simulations in Chap. 8.

5.5 IMPACT OF CLUSTER MERGERS ON THE STATISTICS OF THE LARGEST EINSTEIN RADII AND INFERRED OPTICAL DEPTHS

5.5.1 *Computation of Einstein radii*

In the previous section, we described two independent algorithms for populating the PNC of a fictitious observer with individual and merging dark matter haloes. Before presenting our final results, we now describe an efficient method for computing the distribution of Einstein radii.

Given a lens system, we first sort the masses of all haloes in descending order and begin with the computation of the Einstein radius of the most massive halo M_1. To this end, we scan the region around that halo for neighbouring subhaloes M_i whose distance d is shorter than the sum of both virial radii, $d \leq (r_{\mathrm{vir},1} + r_{\mathrm{vir},i})$. If any surrounding subhaloes satisfy this condition, they are taken into account for the computation of deflection angles. All other haloes that are farther away do not influence the strong-lensing properties of the considered massive halo M_1 and can safely be ignored.

Next, we assign a random triaxial density profile and a random orientation with respect to the observer to each relevant halo. This enables us to determine the tangential critical curve that encloses the massive halo M_1. To do this, we place halo M_1 at the coordinate centre of a Cartesian grid whose side length is chosen to be sufficiently long to contain all relevant subhaloes. Instead of computing the deflection angle map of the complete field and determining the tangential critical curve afterwards, we simply need to detect the first tangential critical point left of the coordinate origin and employ a standard friend-of-friend algorithm to identify the entire tangential critical curve. This way, we only have to compute deflection angles in small stripes surrounding the critical curve, which renders the algorithm very fast. If we aimed at computing the lensing cross section of the considered configuration, we would not be able to use this efficient method but instead would have to calculate the complete deflection angle map. This important difference illustrates why the determination of Einstein radii is computationally far less expensive and why it is of great advantage to infer lensing cross sections from Einstein radii using the discussed correlation between both quantities.

Finally, we detect all haloes which are enclosed by the computed tangential critical curve and mark them as haloes which do not have an independent Einstein radius. We repeat the above procedure for all remaining, unmarked haloes of the sorted mass list so that we end up with a complete catalogue of Einstein radii of the lens system considered.

5.5.2 *Statistics of the largest Einstein radii and inferred optical depths*

We can now quantify the statistical impact of cluster mergers on the strongest gravitational lenses ($\theta_{\mathrm{eff}} \geq 10''$). To this end, we generated a first sample of individual dark matter haloes and a second sample using our newly developed technique to incorporate cluster mergers. Since the largest observed Einstein radii, which may

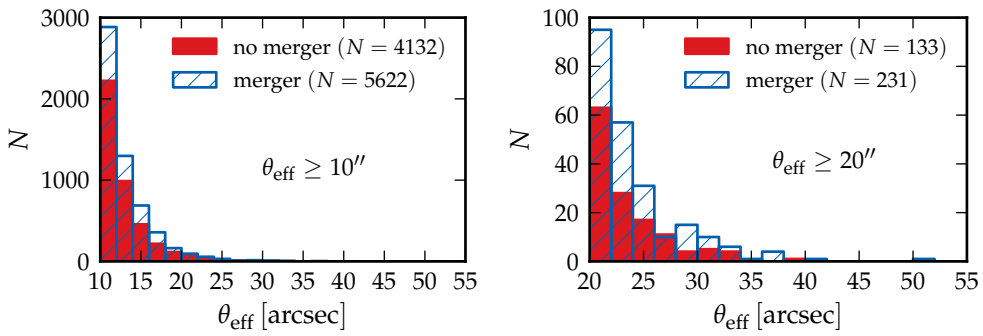

Figure 19: Comparison of the distributions of the largest Einstein radii including (blue patterned histogram) and excluding (red solid histogram) cluster mergers. The left (right) plot shows the histograms of all Einstein radii larger than $10''$ ($20''$).

challenge the standard cosmological model, were all found at redshifts well below unity (cf. Broadhurst & Barkana 2008; Zitrin et al. 2011), we focused our analysis on the redshift range $z \in [0, 1]$. In anticipation of the following results, we note that the masses of all single haloes with effective Einstein radii above $10''$ are larger than $10^{14}\, M_\odot/h$. Recalling that the mass ratio $M_{\rm sub}/M_{\rm main}$ of two merging clusters at least needs to exceed 5% to notably boost the strong-lensing efficiency of the main halo (cf. Sect. 5.3), we could therefore safely ignore all haloes with masses below $M_{\rm min} = 5 \times 10^{12}\, M_\odot/h$. In particular, we pruned all branches (i. e. progenitors) of the merger trees whose masses dropped below that threshold. We modelled all haloes by means of triaxial density profiles with an inner slope $\alpha = 1.0$ and assumed a source redshift of $z_{\rm s} = 2.0$.

Figure 19 and Table 3 (p. 81) clearly demonstrate that cluster mergers do have a significant impact on the distribution of the largest Einstein radii. While we find 4132 Einstein radii larger than $10''$ in the single halo run, that number increases by 36% up to 5622 haloes if mergers are taken into account. The effect is even more significant if we only consider the number of systems with Einstein radii above $20''$, in which case we find an increase of 74%.

Another interesting aspect to be analysed is the frequency of cluster mergers. To do this, we classified observed systems as being actively merging if more than one halo is enclosed by the tangential critical curve. Clearly, this definition does not cover those cases where merging clusters are already close to each other, but still have their own, highly elongated critical curves. Nevertheless, our choice should be sufficiently accurate for a qualitative estimate. We find that 35% of the systems with Einstein radii larger than $10''$ are actively merging. This number increases to 55% if we only consider those clusters with Einstein radii larger than $20''$. Given these results and the above number counts of Einstein radii, we can conclude that (1) cluster mergers are an important mechanism to increase the statistical lensing efficiency of cosmological halo populations and that (2) these events become increasingly dominant for particularly strong gravitational lenses.

Additional evidence in favour of these conclusions is provided by considering the very largest lenses in detail. In the simulation including mergers, eight out of

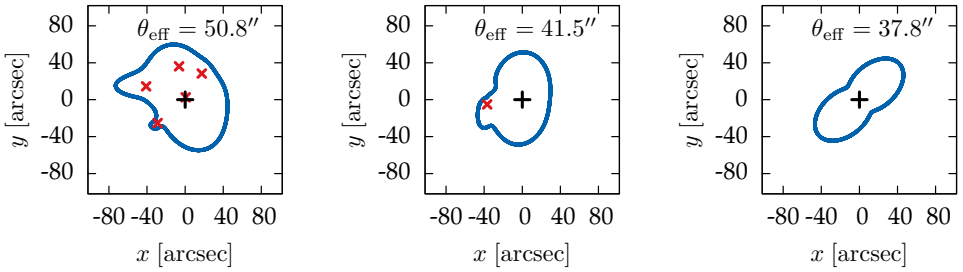

Figure 20: Tangential critical curves of the systems with the largest (left diagram), second largest (middle diagram), and third largest (right diagram) Einstein radius in our simulation including cluster mergers. The black cross in the centre indicates the position of the main halo. The red crosses mark the positions of all subhaloes that are enclosed in the tangential critical curve.

the ten largest Einstein radii stem from actively merging systems. Moreover, the largest Einstein radius in the single halo run has the size $\theta_{\rm eff} = 38.5''$, while we find a notably larger maximum of $\theta_{\rm eff} = 50.8''$ in the run with mergers. Needless to say, these maxima are subject to statistical fluctuations. Since the considered halo populations were randomly drawn, it may well be that for other realizations the single halo maximum is larger than the one found with merging haloes. However, we can safely conclude that cluster mergers need to be taken into account in semi-analytic, statistical studies that aim to challenge the standard cosmological model on the basis of the largest observed Einstein radii.

The left panel of Fig. 20 shows the critical curve of the largest observed Einstein radius, which belongs to an extraordinary system at redshift $z = 0.43$. Starting with an initial mass of $M = 1.8 \times 10^{15}\, M_\odot/h$ at redshift $z = 0$, the halo was split into 20 progenitors with masses above the minimum mass threshold $M_{\rm min}$ before it finally reached the observer's PNC. Six of these 20 progenitors are enclosed in the critical curve shown. The most massive halo in the centre has a mass of $M = 1.1 \times 10^{15}\, M_\odot/h$. The masses of the five surrounding subhaloes lie in the range $6.7 \times 10^{12} - 1.5 \times 10^{14}\, M_\odot/h$. To further demonstrate the importance of mergers, we removed these subhaloes and computed the Einstein radius of the main halo alone, finding that it drops by $\sim 20''$ to now only $\theta_{\rm eff} = 30.9''$. Moreover, we can use that system to verify our choice of the minimum mass threshold $M_{\rm min} = 5.0 \times 10^{12}\, M_\odot/h$. The smallest enclosed subhalo has a mass of $M = 6.7 \times 10^{12}\, M_\odot/h$, which is close to $M_{\rm min}$. If we ignore that halo for the computation of the tangential critical curve, the Einstein radius drops only slightly by $\sim 1.4\%$ to $\theta_{\rm eff} = 50.1''$, confirming that our mass cut-off only leads to negligible errors. There are mainly two reasons for introducing such a mass cut-off in general: (1) we can discard a considerable amount of small-mass branches of the merger trees and (2) we can limit the number of (irrelevant) subhaloes that need to be taken into account for the computation of the critical curves. Both aspects substantially improve the performance of our algorithm.

The framework of hierarchical structure formation suggests that relatively young clusters at intermediate and high redshifts ($z \gtrsim 0.5$) are dynamically more active than older systems at low redshifts. Therefore, it is to be expected that mergers

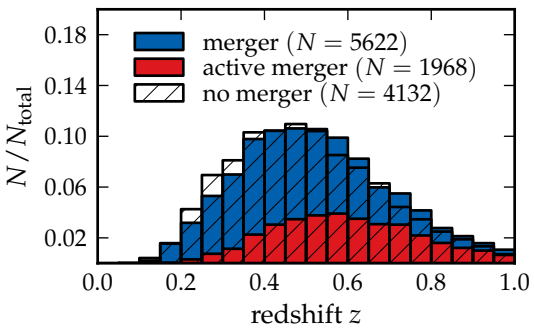

Figure 21: (Normalized) redshift distribution of the strong lenses with Einstein radii larger than 10″ including (blue solid histogram) and excluding (black patterned histogram) cluster mergers. In addition, the red stacks indicate the fraction of actively merging systems of all strong lenses represented by the blue solid histogram, i. e. including cluster mergers.

mainly increase the number of strong lenses in the upper redshift range of our simulation volume. Although Fig. 21 confirms this expectation, the net shift of the overall population of strong-lensing clusters to higher redshifts due to mergers is only moderate. Instead, the redshift distribution of the strongest lenses is predominantly determined by the chosen lensing geometry with sources at redshift $z_{\mathrm{s}} = 2.0$.

Finally, we used the correlation between Einstein radii and lensing cross sections to infer the impact of cluster mergers on the statistics of giant gravitational arcs from the distributions of Einstein radii just computed. Since we concentrated on the strongest gravitational lenses only, we are well inside the regime where the correlation between both quantities is particularly tight and hence our following estimate should be reasonably accurate (Redlich et al. 2012). First, we randomly picked ~ 400 haloes of our catalogue with Einstein radii above 10″ and computed their lensing cross sections $\sigma_{7.5}$. We then used these results to calibrate the best linear fit relation for the correlation:

$$\log(\sigma_{7.5}) = (2.12 \pm 0.06) \log(\theta_{\mathrm{eff}}) - (5.24 \pm 0.07) \; . \tag{125}$$

The cumulative lensing efficiency of cluster samples is usually characterized by their *optical depth* τ for giant gravitational arcs, which is given by the sum of the individual lensing cross sections $\sigma_{7.5,i}$ divided by the size of the entire source sphere,

$$\tau \equiv \left(\sum_i \sigma_{7.5,i} \right) \times \left(4\pi D_s^2 \right)^{-1} \; , \tag{126}$$

where D_s denotes the angular-diameter distance to the source plane. Assuming that the individual lensing cross sections do not overlap in the source plane, the optical depth corresponds to the probability that an arbitrarily placed source with the specified characteristics (cf. Redlich et al. 2012, Sect. 3.1) produces a gravitational arc with a length-to-width ratio higher than 7.5.

As summarised in Table 3, cluster mergers increase the optical depth of all haloes with Einstein radii above 10″ by approximately 45%. Furthermore, as was to be expected, the impact on those systems with Einstein radii above 20″ is even stronger: We find that mergers statistically increase the number of giant arcs produced by these particularly strong lenses by approximately 85%.

Table 3: Comparison of the strong-lensing statistics of two representative samples of dark matter haloes $\left(M > 5 \times 10^{12}\, M_\odot/h,\, z \in [0,1]\right)$ including and excluding cluster mergers. We show the maximum effective Einstein radius $\max(\theta_{\rm eff})$, the number of Einstein radii above a certain threshold X, $N\,(\theta_{\rm eff} \geq X)$, and the optical depth $\tau(\theta_{\rm eff} > X)$ (for gravitational arcs) of all haloes with Einstein radii above the threshold X.

	single haloes	merging haloes
$\max(\theta_{\rm eff})$	$38.5''$	$50.8''$
$N\,(\theta_{\rm eff} \geq 10'')$	4132	5622 $(+36\%)$
$N\,(\theta_{\rm eff} \geq 20'')$	133	231 $(+74\%)$
$\tau(\theta_{\rm eff} > 10'')$	2.9×10^{-7}	4.2×10^{-7} $(+45\%)$
$\tau(\theta_{\rm eff} > 20'')$	3.3×10^{-8}	6.1×10^{-8} $(+85\%)$

5.6 CONCLUSIONS

In this chapter, we mainly focused on developing the theoretical tools needed for the applications in the remainder of this work. We introduced the semi-analytic model of triaxial gravitational lenses and discussed the tight correlation between lensing cross sections and Einstein radii. This correlation is important for our approach in the following three chapters where we discuss the extreme value and order statistics of the largest Einstein radii, finding that there is no statistical evidence for claiming that the largest observed Einstein radii are in tension with the standard cosmological model. Given the tight correlation between lensing cross sections and Einstein radii, this result also implies that the abundance of giant gravitational arcs in the *strongest observed lenses* – which are the focus of this part of the thesis – should agree well with the theoretical expectations. However, it is important to bear in mind that this does not necessarily solve the general arc statistics problem (cf. Sect. 5.2.3).

We highlighted the importance of cluster mergers for the strong-lensing efficiency of individual clusters and thereupon developed a new semi-analytic algorithm for projecting merging galaxy clusters onto the PNC of a fictitious observer. Using this new technique, we were able to compare the statistical strong-lensing properties of one sample of single (isolated) dark matter haloes and a second sample of dark matter haloes that includes the effect of cluster mergers.

Studying representative all-sky realizations of clusters at redshifts $z < 1$ and assuming a constant source redshift of $z_{\rm s} = 2$, we found that cluster mergers increase the theoretically expected number of Einstein radii above $10''$ ($20''$) by approximately 36% (74%), indicating that these events provide a highly efficient mechanism to enhance the lensing efficiency of particularly strong gravitational lenses. These results clearly show that semi-analytic studies need to take cluster mergers into account if they aim to question the standard cosmological model by comparing the largest observed Einstein radii to theoretical expectations.

Furthermore, we estimated that the optical depth for giant gravitational arcs of those haloes with Einstein radii above $10''$ ($20''$) increases by approximately 45% (85%),

which also highlights the importance of cluster mergers for the statistics of giant gravitational arcs. Still, we were unable to reproduce the doubling of the optical depth found by Fedeli et al. (2006). However, this discrepancy can be attributed to the following important differences between both studies:

- Instead of adopting triaxial density profiles with varying properties (i. e. concentration and axis ratios), Fedeli et al. (2006) modelled clusters as spherically symmetric density profiles and elliptically distorted their lensing potentials by a constant amount. Moreover, these authors used an alternative concentration-mass relation. Consequently, their lens model produces surface mass densities with different properties, which are decisive for the strength of the boost of the strong-lensing efficiency during cluster mergers (Redlich et al. 2012).

- Analyses of cluster mergers in numerical simulations reveal that (1) the major axes of infalling substructures are intrinsically aligned with the major axis of the main halo due to its tidal field and (2) subhaloes preferentially approach the main halo along its major axis (Lee et al. 2005; Altay et al. 2006; Zhang et al. 2009). Motivated by these findings, Fedeli et al. (2006) throughout modelled mergers by perfectly aligning the major axes of both haloes and assuming that the subhalo always approaches the main halo exactly along its major axis. As shown in Redlich et al. (2012), these orientations are most favourable and produce the strongest possible enhancement of the strong-lensing efficiency during cluster mergers. On the other hand, this assumption clearly is an idealization that might lead to an overestimation of the net effect of mergers. Since there is no reliable theoretical framework that allows us to predict those alignments realistically, we chose the fairly conservative approach to sample the relative orientations of merging haloes randomly, without taking their possible axis correlations and preferred directions of motion into account. Hence, we expect that our results slightly underestimate the net effect of mergers.

- While we only computed the optical depth of particularly strong lenses with Einstein radii above $10''$, Fedeli et al. (2006) determined the optical depth of all clusters at redshifts $z > 0.5$. Hence, their computation additionally incorporates the following important effect: Cluster mergers tend not only to increase the lensing cross section of the strongest gravitational lenses, but are also capable of transforming clusters to strong gravitational lenses that would otherwise be subcritical. More precisely, it may well be that two relatively small clusters with vanishing individual lensing cross sections produce a nonvanishing, joint lensing cross section while merging. Consequently, mergers are an effective mechanism to substantially increase the optical depth of clusters in the lower mass range. Given the steepness of the mass function, these objects dominate the total optical depth and thus their contribution is likely significant for the doubling of the optical depth found by Fedeli et al. (2006).

Given these remarks, we conclude that our findings do not disagree substantially with the previous results of Fedeli et al. (2006).

6

IS THE LARGE EINSTEIN RADIUS OF MACS J0717.5+3745 IN CONFLICT WITH ΛCDM?

ABSTRACT

Does the largest observed Einstein radius exceed the maximum theoretical expectations of the standard cosmological model? We show that the theory of extreme value statistics provides the proper mathematical framework for studying such questions and describe a semi-analytic method for calculating the general extreme value (GEV) distribution of the largest Einstein radius in a given cosmological volume. We find that the GEV distribution is very sensitive to several theoretical model assumptions, such as the precise choice of the halo mass function, lens triaxiality, the inner slope of the halo density profile, and the mass-concentration relation. We study the occurrence probability of the largest known Einstein radius, which was observed in the galaxy cluster MACS J0717.5+3745, finding that this system is not in conflict with the ΛCDM model. A much larger Einstein radius ($\gtrsim 100''$) would have to be observed to claim tension between theory and observations.

The contents of this chapter were published in Waizmann et al. (2012b). In comparison to the published article, we shortened and rewrote several sections.

6.1 INTRODUCTION

Galaxy clusters are extreme objects: They are amongst the most massive collapsed structures in the observable Universe and flag the rarest peaks of the initial density field. The gas contained in their gravitational potential wells is heated up to extremely high temperatures of $\sim 10^7 - 10^8\,\mathrm{K}$, resulting in the emission of X-ray radiation. Furthermore, they can act as strong gravitational lenses, causing spectacular image distortions of background sources. Individually and as a population, galaxy clusters contain rich information on the formation of structure in the Universe.

Recently, the interest in the extremest among the extreme, the most massive clusters, has substantially increased. This development was mainly triggered by the detection of very massive galaxy clusters at high redshifts (Mullis et al. 2005; Rosati et al. 2009; Jee et al. 2009; Marriage et al. 2011; Menanteau et al. 2012; Foley et al. 2011; Williamson et al. 2011). Several works studied the probability to find such objects in a standard ΛCDM cosmology (Holz & Perlmutter 2012; Baldi & Pettorino 2011; Cayón et al. 2011; Hotchkiss 2011; Mortonson et al. 2011; Chongchitnan & Silk 2012; Waizmann et al.

2012a). All these studies focused on the mass of galaxy clusters, which is unfortunately not a direct observable. Moreover, the mass of a galaxy cluster, ill defined in the first place, is subject to substantial scatter and biases. Hence, it is desirable to study extremes in direct, better defined observables, such as strong lensing signals.

A particularly interesting case from this point of view is the extremely large critical curve of the X-ray luminous galaxy cluster MACS J0717.5+3745 located at redshift $z = 0.546$, which has been independently detected by the Massive Cluster Survey (MACS) (Ebeling et al. 2001, 2007) and as a host of a diffuse radio source (Edge et al. 2003). A strong-lensing analysis revealed that the effective Einstein radius, with $\theta_{\rm eff} = (55 \pm 3)''$ for an estimated source redshift of $z \simeq 2.5$, is the largest known at redshifts $z > 0.5$ (Zitrin et al. 2009, 2011). It is unclear whether or not such a large Einstein radius is consistent with the ΛCDM cosmology (Zitrin et al. 2009).

In this chapter, we aim to answer precisely this question, that is, we aim to investigate whether or not the largest observed Einstein radius is consistent with the theoretical predictions of the standard cosmological model. To this end, we proceed as follows: In Sect. 6.2, we concisely introduce the basic elements of extreme value statistics that are relevant for the remainder of this work. We then describe a semi-analytic method for studying the statistical distribution of the largest Einstein radius in a given cosmological volume and show that the distribution converges to the general extreme value distribution. In Sect. 6.3, we discuss several theoretical model assumptions that strongly affect the distribution of the largest Einstein radius. In Sect. 6.4, we assess the occurrence probability of the large Einstein radius of MACS J0717.5+3745 within the framework of extreme value statistics. Finally, in Sect. 6.5, we present our conclusions.

For reasons to be clarified later (cf. Chap. 8), we neglect the impact of cluster mergers in the present and also in the following chapter. Because cluster mergers significantly shift the distribution of Einstein radii to larger values, all estimates presented in the following two chapters should be considered conservative.

Throughout this chapter, we adopt the best-fitting cosmological parameters obtained from the Wilkinson Microwave Anisotropy Probe seven-year data (WMAP7; Larson et al. 2011), $(\Omega_{\Lambda 0}, \Omega_{\rm m0}, \Omega_{\rm b0}, h, \sigma_8) = (0.727, 0.273, 0.0455, 0.704, 0.811)$.

6.2 APPLYING EXTREME VALUE STATISTICS TO THE DISTRIBUTION OF THE LARGEST EINSTEIN RADIUS

The theory of extreme value statistics models the stochastic behaviour of extremes and provides a rigorous framework for determining the likelihood of rare events (see e.g. Gumbel 1958; Kotz & Nadarajah 2000; Coles 2001; Reiss & Thomas 2007, for comprehensive introductions). In particular, the theory defines the mathematical recipe for quantitatively answering questions of the following kind: Given a cosmological model, how likely is it that the largest observed Einstein radius in a survey of a certain cosmological volume is as large as X''?

In the framework of extreme value statistics, there are two approaches to the modelling of rare events. The first one, also known as the Gnedenko approach (Fisher & Tippett 1928; Gnedenko 1943), models the distribution of block maxima, while the second one, known as the Pareto approach (Pickands 1975), models the distribution

of excesses over high thresholds. Because we are interested in the distribution of the largest Einstein radius and do not intend to calculate the likelihood for large Einstein radii to exceed a predefined threshold, we discuss the first approach in the following.

6.2.1 *Gnedenko approach*

Given a set of independent identically distributed (i.i.d.) random variables X_i, the block maximum M_n is defined as

$$M_n = \max(X_1, \dots X_n) \; . \tag{127}$$

Under very general conditions, the limiting cumulative distribution function (CDF) of the renormalised block maxima for $n \to \infty$ is given by one of the extreme value families: Gumbel (Type I), Fréchet (Type II), or Weibull (Type III) (Fisher & Tippett 1928; Gnedenko 1943). These three families can be unified as a general extreme value (GEV) distribution (von Mises 1954; Jenkinson 1955),

$$G_{\gamma,\beta,\alpha}(x) = \begin{cases} \exp\left\{-\left[1+\gamma\left(\frac{x-\alpha}{\beta}\right)\right]^{-1/\gamma}\right\}, & \text{for} \quad \gamma \neq 0, \\ \exp\left\{-\mathrm{e}^{-\left(\frac{x-\alpha}{\beta}\right)}\right\}, & \text{for} \quad \gamma = 0, \end{cases} \tag{128}$$

with the location, scale, and shape parameters α, β, and γ. In this generalisation, $\gamma = 0$ corresponds to the Type I, $\gamma > 0$ to the Type II, and $\gamma < 0$ to the Type III distributions. The corresponding probability density function (PDF) is given by $g_{\gamma,\beta,\alpha}(x) = \mathrm{d}G_{\gamma,\beta,\alpha}(x)/\mathrm{d}x$ and reads (for $\gamma \neq 0$)

$$g_{\gamma,\beta,\alpha}(x) = \frac{1}{\beta}\left[1+\gamma\left(\frac{x-\alpha}{\beta}\right)\right]^{-1-1/\gamma} \exp\left\{-\left[1+\gamma\left(\frac{x-\alpha}{\beta}\right)\right]^{-1/\gamma}\right\} . \tag{129}$$

The mode of the GEV distribution – which is the most likely value – is given by

$$x_0 = \alpha + \frac{\beta}{\gamma}\left[(1+\gamma)^{-\gamma} - 1\right] \; . \tag{130}$$

The expected value of the GEV distribution is

$$\mathrm{E}_{\mathrm{GEV}} = \alpha - \frac{\beta}{\gamma} + \frac{\beta}{\gamma}\,\Gamma\left(1-\gamma\right) \; , \tag{131}$$

where Γ denotes the Gamma function.

6.2.2 *Modelling the distribution of the largest Einstein radius with the GEV*

Due to the complexity of the modelling of the Einstein radius distribution, it is not possible to find analytic relations for the GEV parameters, as can be done for halo masses, for instance (Davis et al. 2011; Waizmann et al. 2011). Therefore, we adopt the following semi-analytic approach: Suppose we intend to calculate the GEV

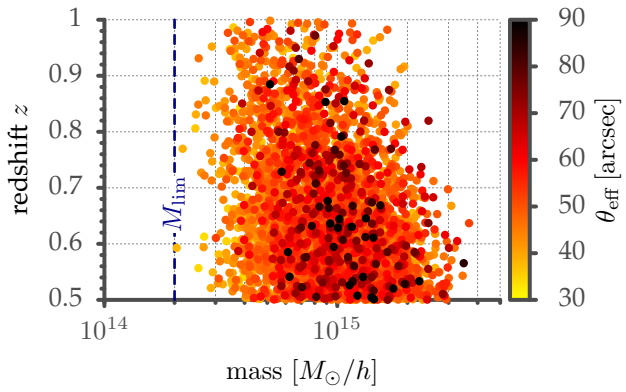

Figure 22: Distribution in mass and redshift of 4 000 maxima of the Einstein radius in the redshift interval $0.5 \leq z \leq 1.0$, assuming full sky coverage. The colour encodes the size of the individual largest Einstein radius from each simulation run.

distribution of the largest Einstein radius in a certain cosmological volume. We then use the MC technique described in Sect. 5.4.1 to populate the volume with a mock catalogue of triaxial gravitational lenses, and compute their Einstein radii. We note the largest Einstein radius $\theta^1_{\rm eff}$ of the current realisation, and repeat this random process n times. After this procedure, we have a set of n largest Einstein radii extracted from an ensemble of n representative realisations of surveys of the considered cosmological volume, $M = \left(\theta^1_{\rm eff}, ..., \theta^n_{\rm eff}\right)$. For large n, the empirical CDF of these maxima converges to the GEV distribution. Vice versa, for sufficiently large n, we can fit the GEV distribution to the empirically sampled CDF. This fit allows us to derive analytic relations for probabilities and exclusion criteria, and also enables us to smoothly extrapolate to regions that are only sparsely sampled by the empiric data.

To optimise our semi-analytic approach for the following applications, we need to discuss some preliminary issues. For instance, the choice of the redshift interval and the allowed halo mass range is decisive to keep computational costs under control. Moreover, we have to determine how many mock realisations we need to sample to yield accurate estimates of the location, shape and scale parameter of the GEV distribution.

To investigate these questions, we focus our study of the distribution of the largest Einstein radii on clusters in the redshift range $0.5 \leq z \leq 1$, assuming a source redshift of $z_{\rm s} = 2.0$. This choice already drastically reduces the number of haloes that have to be simulated, and was motivated by the fact that the 12 MACS clusters analysed by Zitrin et al. (2011) were observed at redshifts $z > 0.5$. Next, we need to identify a lower mass limit $M_{\rm lim}$ for the MC algorithm that draws random halo populations, which must be chosen such that the inferred sampled maxima distribution is not biased. To do so, we simulated 4 000 mock realisations of the considered cosmological volume, based on the Tinker et al. (2008) mass function, and adopting a lower mass limit of $M > 2 \times 10^{14}\, M_\odot/h$. Figure 22 shows the mass and redshift distribution of the 4 000 largest Einstein radii, confirming that the chosen mass limit is sufficiently low; this is in good agreement with the results of Oguri & Blandford (2009). Unless stated otherwise, we adopt $M_{\rm lim} = 2 \times 10^{14}\, M_\odot/h$ throughout this chapter.

We note that Fig. 22 also shows that the maxima stem from a wide range of masses. It is not unlikely that a rather low-mass cluster exhibits the largest Einstein radius. Because we are modelling triaxial haloes, this result is a first indication that several other properties of the strongest lenses – such as the orientation of the halo with

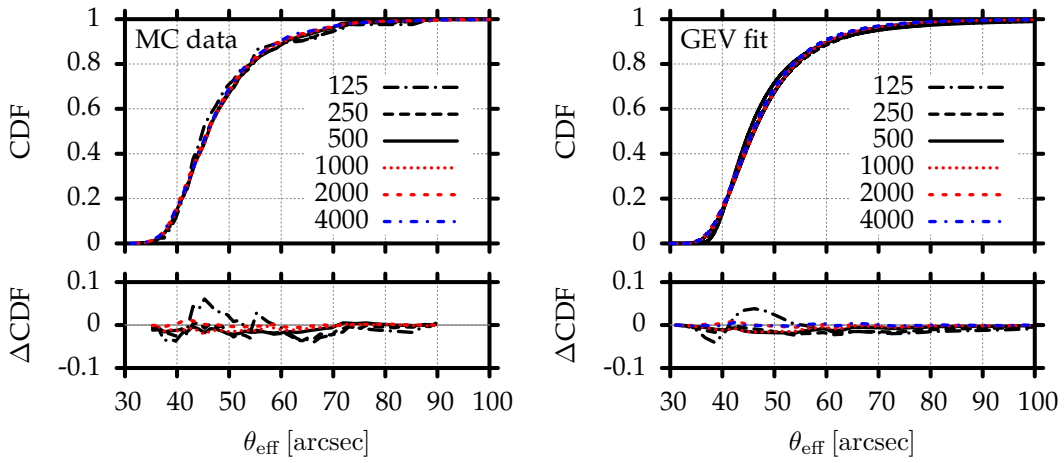

Figure 23: CDFs of the largest Einstein radius for a different number of maxima in the range between 125 and 4 000. The left panel shows the CDFs directly based on the MC simulations, and the right panel presents the corresponding fits of the GEV distribution. The small lower panels show the difference ΔCDF with respect to the high-resolution run based on 4 000 maxima.

respect to the observer, the lensing geometry, and the concentration – are more important than the mass. Finally, most of the maxima are found in the lower redshift range; this is a consequence of the chosen lensing geometry ($z_{\rm s} = 2.0$).

Having fixed the mass and redshift range, the last step in optimizing the computational cost is to understand how many independent maxima actually have to be sampled in order to construct the CDF of the largest Einstein radius. To this end, we computed the respective CDFs for different sample sizes $N_{\rm samp}$ between 125 and 4 000. Each CDF was computed at 50 linearly equidistant points between the largest and the smallest value. The results of these computations are presented in the left panel of Fig. 23. As expected, the noise of the CDFs decreases with increasing $N_{\rm samp}$. For $N_{\rm samp} \geq 1\,000$, the difference with respect to the high resolution run with $N_{\rm samp} = 4\,000$ is $\lesssim 0.02$, corresponding to an over-estimation of the occurrence probability of a given Einstein radius by less than two per cent. Hence, we utilise $N_{\rm samp} = 1\,000$ for all computations in the remainder of this chapter, unless stated otherwise.

The right panel of Fig. 23 indicates that the GEV distribution fits the MC-simulated distributions very well. In Table 4 (p. 88), we additionally present the fitted GEV parameters as well as the root mean square of the residuals for the individual runs. Anticipating the results of the following sections, we note that the fitted shape parameters γ for most distributions discussed in this chapter are found to be in the range of $0.05 < \gamma < 0.2$, which means that the distribution of the largest Einstein radius can in general be described by a Fréchet (Type II) distribution and is consequently bounded from below. The location parameter α is always very close to the mode, the most likely maximum, with the two values differing only by $\sim$ one per cent. It is noteworthy that the location parameter α can be estimated very well with rather small sample sizes, whereas the shape parameter γ is subject to larger uncertainties. Even

Table 4: Values of the location, scale, and shape parameters, α, β, and γ of the GEV distributions fitted (at 50 equally linearly space points; see text) to the CDFs of the largest Einstein radius for different sample sizes $N_{\rm samp}$. We additionally quote the number of degrees of freedom (DoF) of the fit and the root mean square (rms) of the residuals.

$N_{\rm samp}$	α [arcsec]	β [arcsec]	γ	DoF	rms
125	43.17 ± 0.066	5.12 ± 0.101	0.35 ± 0.020	47	1.234×10^{-2}
250	43.69 ± 0.050	6.04 ± 0.077	0.23 ± 0.014	47	8.665×10^{-3}
500	43.81 ± 0.044	6.19 ± 0.067	0.15 ± 0.012	41	6.394×10^{-3}
1000	43.83 ± 0.026	6.16 ± 0.039	0.14 ± 0.007	41	3.736×10^{-3}
2000	43.52 ± 0.017	6.14 ± 0.026	0.13 ± 0.005	41	2.442×10^{-3}
4000	43.58 ± 0.015	6.07 ± 0.023	0.13 ± 0.004	34	2.036×10^{-3}

for only 125 samples, the difference of the mode with respect to the $N_{\rm samp} = 4\,000$ case is less than two arcsec. This result is similar to the findings of Waizmann et al. (2011), who reported the same behaviour for the case of halo masses.

In what follows, we use the GEV fits for any subsequent analysis like the calculation of CDFs, PDFs, modes or quantiles.

6.3 DISTRIBUTION OF THE LARGEST EINSTEIN RADIUS

6.3.1 *Impact of the mass function*

The choice of the mass function must have an impact on the distribution of the largest Einstein radius because it alters the size of the halo population from which the maxima are drawn. This effect is particularly important for galaxy clusters since the exponentially suppressed tail of the mass function is naturally very sensitive to modification. As previously shown in Fig. 22, the maxima stem from a relatively broad range of masses. Hence, the larger the halo population in this mass range, the more likely it is to sample a particularly large Einstein radius.

To quantify the influence of different mass functions, we sampled the CDFs of the largest Einstein radii for four different mass functions, namely the Press & Schechter (1974) (PS), Tinker et al. (2008) (Tinker), Sheth & Tormen (1999) (ST), and the Crocce et al. (2010) (Crocce) mass functions. The differences between these mass functions are visualised in

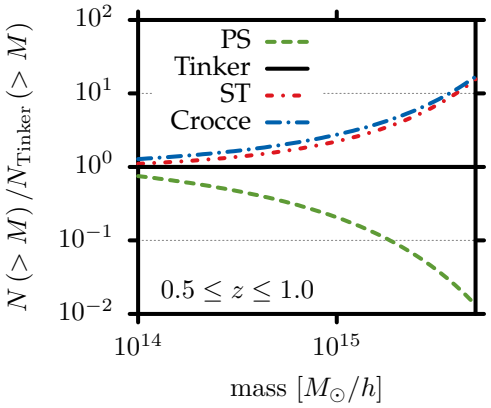

Figure 24: Number of massive haloes predicted by different mass functions with respect to the Tinker mass function.

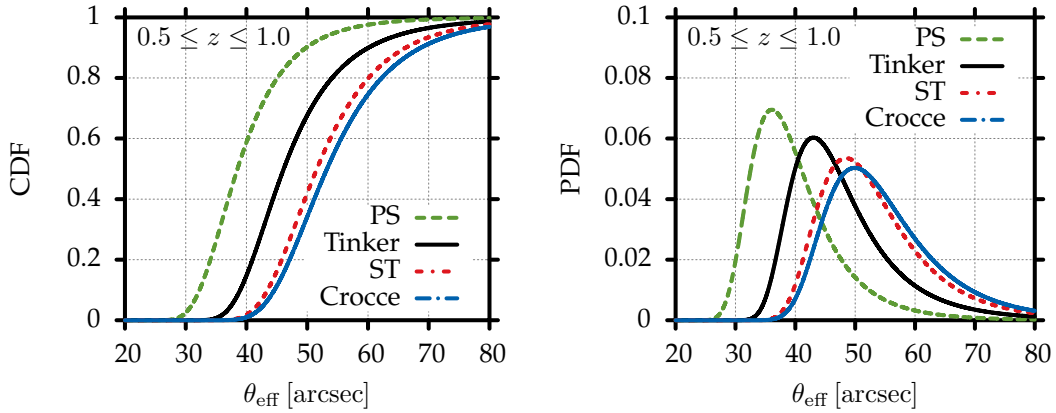

Figure 25: CDFs and PDFs of the largest Einstein radius for different mass functions.

Fig. 24. We decided to use the Tinker mass function as a reference because the halo masses are defined as spherical overdensities with respect to the mean background density, a definition that is closer to theory and actual observations than the friend-of-friend masses that were used for the Crocce mass function. We added the Crocce mass function to our analysis because it predicts substantially more haloes at the high-mass end (Bhattacharya et al. 2011). It is based on simulations with a box size much larger than the horizon scale, which gives more statistics at the high-mass end at the price of leaving the realm of the Newtonian approximation. However, Green & Wald (2012) argue that the Newtonian approximation for N-body simulations might also be valid on super-horizon scales.

The resulting extreme value distributions for the four different mass functions are presented in Fig. 25, based on the simulation of 1 000 maxima in the redshift range $0.5 \leq z \leq 1.0$ on the full sky. The results clearly show that the effect of different mass functions is substantial. The CDFs based on the ST and the Crocce mass functions exhibit the strongest difference with respect to the PS one. The modes of the distributions are 36.1″ (PS), 43.0″ (Tinker), 48.4″ (ST), and 49.9″ (Crocce), that is, they can differ by more than ten arcsec, which implies that the inferred occurrence probability for a given Einstein radius is highly sensitive to the precise choice of the mass function. For completeness, we note that Fig. 25 and the numerical values of the shape parameters γ indicate that the shape of the best-fitting GEV distributions is almost constant. We thus conclude that a change of the mass function primarily causes a shift and a broadening of the distributions along the θ_{eff}-direction.

6.3.2 *Impact of lens triaxiality*

The triaxiality of gravitational lenses has an important impact on the distribution of the maxima. For instance, a highly elongated halo whose major axis is aligned along the line-of-sight of the observer exhibits a highly concentrated, projected surface mass density profile, which gives rise to a large tangential critical curve (see e.g. Oguri et al. 2003; Dalal et al. 2004; Meneghetti et al. 2007, 2010). Therefore, when sampling axis ratios a/c and b/c from the distributions (109) and (110), particularly small axis ratios

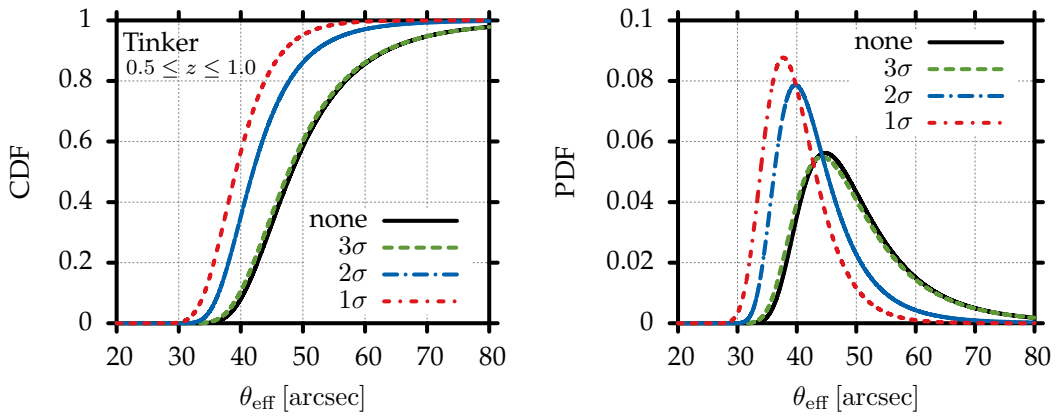

Figure 26: CDFs and PDFs of the largest Einstein radius for different cut-offs of the axis-ratio distribution as labelled in the figure.

can potentially propagate into extreme strong-lensing events. Since the empirical fits from JS02 were only based on few data points in this regime, it is unclear how reliable the fitted axis-ratio distributions are.

To study the impact of this uncertainty, we introduced a cut-off in the distribution (109) for the scaled axis ratio $a_{\rm sc}$ to remove extreme cases. More precisely, we cut off the distribution at different confidence levels n, according to

$$a_{\rm sc}^{\rm cut} = 0.54 - n\sigma_{\rm s} \,, \tag{132}$$

selecting values of 1σ, 2σ, 3σ and comparing them to the case without any cut-off. We simulated the distributions of the largest Einstein radius for the different cut-offs based on 1 000 maxima, assuming a lower mass limit of $M_{\rm lim} = 2 \times 10^{14}\, M_\odot/h$ and the Tinker mass function.

Table 5: Shape parameter γ and the mode of the CDFs for different cut-offs in the axis-ratio distribution.

cut	$a_{\rm sc}^{\rm cut}$	γ	Mode
1σ	0.427	−0.014	$37.7''$
2σ	0.314	0.098	$39.8''$
3σ	0.201	0.149	$44.2''$
none	–	0.151	$44.8''$

Table 5 and Fig. 26 show that the effect of the above cut-off is indeed substantial. In comparison to the previous section, the cut-off value not only strongly affects the mode but also the shape of the CDFs. For the 1σ cut-off, the shape parameter becomes negative. Consequently, the CDF of the largest Einstein radius is then described by a Weibull (Type III) distribution, indicating that the underlying distribution is bounded from above. For decreasing values of n, that is, by enforcing less extreme axis ratios, the CDF steepens, indicating that large Einstein radii become less likely.

Motivated by these results, we investigated whether or not the largest Einstein radii are always produced by highly elongated haloes with extreme axis ratios. To this end, we studied the distribution of random halo samples in scaled axis ratio $a_{\rm sc}$ and concentration $c_{\rm e}$. The left panel of Fig. 27 compares the distribution of the *full* halo sample of a *single* realisation with the distribution of the $a_{\rm sc}$ *minima* based on 1 000 all-sky realisations. As expected (cf. Sect. 5.2.1), highly elongated haloes exhibit low values of the concentration parameter. Typical values for the minima scatter around

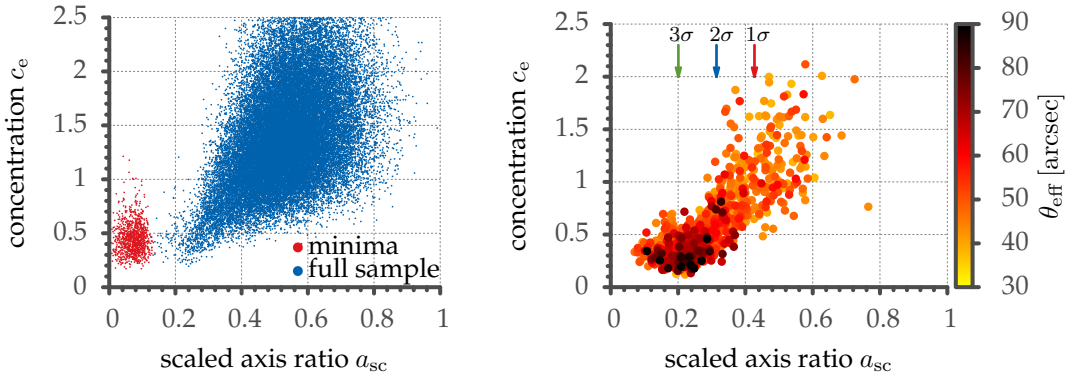

Figure 27: Distribution in scaled axis ratio a_{sc} and concentration c_e of sampled haloes, according to different selection criteria. The left panel shows the distribution of a full halo sample of a single realisation (blue dots) and the sample of the a_{sc} minima (red dots) extracted from 1 000 independent halo samples. The right panel shows the corresponding distribution of the haloes that give rise to the 1 000 largest Einstein radii. The small arrows indicate the same cut-offs as in Fig. 26.

$\bar{a}_{sc}^{min} \approx 0.08$. As a comparison, the right panel of Fig. 27 shows the corresponding distribution of the largest Einstein radii extracted from the 1 000 realisations. Evidently, the largest Einstein radii stem by no means exclusively from the haloes with minimal a_{sc}, but from a rather broad range of a_{sc}. More precisely, Fig. 27 indicates that the largest Einstein radii either stem from lowly concentrated and highly elongated haloes, or from less elongated but higher concentrated ones. Nonetheless, we note that the largest maxima, which are represented by the dark red to black dots in the right panel of Fig. 27, are confined to the region of particularly small a_{sc} and low c_e. This explains the strong impact of the cut-off on the shape parameters of the fitted GEV distributions because the cut-off effectively removes the largest maxima and thus leads to steeper CDFs.

Due to the limited knowledge of the statistics of extremely small axis ratios, it is not possible to clearly define a proper choice of the cut-off (if present) until the triaxiality distributions of large halo samples (covering the largest cluster masses) are studied in numerical simulations. In the study of JS02 (see their Figure 9), scaled axis ratios below ~ 0.2 were not found for any of the studied redshifts. The value of $a_{sc}^{min} \sim 0.2$

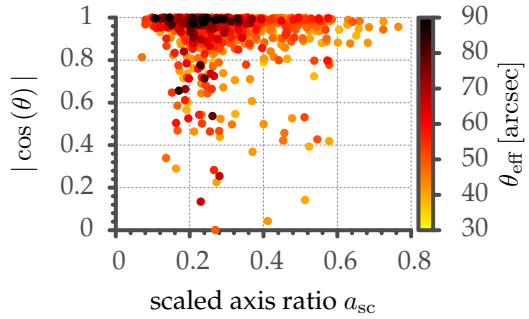

Figure 28: Spatial orientation of the haloes producing the largest Einstein radius as a function of the scaled axis ratio a_{sc}. Here, θ denotes the angle between the major axis of each halo and the line-of-sight direction of the observer.

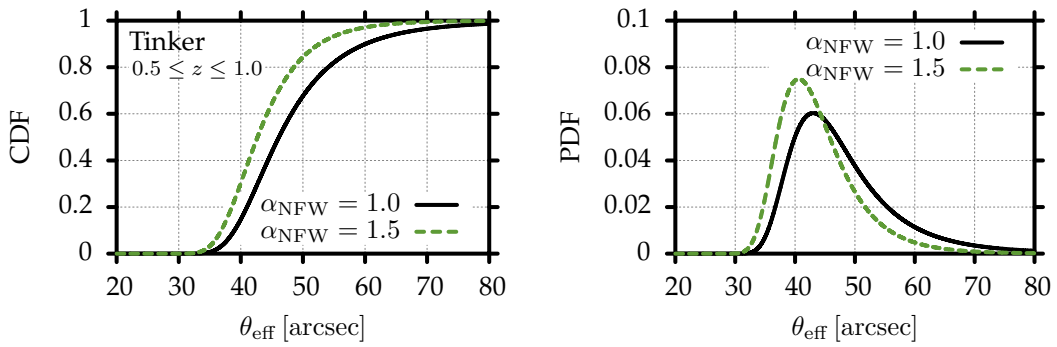

Figure 29: CDFs and PDFs of the largest Einstein radius for different values of the inner slope α_{NFW} of the triaxial density profile.

corresponds to the cut-off on the 3σ level. It should be noted, however, that in general a_{sc} also depends on the underlying cosmology (cf. Eq. (110)).

Finally, Fig. 28 demonstrates the importance of the projection effect mentioned at the beginning of this section: The majority of the largest Einstein radii is produced by strong lenses whose major axis is aligned along the line-of-sight of the observer. Particularly those lenses with favourable alignment and small axis ratio a_{sc} exhibit the largest Einstein radii.

6.3.3 *Impact of the inner slope and the c–M relation*

Figure 29 shows the impact of the inner slope α_{NFW} of the triaxial density profile on the GEV distribution of the largest Einstein radius. The distribution for the steeper inner density profile is shifted to smaller Einstein radii, confirming the findings reported in Oguri & Keeton (2004, p. 669). At first, this result seems a bit unexpected because *on average*, steeper density profiles lead to slightly larger Einstein radii (see e.g. Oguri 2004). However, as discussed in the previous section, highly elongated haloes that are projected along the line-of-sight crucially affect the shape of the GEV distribution. For $\alpha_{\mathrm{NFW}} = 1.0$, the density profiles are slightly shallower, leading to even more extended haloes in the case of small axis ratios. Therefore, the projection effect is even more pronounced, which explains the shift visible in Fig. 29.

Finally, also the concentration–mass (c–M) relation assumed for modelling the triaxial density profile influences the statistics of the largest Einstein radii. We mimic a variation in the c–M relation by computing the GEV distributions for different values of the normalisation parameter A_{e} for the mean concentration $\bar{c}_{\mathrm{e}}$ (cf. Eq. (113)). Assuming a fixed value for the scaled axis ratio a_{sc}, smaller A_{e} correspond to lower values of the mean concentration, implying that lower concentrations c_{e} are more likely to be sampled. Following Oguri et al. (2003), we vary the value of A_{e} between 0.8 and 1.6, with $A_{\mathrm{e}} = 1.1$ being the ΛCDM standard value.

Figure 30 indicates that large values of A_{e} shift the GEV distribution to smaller Einstein radii. As before, this result can be explained by the strength of the projection effect. Most importantly, we conclude that also the assumed c–M relation significantly influences the GEV distribution of the largest Einstein radius.

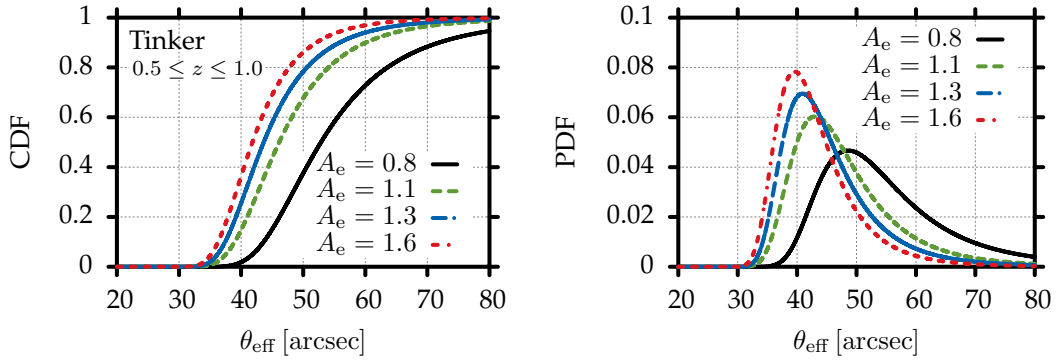

Figure 30: CDFs and PDFs of the largest Einstein radius for different values of the normalisation parameter A_e of the mass-concentration relation from Eq. (114).

6.3.4 *Other important effects*

By presenting the detailed discussion in the previous sections, we mainly intended to highlight the numerous theoretical uncertainties that strongly affect the GEV distribution of the largest Einstein radius. In particular the statistical description of triaxial dark matter haloes (e. g. distribution of axis ratios) needs to be improved.

In addition to the uncertainties discussed above, there are more effects that strongly influence the statistics of the largest Einstein radius. In Chap. 8, we show that the inclusion of cluster mergers significantly shifts the GEV distribution to larger values. Closely related and to some extent equivalent, the inclusion of substructures is expected to have a similar effect. Finally, the brightest cluster galaxy (BCG) can lead to an increase of the strong-lensing effect, but to a lesser extent than the previously discussed effects (Puchwein et al. 2005; Meneghetti et al. 2007; Giocoli et al. 2012).

6.4 MACS J0717.5+3745 – A CASE STUDY

The X-ray luminous galaxy cluster MACS J0717.5+3745, independently observed at redshift $z_{\mathrm{obs}} = 0.546$ by the MACS survey (Ebeling et al. 2001, 2007), and as a host of a diffuse radio source by Edge et al. (2003), is a quite remarkable system. It is connected to a 4 Mpc long large-scale filament (Ebeling et al. 2004) that leads into the cluster and exhibits ongoing merging activity (Ma et al. 2008). Furthermore, the cluster possesses the most powerful known radio halo (Bonafede et al. 2009) and has also been observed via the Sunyaev-Zel'dovich effect (LaRoque et al. 2003; Mroczkowski et al. 2012). A strong-lensing analysis of this highly interesting system revealed that, with $\theta_{\mathrm{eff}} = (55 \pm 3)''$ for an estimated source redshift of $z_s \sim 2.5$, the effective Einstein radius is the largest known at redshifts $z > 0.5$ (Zitrin et al. 2009, 2011).

To assess the occurrence probability of the observed effective Einstein radius of MACS J0717.5+3745, we computed the CDF of the largest Einstein radius for the redshift range $0.5 \leq z \leq 1.0$ based on the Tinker mass function, assuming the nominal MACS survey area ($A_s = 22\,735\,\mathrm{deg}^2$) as well as full sky coverage ($A_s = 41\,153\,\mathrm{deg}^2$), and a source redshift of $z_s = 2.5$. We decided to use the conservative

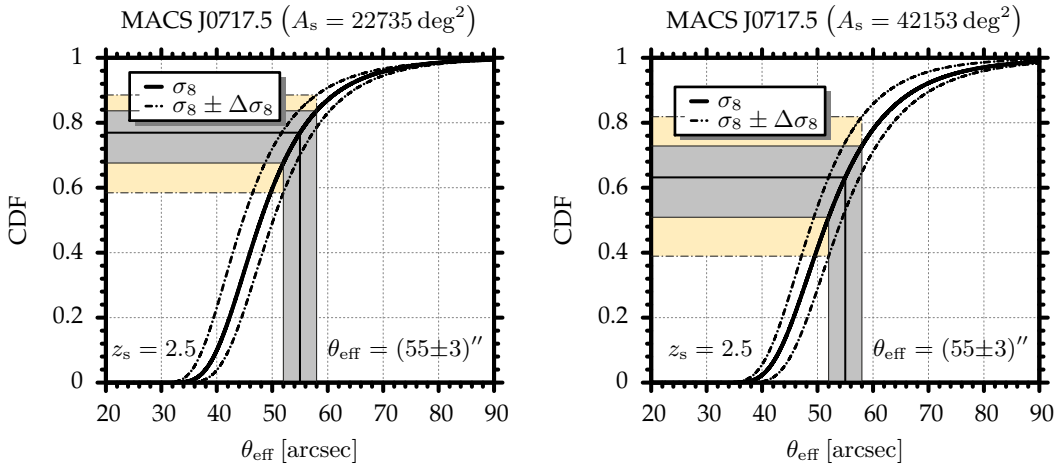

Figure 31: CDFs of the largest Einstein radius for the redshift range $0.5 \leq z \leq 1.0$, a source redshift of $z_s = 2.5$, and the nominal MACS survey area (left panel) as well as the full sky (right panel). The dashed-dotted lines, together with the yellow shaded area, illustrate the impact of the uncertainty in the WMAP7 value of σ_8 on the CDFs. The grey shaded area indicates the uncertainty in the measurement of the Einstein radius.

cut-off $a_{sc}^{cut} = 0.249$, corresponding to the inclusion of 99% of the possible axis ratios from the distribution (110). In doing so, we even cut off the distribution above the most likely minimum of $a_{sc}^{min} = 0.2$. Consequently, the estimated CDF is steeper, resulting in a more conservative estimate of the occurrence probability of a given Einstein radius. In comparison to the previously discussed distributions that assumed a source redshift of $z_s = 2.0$, the higher source redshift assumed here shifts the distribution to larger Einstein radii due to the modified lensing geometry (Oguri & Blandford 2009).

Like the mass function, the uncertainty in the normalisation σ_8 of the matter power spectrum also influences the distribution of the largest Einstein radii, because it influences the number of haloes from which the maxima are drawn. To incorporate the uncertainty in the measured value of σ_8, we also computed the distributions for the upper and lower 1σ limits $\sigma_8 = (0.811 \pm 0.023)$ of the WMAP7+BAO+SNSALT dataset (Komatsu et al. 2011).

The left panel of Fig. 31 shows that, for the nominal MACS survey area, we find an occurrence probability of $\sim (16 - 32)$ per cent based on the uncertainty of the observed Einstein radius θ_{eff} alone. When the additional uncertainty of the precision of σ_8 is included, this range widens to $\sim (11 - 42)$ per cent. When the survey area is extended to the full sky, the CDFs are shifted to larger values, and consequently the occurrence probability for a given observation increases. In the case of MACS J0717.5+3745, we find an occurrence probability of $\sim (18 - 61)$ per cent when taking the uncertainty of σ_8 into account.

From the above ranges of occurrence probabilities, it can be directly inferred that the large critical curve of MACS J0717.5+3745 cannot be considered in tension with the ΛCDM model. This finding is supported by the results of the previous sections, which showed that the uncertainty of the mass function, particularly at the high-mass end, and the uncertainty in the shape of galaxy clusters allow a wide range

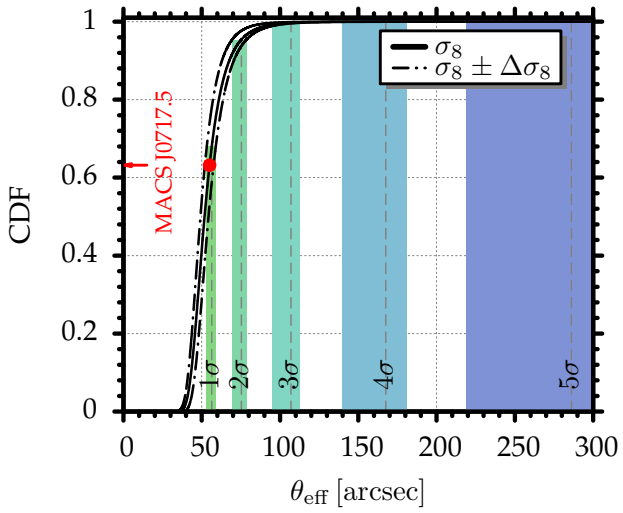

Figure 32: CDF of the largest Einstein radius, assuming a redshift interval of $0.5 \leq z \leq 1.0$, the nominal MACS survey area ($A_{\mathrm{s}} = 22\,735\,\mathrm{deg}^2$), and a source redshift of $z_{\mathrm{s}} = 2.5$. The dashed-dotted lines indicate the impact of the uncertainty in the normalisation σ_8 of the power spectrum as measured by WMAP7 and show, respectively, the CDFs for $\sigma_8 - \Delta\sigma_8$ and $\sigma_8 + \Delta\sigma_8$. The vertical shaded regions denote the range of θ_{eff} values for which these CDFs take a value equal to $n\sigma$, with $n \in [1, 5]$.

of distributions. Moreover, the inclusion of cluster mergers (cf. Chap. 8) further strengthens our conclusions.

With this in mind, the occurrence probabilities inferred above should just be considered a rough estimate. Because of the uncertainties in modelling the distribution of Einstein radii, an observed critical curve should exhibit a much larger extent in order to be taken as clearly in tension with the ΛCDM model. To quantify this statement, we used the previously derived CDFs for MACS J0717.5+3745 to calculate the values of the Einstein radius θ_{eff} for which the CDFs take values that correspond to confidence levels $n\sigma$ with $n \in [1, 5]$. Figure 32 indicates that in order to lie beyond the 3σ level, corresponding to an occurrence probability of ~ 0.3 per cent, and to account for the uncertainty stemming from σ_8, the Einstein radius θ_{eff} should be larger than $\sim 115''$.

6.5 CONCLUSIONS

In this chapter, we described a new semi-analytic approach for applying the theory of extreme value statistics to the distribution of the single largest Einstein radius in a given cosmological volume. Our work can be divided into three distinct parts: first, a preparatory study; second, a study of the effects that impact on the distribution of the maximum Einstein radius; and third, a case study for MACS J0717.5+3745.

In the first preparatory part, we showed that $\sim$ 1 000 independently sampled maxima are sufficient to accurately estimate the distribution of the largest Einstein radius, and that the resulting distribution converges to the GEV distribution. In general, we found that the distribution of the largest Einstein radius can be well described by a Fréchet (Type II) distribution, indicating that the distribution is bounded from below. Furthermore, we confirmed the findings of Oguri & Blandford (2009) that the sample of maxima is distributed in a wide range in the mass–redshift plane, revealing that the single largest Einstein radius has its origin by no means necessarily in the most massive halo of a given mock realisation. This shows that other properties of the strongest lenses (such as profile shape, orientation, etc.) have a stronger impact on the GEV distribution than mass.

We demonstrated that the precise choice of the mass function, the normalisation of the matter power spectrum σ_8, the concentration–mass relation assumed for modelling the haloes, the statistics of (small) axis ratios, and the inner slope of the triaxial density profile strongly affect the resulting GEV distribution of the largest Einstein radius. Many of these theoretical uncertainties should carefully be studied in future works before the extreme value statistics of the largest Einstein radius can be used for a reliable consistency test of the ΛCDM model.

In the last part, we studied the occurrence probability of the largest known Einstein radius observed in the galaxy cluster MACS J0717.5+3745 (Zitrin et al. 2009). Accounting only for the uncertainty in σ_8, we found an occurrence probability of $\sim (11 - 42)$ per cent for the MACS survey area and of $\sim (18 - 61)$ per cent for the full sky, indicating that this observation cannot be considered in conflict with ΛCDM. This conclusion is supported by the fact that the probability range would widen further if accounted for the uncertainties in the underlying assumptions (e. g. extreme axis ratios), and also considering that cluster mergers additionally shift the GEV distribution to larger Einstein radii (cf. Chap. 8), rendering any claim of tension with ΛCDM untenable.

7

THE ORDER STATISTICS OF THE LARGEST EINSTEIN RADII

ABSTRACT

In the previous chapter, we focused on the extreme value distribution of the single largest Einstein radius. Here, we show that our previous approach can meaningfully be extended by studying the order statistics of the n largest Einstein radii. This extension is advantageous because it allows formulating more robust ΛCDM exclusion criteria based on n observations instead of a single extreme strong-lensing event, which might be caused by a highly unlikely, very peculiar lensing system (e. g. a statistical outlier). We apply these exclusion criteria to a selected sample of twelve MACS clusters, finding that their remarkably large Einstein radii do not exceed the theoretical expectations of the ΛCDM model. This conclusion is further corroborated by the large uncertainties that enter the semi-analytic lens modelling and to which the largest Einstein radii are particularly sensitive.

The contents of this chapter were published in Waizmann et al. (2014). In comparison to the published article, we shortened and rewrote several sections.

7.1 INTRODUCTION

The previous chapter discussed the idea to formulate ΛCDM exclusion criteria based on the extreme value statistics of the largest Einstein radius in a certain cosmological volume. However, inference based on a single observation is difficult for it is a priori unknown whether the maximum was really drawn from the supposedly underlying distribution, or whether the event was caused by a very peculiar situation in the concrete survey that was statistically not accounted for. This is particularly important for strong-lensing systems, which are heavily influenced by a number of different physical effects (extreme axis ratios, projection effects, mergers, etc.). It is therefore desirable to formulate ΛCDM exclusion criteria that are based on a number of observations instead of a single event.

This goal can be accomplished by applying order statistics to the distribution of the n largest Einstein radii. To outline this idea, we first introduce the mathematical prerequisites of order statistics in Sect. 7.2. Using (almost) the same approach as in the previous chapter, we obtain the order statistics by semi-analytically sampling the hierarchy of the largest Einstein radii in a predefined cosmological volume. We summarise this semi-analytic approach in Sect. 7.3 and also briefly characterise the

population of those clusters producing the largest Einstein radii. By fitting the GEV distribution to the empirically sampled distribution of maxima, we can derive analytic expressions for the lower order distributions (e. g. the distribution of the second largest Einstein radius), and eventually use these relations to formulate ΛCDM exclusion criteria. In Sect. 7.4.1, we demonstrate the practicality of this ansatz: We compute the theoretically expected order statistics for the cosmological volume containing the twelve MACS clusters analysed by Zitrin et al. (2011), formulate explicit exclusion criteria, and compare these results with the large observed Einstein radii of the MACS sample. Finally, in Sect. 7.5, we present our conclusions.

Throughout this chapter, we adopt the best-fitting cosmological parameters obtained from the Wilkinson Microwave Anisotropy Probe seven-year data (WMAP7; Larson et al. 2011), $(\Omega_{\Lambda 0}, \Omega_{\mathrm{m}0}, \Omega_{\mathrm{b}0}, h, \sigma_8) = (0.727, 0.273, 0.0455, 0.704, 0.811)$. Moreover, we set the inner slope α of the triaxial density profile to the conservative value of $\alpha = 1.0$ (cf. Eq. (107)), fix the normalisation of the concentration-mass relation to $A_{\mathrm{e}} = 1.1$ (cf. Eq. (114)), and force the scaled axis ratio a_{sc} (minor axis) to lie within the 99% confidence interval of the distribution (110) to avoid unrealistic density profiles with extremely small axis ratios and too low concentrations (cf. Sect. 6.3.2).

7.2 ORDER STATISTICS

In this section, we briefly summarise the mathematical prerequisites of order statistics that are needed for the remainder of this work. A more thorough treatment can be found in the excellent textbooks of Arnold et al. (1992) and David & Nagaraja (2003) or, in a cosmological context, in Waizmann et al. (2013).

Suppose that $\{X_1, X_2, \ldots, X_n\}$ is a random sample of a continuous population with the PDF $f(x)$ and the corresponding CDF $F(x)$. Then, the order statistic is given by the random variates ordered by magnitude $X_{(1)} \leq X_{(2)} \leq \cdots \leq X_{(n)}$, where $X_{(1)}$ is the smallest (minimum) and $X_{(n)}$ denotes the largest (maximum) variate in the sample. The PDF of the i-th order $X_{(i)}$ $(1 \leq i \leq n)$ is then found to be

$$f_{(i)}(x) = \frac{n!}{(i-1)!(n-i)!} \left[F(x)\right]^{i-1} \left[1 - F(x)\right]^{n-i} f(x) \,. \tag{133}$$

Correspondingly, the CDF of the i-th order is given by

$$F_{(i)}(x) = \sum_{k=i}^{n} \binom{n}{k} \left[F(x)\right]^{k} \left[1 - F(x)\right]^{n-k} \,. \tag{134}$$

The distribution functions of the special cases of the lowest and the highest values are then readily found to be

$$F_{(1)}(x) = 1 - \left[1 - F(x)\right]^{n} \,, \tag{135}$$

and

$$F_{(n)}(x) = \left[F(x)\right]^{n} \,. \tag{136}$$

For large sample sizes, both $F_{(1)}(x)$ and $F_{(n)}(x)$ can be described by a member of the GEV distribution (see Sect. 6.2.1).

The distribution functions of the single-order statistics can be generalised to n-dimensional joint distributions. In this chapter, we do not go beyond the two-order statistics for which the joint PDF $X_{(r)}, X_{(s)}$ $(1 \leq r < s \leq n)$ reads

$$f_{(r)(s)}(x,y) = \frac{n!}{(r-1)!(s-r-1)!(n-s)!} f(x)f(y) \times [F(x)]^{r-1} [F(y)-F(x)]^{s-r-1} [1-F(y)]^{n-s} \ , \tag{137}$$

where we assumed $x < y$. The joint CDF can be derived by integrating the above PDF, or by a direct argument (Arnold et al. 1992, Sect. 2.2), and is given by

$$F_{(r)(s)}(x,y) = \sum_{j=s}^{n} \sum_{i=r}^{j} \frac{n!}{i!(j-i)!(n-j)!} \times [F(x)]^{i} [F(y)-F(x)]^{j-i} [1-F(y)]^{n-j} \ . \tag{138}$$

We refer to Appendix A of Waizmann et al. (2013) for more details on the implementation of the single-order and two-order statistics.

Finally, we need to emphasise an important ambiguity concerning the nomenclature used in the following sections. In line with the previous chapters, we exclusively focus on the order statistics of the strongest lenses. Adopting the standard convention of the mathematical literature, and also following the above definitions, we would have to refer to the statistics of the n-th order, the $(n-1)$-th order, the $(n-2)$-th order, and so on, to denote the statistics of the largest, the second largest, and the third largest Einstein radius. However, this nomenclature would unnecessarily complicate our discussion in some paragraphs or the labelling of figures. From here on, we therefore define to additionally use the term *rank* to refer to Einstein radii in *descending order*, that is, we define that the i-th rank corresponds to the $(n+1-i)$-th order. To refer to the statistics of the fourth largest Einstein radius, for instance, we could either simply refer to the statistics of the fourth rank or, equivalently, to the $(n-3)$-th order.

7.3 SAMPLING THE ORDER STATISTICS

The approach for sampling the order statistics of Einstein radii is identical to the one used in the previous chapter: We create a large number of mock realisations of the cluster population on the PNC, compute their strong-lensing characteristics, and collect the Einstein radii of the highest orders. Throughout this chapter, we used the Tinker et al. (2008) mass function to sample representative halo populations. Because we eventually intend to compare our sampled distributions with the twelve MACS clusters observed at redshifts $z > 0.5$, we focused our analysis of the order statistics of the largest Einstein radii on clusters in the redshift range $0.5 \leq z \leq 1$. In line with the strong-lensing analysis by Zitrin et al. (2011), we assumed a fixed source redshift of $z_\mathrm{s} = 2.0$.

In the previous chapter, we showed that $\sim 1\,000 - 2\,000$ independent maxima are sufficient for accurately sampling the CDF of the largest Einstein radius and that the maxima stem from haloes with masses $M > 2 \times 10^{14}\, M_\odot / h$. While the first statement

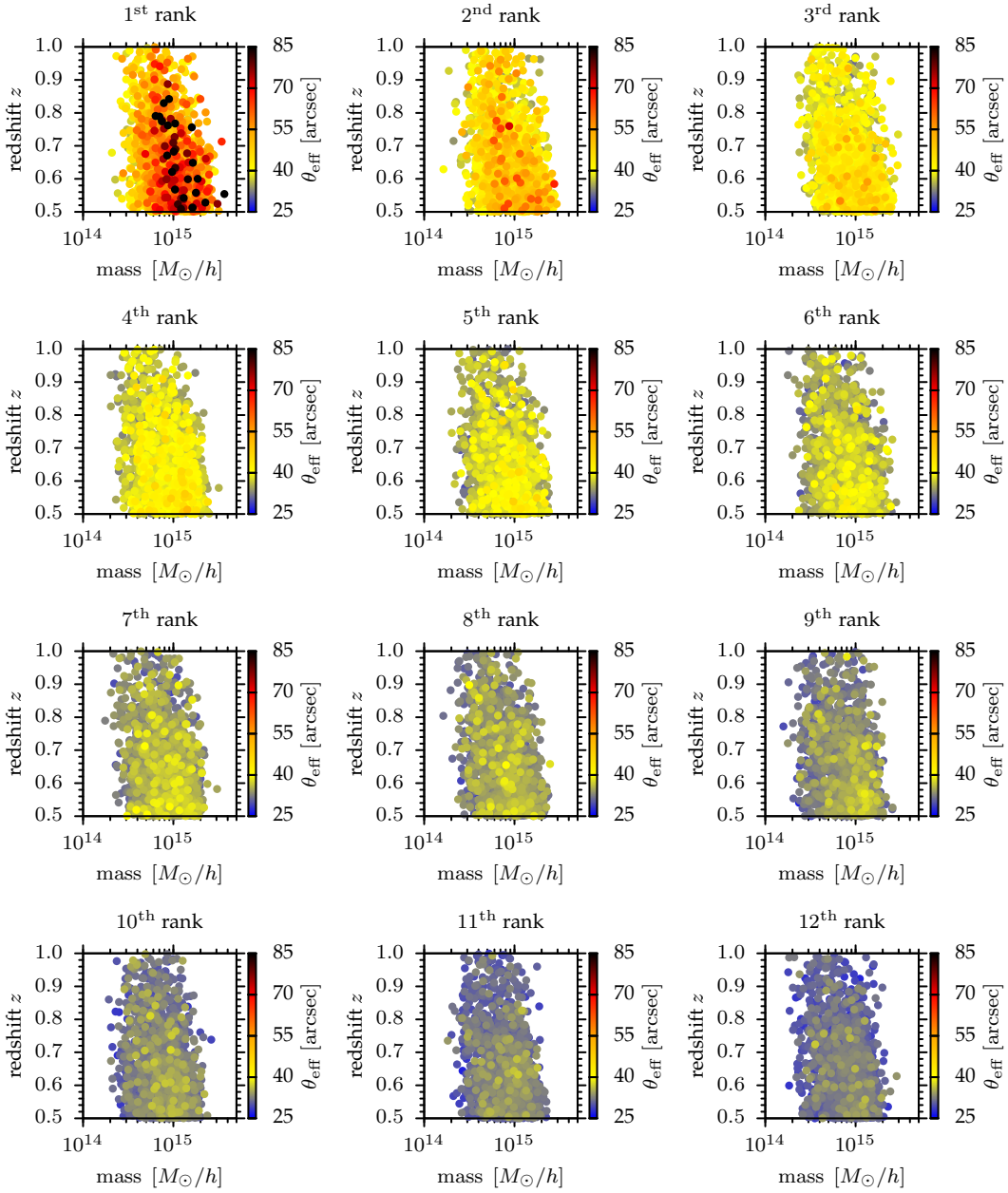

Figure 33: Mass and redshift distributions of the gravitational lenses that exhibit the twelve largest Einstein radii. The distributions were extracted from 2 000 mock realisations of Einstein radii in the redshift interval $0.5 \leq z \leq 1.0$ on the full sky.

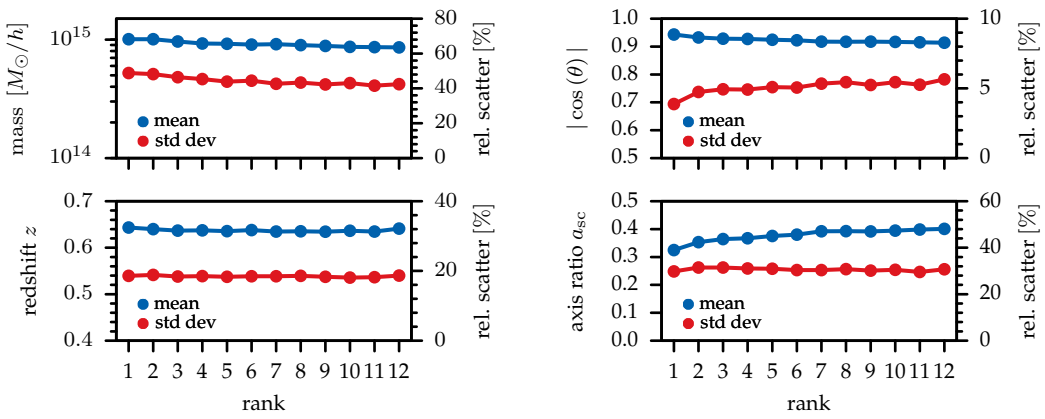

Figure 34: Sample mean (blue lines) and relative scatter (red lines) of the halo mass (upper-left panel), the redshift (lower-left panel), the alignment $|\cos(\theta)|$ (upper-right panel), and the scaled axis ratio a_{sc} (lower-right panel) as a function of the rank.

will certainly also hold for the order statistics, the second might not be valid any more for distributions of lower orders of the Einstein radius. To verify the second assumption, we decided to sample 2 000 mock realisations of the cosmological volume considered, adopting a lower mass limit of $M_{lim} = 10^{14}\,M_\odot/h$. The distribution in mass and redshift for the twelve largest Einstein radii is shown in Fig. 33, which clearly demonstrates that, also for the lower orders, only a few values fall below the previous limit of $M > 2 \times 10^{14}\,M_\odot/h$. In the following, we thus adopt the more conservative lower mass limit of $M_{lim} = 10^{14}\,M_\odot/h$.

Figure 33 indicates that all orders stem from a wide range of masses. This tendency is further confirmed by Fig. 34, which shows the dependence of the sample mean and the relative scatter in mass and redshift for the first twelve ranks. It can be seen that the sample mean in mass (upper-left panel) weakly drops with increasing rank and exhibits a large relative scatter of ~ 40 per cent. Although, on average, the sample of the largest Einstein radii stems from massive clusters with masses $M \sim 10^{15}\,M_\odot$, the large scatter indicates that also notably less massive clusters likely contribute to this ordered list of very large Einstein radii. The sample mean of the clusters' redshifts (lower-left panel) is independent of the rank and shows a relative scatter of ~ 20 per cent. This is because the distribution in redshift is mainly determined by the lensing geometry, which is, of course, independent of the considered order.

In addition to the mass and redshift distributions, it is interesting to examine how the orientation of the haloes and their scaled axis ratios depend on the different orders. For this purpose, we also calculated the sample mean and the relative scatter of the alignment $|\cos(\theta)|$ and the scaled axis ratio, a_{sc} (cf. Sect. 6.3.2). A value of $|\cos(\theta)| = 1$ corresponds to a perfect alignment of the halo's major axis with the line-of-sight of the observer. The upper-right panel of Fig. 34 indicates that the mean alignment for the first twelve ranks is high (> 0.9), but slightly decreases with increasing rank. Thus, the higher the rank, the more likely it happens that the haloes are slightly misaligned with the line-of-sight. This result can be easily understood. For the very largest Einstein radii, all parameters (mass, orientation, concentration, etc.) simultaneously

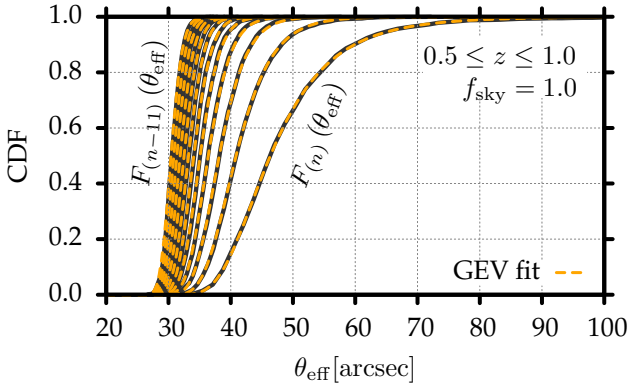

Figure 35: CDFs of the twelve largest Einstein radii. The black solid lines depict the empirically sampled CDFs. The orange dashed lines indicate the GEV fits to the CDFs.

need to be most beneficial in terms of the strong-lensing efficiency. For higher ranks, a slightly disadvantageous setting of one parameter (e. g. a slightly misaligned halo) can still be compensated for by other halo properties. Nevertheless, the smallness of the relative scatter of the alignment with respect to the observer demonstrates that this property is an important characteristic of the sample of the strongest lenses. Closely related to the alignment is the elongation of the lensing-halo, which is encoded in the scaled axis ratio. In the lower-right panel of Fig. 34, we therefore present the dependence of the mean and relative scatter of $a_{\rm sc}$ on the rank. A low value of $a_{\rm sc}$ indicates a very elongated system, while a halo with $a_{\rm sc} = 1$ is spherical. The increase of the mean with increasing rank indicates that the higher ranks likely stem from less elongated haloes.

We summarise that, on average, the twelve largest Einstein radii stem from haloes with masses $M \sim 10^{15}\,M_\odot$. However, halo orientation and triaxiality (i. e. elongation) are influential factors that individually allow clusters with lower masses to produce very large Einstein radii.

7.4 COMPARISON WITH OBSERVATIONS

7.4.1 *Theoretical distributions of the order statistics*

Employing the semi-analytic approach described in Sect. 7.3, we now sample the order statistics of the largest Einstein radii in the redshift range $0.5 \leq z \leq 1.0$, assuming full sky coverage.

Figure 35 reveals that the CDFs of the twelve highest orders steepen as the order decreases; a similar effect was found by Waizmann et al. (2012a), who studied the order statistics of the most massive and most distant galaxy clusters. In comparison to the highest order $F_{(n)}$, which is broad and allows the largest Einstein radius to be realised in a wide range, the lower orders are confined to an increasingly narrow range of Einstein radii. Therefore, the higher order CDFs can, in principle, be used to formulate tighter exclusion criteria.

The orange dashed curves in Fig. 35 depict analytic fits to the empirically sampled CDFs. These fits were computed using the following recipe: We first fitted the GEV distribution (cf. Sect. 6.2.1) to the distribution of the maxima $F_{(n)}$, finding the best-fit

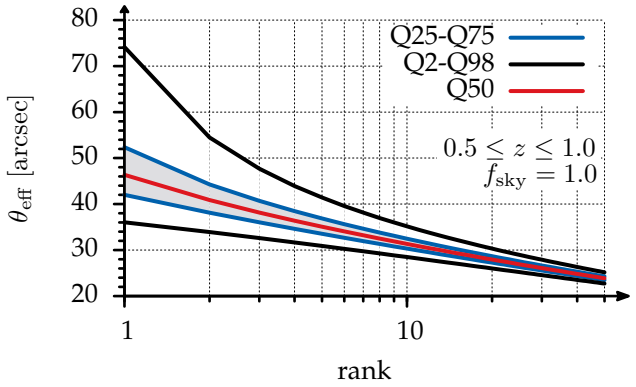

Figure 36: Different percentiles of the CDFs of the largest Einstein radii as a function of rank. The red line depicts the median (Q50), the blue lines the inner quartile range (Q25-Q75), and the black lines the 2 percentile (Q2, lower curve) and the 98 percentile (Q98, upper curve). The latter can be used as ΛCDM exclusion criterion.

parameters $\alpha = (43.52 \pm 0.017)$, $\beta = (6.14 \pm 0.026)$ and $\gamma = (0.13 \pm 0.005)$. Then, using the relation from Eq. (136), we inferred the underlying distribution $F(\theta_{\mathrm{eff}})$, which can in turn be used to derive analytic relations for the order statistics of the n largest Einstein radii. Figure 35 confirms that the fitted order statistics match the empirically sampled distributions very well, confirming the consistency of the higher order CDFs.

Applying order statistics to Einstein radii allows exclusion criteria to be formulated as a function of rank, as presented in Fig. 36. Choosing the 98 percentile as ΛCDM exclusion criterion, for instance, one would need to find approximately twenty Einstein radii with $\theta_{\mathrm{eff}} \gtrsim 30''$, ten with $\theta_{\mathrm{eff}} \gtrsim 35''$, five with $\theta_{\mathrm{eff}} \gtrsim 42''$, or one with $\theta_{\mathrm{eff}} \gtrsim 74''$ on the full sky, in order to claim tension with the ΛCDM expectations. We recall that these exclusion criteria can be considered conservative because here we modelled the distribution of Einstein radii using the simple semi-analytic method that does not incorporate cluster mergers.

For convenience, we use the fitted distributions in what follows. Any small error introduced by this choice is negligible in comparison to the numerous model uncertainties (cf. Sect. 6.3).

7.4.2 *Comparison with the MACS sample*

We now compare the theoretical order statistics with the Einstein radii of the twelve high-redshift ($z > 0.5$) MACS clusters reconstructed by Zitrin et al. (2011). The results of their strong-lensing analysis are summarised in Table 6 (p. 104).

Figure 37 compares the theoretical order statistics with the observed Einstein radii in the form of a box-and-whisker diagram. Defining outliers with respect to the ΛCDM expectations as observations that exceed the 98 percentile, none of the twelve observed Einstein radii falls outside the expectations for the full sky. The result that all observed Einstein radii with rank larger than five fall below the 2 percentile, with a much steeper slope, is a clear indication that the MACS sample is incomplete in terms of the largest Einstein radii that are expected to be found in on the full sky. Because the strongest lenses stem from a wide range in mass, a much larger sample than that covered by the MACS survey (which only focused on very massive clusters) would be required to extract a complete statistic of the largest Einstein radii.

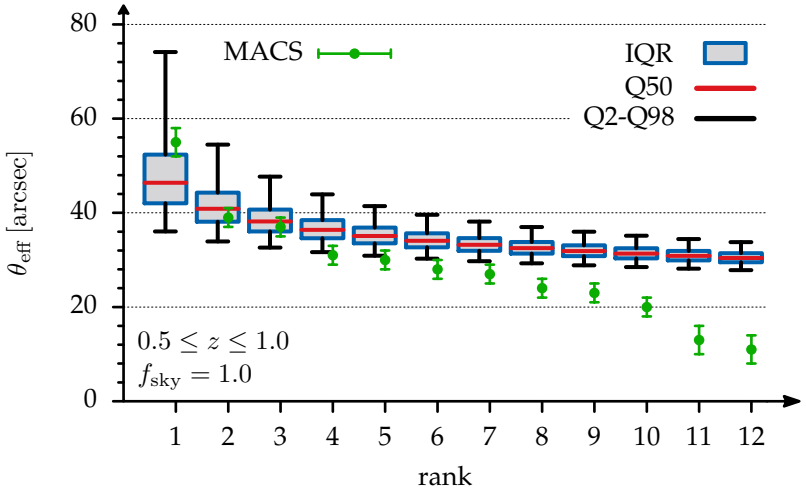

Figure 37: Box-and-whisker diagram for the comparison of the theoretically expected order statistics with the twelve observed Einstein radii of the MACS cluster sample as listed in Table 6. For each rank, the red lines denote the median (Q50), the blue bordered grey boxes give the inner-quartile-range (IQR), and the black whiskers mark the range between the 2 and 98 percentile (Q2, Q98) of the theoretical distribution. The green error bars represent the observed Einstein radii (Zitrin et al. 2011).

It is important to stress that we computed the order statistics of the largest Einstein radii for (fictitious) all-sky realisations, although the nominal survey area of the MACS survey comprises only a fraction of the full sky ($A_{\rm s} = 22\,735\,{\rm deg}^2$). By reducing the effective survey area, we would decrease the cluster sample from which the largest Einstein radii are drawn, and consequently the theoretical distributions would be shifted to slightly lower values of $\theta_{\rm eff}$. In addition, we could try to mimic the same selection criteria that were applied to define the cluster sample covered by the MACS survey. This is, however, a fairly complicated procedure, which is additionally subject to many uncertainties.

On the other hand, it is also important to stress that we completely neglected the impact of cluster mergers here, which substantially increase the Einstein radii of the strongest lenses (cf. Chap. 5). In addition, recent measurements of the Planck satellite (Planck Collaboration et al. 2013) indicate higher values of the matter density parameter $\Omega_{\rm m0}$ and the normalisation σ_8 of

Table 6: Summary of the strong-lensing analysis of the twelve MACS clusters analysed by (Zitrin et al. 2011). The clusters are ordered (descending) by their Einstein radius.

MACS	z	$\theta_{\rm eff}$ [arcsec]
J0717.5+3745	0.546	55 ± 3
J0257.1-2325	0.505	39 ± 2
J2129.4-0741	0.589	37 ± 2
J0744.8+3927	0.698	31 ± 2
J0025.4-1222	0.584	30 ± 2
J0647.7+7015	0.591	28 ± 2
J1149.5+2223	0.544	27 ± 3
J0018.5+1626	0.545	24 ± 2
J2214.9-1359	0.503	23 ± 2
J1423.8+2404	0.543	20 ± 2
J0454.1-0300	0.538	13^{+3}_{-2}
J0911.2+1746	0.505	11^{+3}_{-1}

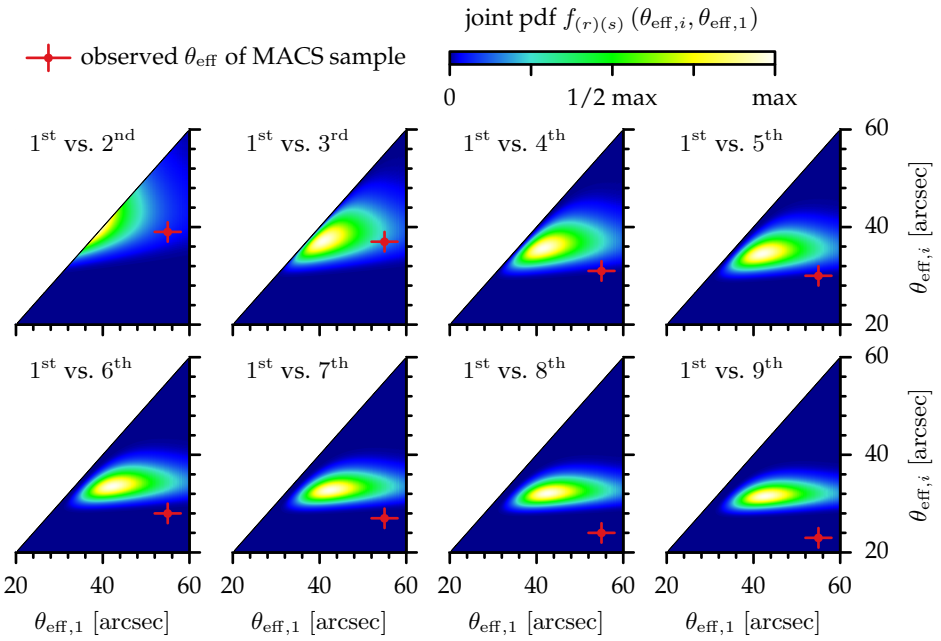

Figure 38: PDFs of the joint two-order statistics for different combinations of the first rank $\theta_{\mathrm{eff},1}$ (x-axis) with higher ranks $\theta_{\mathrm{eff},i}$ (y-axis). The distributions were calculated for the redshift range $0.5 \leq z \leq 1.0$ on the full sky. The color bar is set to range from zero to the maximum of the individual joint PDF in each panel. The red error bars indicate the observed Einstein radii as listed in Table 6. The PDFs are limited to a triangular domain due to the ordering constraint $\theta_{\mathrm{eff},i} < \theta_{\mathrm{eff},1}$ (cf. Eq. (137)).

the matter power-spectrum than the WMAP7 values used in this chapter. Higher values of Ω_{m0} and σ_8 would increase the abundance of high-mass haloes, which in turn would shift the order statistics to larger Einstein radii and consequently render the MACS sample even more likely. Finally, we recall that several theoretical uncertainties (such as extreme axis ratios; cf. Sect. 6.3) affect the semi-analytic modelling of the distribution of the largest Einstein radii.

Taking these remarks into account, we conclude that there is no reliable statistical evidence for the large Einstein radii of the twelve MACS clusters to exceed the theoretical expectations of the ΛCDM model. In the following chapter, we explicitly demonstrate that this conclusion is further strengthened by including cluster mergers.

7.4.3 *Joint distributions*

Apart from the study of the individual order statistics, it is also possible to derive joint distributions for different orders by means of Eqs. (137) and (138). We exemplarily present the joint PDFs for combinations of the highest order with lower orders in Fig. 38.

It can be seen that the largest and the second largest Einstein radius are likely equally large (upper-left panel), while Einstein radii of higher ranks are, on average, notably smaller than the maximum. Furthermore, the peak of the joint PDF narrows

for the smaller Einstein radii (y-axis) with increasing rank, which is a consequence of the steepening of the CDFs as shown in Fig. 35. Finally, we note that the observed Einstein radii (red crosses) fall increasingly below the peak of the joint PDFs. Similarly as in Fig. 37, this is a manifestation of the incompleteness of the observed sample.

The joint PDFs shown in Fig. 38 also imply that the ratio of Einstein radii of different orders could itself be an important diagnostic. It may even be more robust than the Einstein radii themselves because the absolute calibration may drop out.

Finally, we note in passing that the joint PDFs considered above can easily be extended to higher dimensions. Waizmann et al. (2013) outlined this approach for the order statistics of clusters in mass and redshift.

7.5 CONCLUSIONS

In this chapter, we presented a new framework for calculating the individual and joint order distributions of the n largest Einstein radii in a given cosmological volume. The method can easily be adapted to different conditions (e. g. survey size, redshift range, cosmological parameters) and potentially constitutes a valuable consistency check of the underlying cosmological model.

The order statistics of the largest Einstein radii can be considered an extension of the extreme value statistics of the maximum Einstein radius studied in the previous chapter and allows formulating ΛCDM exclusion criteria that are based on n observations instead of a single one. The CDFs of the twelve largest Einstein radii steepen with decreasing order, indicating that the lower orders are, in principle, more constraining. Moreover, we found that the twelve strongest lenses stem from a wide range in mass, but are, on average, well aligned along the line-of-sight and exhibit highly elongated, triaxial density profiles. These findings support the notion that, for the sample of the largest Einstein radii, triaxiality and halo alignment along the line-of-sight matter more than mass.

Most importantly, we demonstrated that large Einstein radii of the twelve high-redshift MACS clusters analysed by Zitrin et al. (2011) do not exceed the theoretical expectations of the ΛCDM model. Taking current theoretical uncertainties into account, much larger Einstein radii would have to be observed to seriously challenge the concordance model.

8

THE ORDER STATISTICS OF THE LARGEST EINSTEIN RADII WITH CLUSTER MERGERS

ABSTRACT

Based on techniques developed in the previous chapters, we investigate the impact of galaxy-cluster mergers on the order statistics of the largest Einstein radii. We show that the inclusion of mergers significantly shifts the extreme value distribution of the largest Einstein radius to higher values, typically increasing the expected value by $\sim$10%. A comparison with current data reveals that the largest observed Einstein radius agrees excellently well with the theoretical predictions of the ΛCDM model at redshifts $z > 0.5$. At redshifts $z < 0.5$, our results are somewhat more controversial. Although cluster mergers also increase the expected values of the order statistics of the n largest Einstein radii by $\sim$10%, the theoretically expected values are notably lower ($\sim 3\sigma$ deviation for $n = 12$) than the largest Einstein radii of a selected sample of SDSS clusters in the redshift range $0.1 \leq z \leq 0.55$. The uncertainties of the observed Einstein radii are still large, however, and thus the measurements need to be carefully revised in future works. Therefore, given the premature state of current observational data, overall, there is still no reliable statistical evidence for observed Einstein radii to exceed the theoretical expectations of the standard cosmological model.

The contents of this chapter were published in Redlich et al. (2014b).

8.1 INTRODUCTION

Do the strongest observed gravitational lenses exceed the theoretical expectations of the standard cosmological model? This question has long been debated in the literature (see Bartelmann 2010b; Meneghetti et al. 2013, for reviews), and was the central theme of the previous chapters.

However, so far, our analysis is still incomplete in the following sense: while we explicitly emphasised the importance of cluster mergers for the statistics of the strongest lenses in Chap. 5, we did not include mergers in our computations of Chaps. 6 and 7. This decision was motivated by several factors. Firstly, particularly in Chap. 6, we investigated the properties of triaxial lenses (such as orientation and profile shape) that decisively affect the extreme value distribution of the largest Einstein radius. For these studies, it was important to isolate individual effects, and therefore it was neither desirable nor required to include cluster mergers. Secondly, we aimed to derive conservative exclusion criteria. We were able to show that the strongest

observed lenses do not exceed the theoretical expectations of the standard cosmological model even if cluster mergers are neglected. Because mergers additionally boost the strong lensing efficiency, including these events should additionally consolidate this conclusion. Thirdly, including cluster mergers is computationally very expensive. A typical realisation of a mock universe requires MC simulations of $\sim 10^6$ merger trees. In addition, lensing computations with multiple haloes in the field of view are substantially more expensive than those with single haloes. To estimate the order statistics of the largest Einstein radii with an acceptable precision, $\sim 10^3$ mock universes have to be sampled. This whole procedure is computationally very demanding, even though our semi-analytic method was specifically tailored to be fast.

In this sense, this chapter completes our discussion of the strongest gravitational lenses. Based on previously developed techniques, we compute the impact of cluster mergers on the order statistics of the largest expected Einstein radii in the Universe. This is not only interesting in itself, but also because it differs from the analysis performed in Chap. 5, where we investigated the impact of cluster mergers on averaged quantities such as the optical depth for giant gravitational arcs. Moreover, we compare our theoretical results to another, independent set of observational data at redshifts $z < 0.5$ (Zitrin et al. 2012), finding that the observed lenses in this cosmological volume might either be somewhat stronger than theoretically expected, or the substantial extrapolation employed by Zitrin et al. (2012) to infer the Einstein radii is dubious.

The plan for this chapter is as follows: Section 8.2 describes the new merger tree algorithm used for this chapter, and also contains some information on speeding up the computations. The impact of cluster mergers on the order statistics of the largest Einstein radii is analysed in Sect. 8.3. Thereafter, in Sect. 8.4, we compare our theoretical predictions with current observational data. In Sect. 8.5, we summarise our main results and finally conclude.

Throughout this chapter, we adopt the best-fitting cosmological parameters derived from the Planck 2013 data, $(\Omega_{\Lambda 0}, \Omega_{\mathrm{m}0}, \Omega_{\mathrm{b}0}, h, \sigma_8) = (0.685, 0.273, 0.047, 0.673, 0.829)$ (Planck Collaboration et al. 2013). Moreover, we set the inner slope α of the triaxial density profile to the conservative value of $\alpha = 1.0$ (cf. Eq. (107)), fix the normalisation of the concentration-mass relation to $A_{\mathrm{e}} = 1.1$ (cf. Eq. (114)), and force the scaled axis ratio a_{sc} (minor axis) to lie within the 99% confidence interval of the distribution (110) to avoid unrealistic density profiles with extremely small axis ratios and too low concentrations (cf. Sect. 6.3.2).

8.2 ALGORITHM FOR INCLUDING CLUSTER MERGERS

8.2.1 *Extended Press-Schechter merger tree algorithm*

In Chap. 5, we developed a semi-analytic method that allows us to project merging galaxy clusters onto a fictitious observer's PNC and calculate their strong-lensing properties. Moreover, we emphasised that we employed two completely independent algorithms to compute the strong-lensing statistics: (1) a standard MC approach to sample isolated haloes from a given mass function, and (2) our new method that

incorporates cluster mergers. We did so in preparation of the following applications, but also to independently cross-check the new merger algorithm. For self-consistency, the two methods had to be based on the original mass function of Press & Schechter (1974).

On the other hand, in Sect. 6.3.1 we found that the precise choice of the halo mass function has a significant impact on the GEV distribution of the largest Einstein radius. Because it is based on the overly idealistic theory of spherical collapse, the mass function of Press & Schechter (1974) is known to underestimate the abundance of high-mass haloes, which in turn leads to lower expectation values for the largest Einstein radius in a given cosmological volume. Conversely, the mass function of Sheth & Tormen (1999) over-predicts the number of high-mass haloes, which shifts the GEV distribution to too high values. The Tinker et al. (2008) (Tinker) mass function is a compromise between these two extremes and is broadly accepted as a more accurate representation of the mass function determined from N-body simulations. Therefore, all calculations of Chap. 7 were based on the Tinker mass function.

In this chapter, we aim to calculate the order statistics of the largest Einstein radii as realistically as possible, so that our results can be compared with real observations. It would therefore be desirable to replace the original merger algorithm by an alternative algorithm that generates halo catalogues consistent with the Tinker mass function.

Jiang & van den Bosch (2014) recently compared several different merger tree codes, finding that the algorithm proposed by Parkinson et al. (2008) (PCH) reproduces the merger rates measured in N-body simulations most accurately. The basic idea of the PCH algorithm is quite simple: although merger algorithms based on the original extended Press-Schechter formalism are slightly inaccurate, they are certainly not completely unacceptable. Instead, they exhibit statistical properties (such as trends with mass and redshift) that agree well with those of merger trees constructed from N-body simulations. Parkinson and co-workers thus proposed to take the Press-Schechter merger rate as a starting point, and slightly perturb this quantity using an empirically motivated function. The probability for drawing a progenitor of mass M_1 from a parent halo of mass M_0 at redshift z is then modified according to

$$\frac{\mathrm{d}N}{\mathrm{d}M_1} \rightarrow G\left(M_0, M_1\right) \frac{\mathrm{d}N}{\mathrm{d}M_1}, \quad G\left(M_0, M_1\right) = G_0 \left[\frac{\sigma\left(M_1\right)}{\sigma\left(M_0\right)}\right]^{\gamma_1} \left[\frac{\delta\left(z\right)}{\sigma\left(M_0\right)}\right]^{\gamma_1}, \quad (139)$$

where $\delta(z)$ is the linear density threshold for collapse and $\sigma\left(M\right)$ denotes the rms linear density fluctuation extrapolated to redshift $z = 0$ in spheres containing mass M (Lacey & Cole 1993). G_0, γ_1 and γ_2 are free empirical parameters of this ansatz, which PCH constrained by fitting their algorithm to merger trees extracted from the Millennium simulation (Springel et al. 2005).

While testing our implementation of the PCH algorithm, we observed that the algorithm calibrated with the best-fitting parameters given by PCH still notably underpredicts the abundance of high-mass haloes ($\sim 10^{15} M_{\odot}/h$). More accurate results can be achieved with the parameters given by Benson (2008), who employed a slightly different fitting procedure. In this chapter, we thus used the values derived by Benson (2008): $G_0 = 0.605$, $\gamma_1 = 0.375$ and $\gamma_2 = -0.115$.

The performance of our algorithm for projecting merging galaxy clusters onto the PNC is visualised in Fig. 39. We show a random halo catalogue in the redshift range

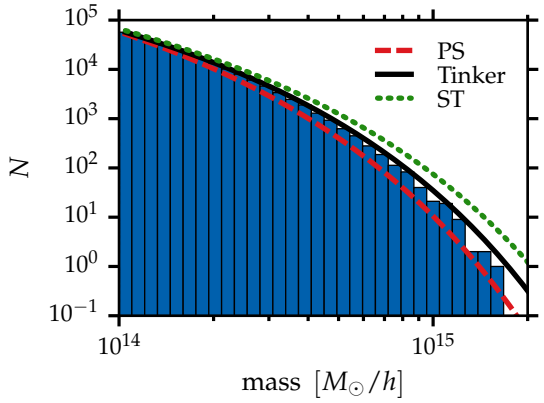

Figure 39: Comparison between a Monte-Carlo sampled halo catalogue in the redshift range $0.5 < z < 1.0$ (full sky) and the corresponding theoretically expected values of different halo mass functions. The random halo catalogue was generated with the merger tree algorithm of Parkinson et al. (2008). The red dashed, solid black, and green dotted curves indicate the mass functions proposed by Press & Schechter (1974) (PS), Tinker et al. (2008) (Tinker), and Sheth & Tormen (1999) (ST).

$0.5 < z < 1.0$ (full sky) that was generated with the PCH merger algorithm. As a reference, we also plot the theoretically expected values of the mass functions of Press-Schechter, Tinker, and Sheth-Tormen. The initial haloes at redshift $z = 0$ were drawn from the Tinker mass function. Figure 39 confirms that the sampled catalogue agrees well with the expectations of the Tinker mass function at the considered redshift range. Yet, even with the parameters from Benson (2008), the generated mass function falls slightly short of high-mass haloes. The deviation is only moderate, however, and to fix this problem, one would have to run large N-body simulations containing sufficiently many clusters with masses $M > 10^{15} M_\odot/h$ and re-fit the PCH algorithm. Clearly, this would go beyond the scope of the present work. For the following sections, it is only important to remember that the generated halo catalogues lack a few high-mass objects, which renders our estimates of the order statistics more conservative. Moreover, if one is only interested in haloes with redshifts $z \gg 0$, the problem of too few high-mass haloes can be mitigated by starting the merger tree simulations at higher initial redshifts, $z_{\rm ini} > 0$, because this decreases the interval over which the haloes have to be evolved backwards in time and hence also reduces the overestimated mass loss.

We cannot use an independent approach here to sample single haloes (without mergers) because the PCH algorithm does not exactly reproduce the Tinker mass function. Whenever we compute the statistics of Einstein radii neglecting cluster mergers, we simply take the catalogues generated by the merger algorithm instead and ignore the spatial correlations of the haloes, that is, we simply treat all haloes as isolated objects.

8.2.2 *Suggestions to reduce the computing time*

Increasing computational complexity is one main difficulty in estimating the order statistics of the largest Einstein radii including clusters mergers. As was shown in Sect. 6.2.2, about 10^3 mock universes have to be sampled for accurate fits of the GEV distribution. For each realisation, typically $\sim 10^6$ merger trees need to be simulated, and subsequently, their strong-lensing signals have to be evaluated. This whole procedure is computationally quite demanding. The computation of the results

presented in the following section, for instance, required approximately 2800 CPU hours on a large computing grid.

However, there are several steps that greatly reduce the required wall-clock time. Since future studies will probably face similar problems, it might be useful to list some of these steps here:

- *Mass thresholds*: As shown previously (and again verified for this chapter), only massive haloes contribute to the order statistics of the largest Einstein radii. We therefore only sample haloes with masses $M > 10^{14}\,M_\odot/h$ at the initial redshift. While simulating their merger trees, we discard all progenitors whose mass falls below $5 \times 10^{12}\,M_\odot/h$, because subhaloes at least need to exceed 5% of the main halo mass to notably perturb the Einstein radius (cf. Sect. 5.3).

  As described in Sect. 5.4.2, for each initial halo, our merger routine projects a list of progenitors onto the PNC. If the total mass of all progenitors falls below $10^{14}\,M_\odot/h$, we discard the system. Otherwise, we sort the progenitors in descending mass order, determine the Einstein radius of the most massive halo, and flag all progenitors that have been enclosed by the tangential critical curve. Next, we check if the total mass of the remaining unenclosed progenitors is larger than $10^{14}\,M_\odot/h$. If that is the case, we again sort them in descending mass order and compute the next Einstein radius. We repeat this procedure until no relevant unenclosed progenitors remain.

- *Maximum separation*: When computing the tangential critical curve that surrounds a certain progenitor, we only take the neighbouring haloes into account (superposition of deflection angles) whose distance is smaller than the sum of both virial radii, $d \leq (r_{\mathrm{vir},1} + r_{\mathrm{vir},2})$. Haloes that are farther away can safely be neglected because they do not notably perturb the lensing signal.

- *Einstein radius threshold*: From experience, we know that the n-th largest Einstein radius of a mock realisation will certainly be larger than a lower threshold $\theta_{\mathrm{eff}}^{\mathrm{min}}$. Then, prior to computing the detailed shape of the tangential critical curve of a lens system, we first quickly estimate the size of the resulting Einstein radius using the following steps:

  We loop over all relevant haloes in the field of view and treat them as isolated gravitational lenses. Because of their triaxial density profile, the projected surface mass density is ellipsoidal. We determine the major axis of the isodensity ellipses and compute the radius $\theta_{\mathrm{E}}^{\mathrm{est}}$ at which the tangential eigenvalue λ_{t} vanishes. A circle with radius $\theta_{\mathrm{E}}^{\mathrm{est}}$ encloses the full tangential critical curve of the halo and accordingly certainly over-estimates the real effective Einstein radius, $\theta_{\mathrm{eff}}^{\mathrm{est}} > \theta_{\mathrm{eff}}$.

  If the sum of all estimated Einstein radii (plus some tolerance) is smaller than the threshold $\theta_{\mathrm{E,eff}}^{\mathrm{min}}$, we can safely discard the system and skip the expensive detailed lensing computations.

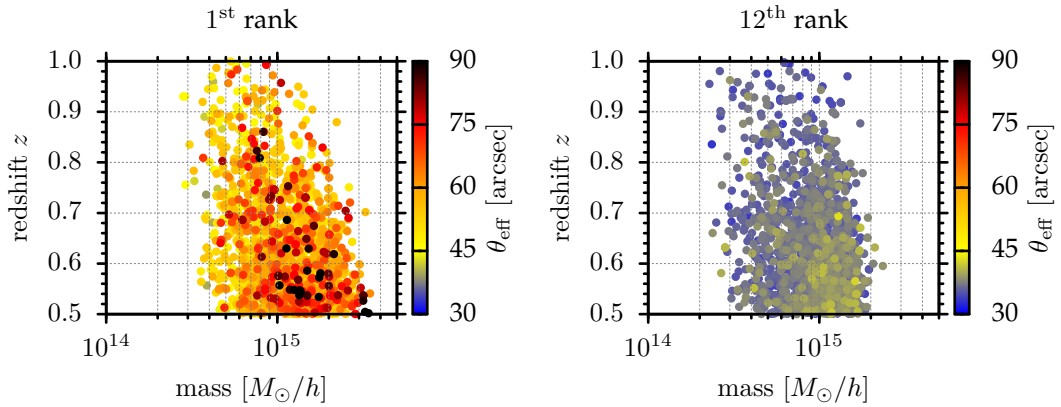

Figure 40: Mass and redshift distributions of the gravitational lenses that produce the largest and the twelfth-largest Einstein radius. The distributions were extracted from 2 000 mock realisations of Einstein radii in the redshift interval $0.5 \leq z \leq 1.0$ on the full sky. The calculations incorporated the impact of cluster mergers. The plotted mass denotes the total mass of all haloes enclosed by the corresponding tangential critical curves.

- *Shoelace formula*: The effective Einstein radius is derived from the area enclosed by the tangential critical curve. This area A can efficiently be computed using Stokes' theorem in two dimensions,

$$A = \int_A \mathrm{d}A = \int_A \mathrm{rot}\,\vec{v}\,\mathrm{d}A = \int_{\partial A} \vec{v}\,\mathrm{d}s\,, \tag{140}$$

  where $\vec{v}$ must be a vector field with $\mathrm{rot}\,\vec{v} = -\partial_y v_x + \partial_x v_y = 1$, such as $\vec{v} = 1/2\,(-y, x)^{\mathrm{T}}$. The calculation of the area thus reduces to a simple line integral, which is far cheaper than standard connected-component labelling algorithms. Practically, the line integral is implemented by means of a loop over all boundary points, summing up the contributions using the so-called shoelace formula.

- *Parallelisation*: The calculations can optimally (and trivially) be parallelised with OpenMP/MPI. The wall-clock time decreases inversely proportional to the number of CPUs used.

8.3 EXTREME VALUE AND ORDER STATISTICS WITH CLUSTER MERGERS

We now study the impact of cluster mergers on the order statistics of the largest Einstein radii in a certain cosmological volume. For comparison with the previous chapter, we exemplarily consider full-sky realisations of the cluster population in the redshift range $0.5 \leq z \leq 1.0$, which contains the twelve high-redshift ($z > 0.5$) MACS clusters analysed by Zitrin et al. (2011). In agreement with these authors, we assume a constant source redshift of $z_\mathrm{s} = 2.0$ throughout this chapter. We sampled 2 000 mock realisations of the cluster population and collected the largest Einstein radius of each run. These data allowed us to accurately estimate the order statistics of the twelve largest Einstein radii.

Figure 40 shows the mass and redshift distributions of the clusters that produce the largest and the twelfth-largest Einstein radius. Because our analysis also includes

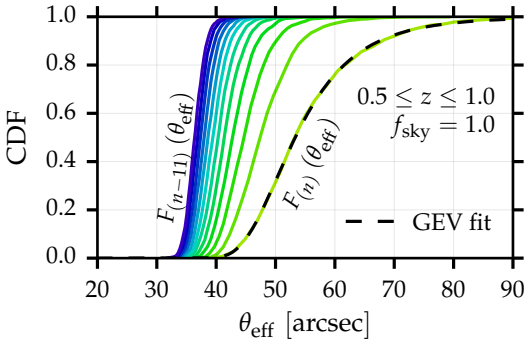

Figure 41: CDFs of the twelve largest Einstein radii, including the impact of cluster mergers. The black dashed curve indicates the fit of the GEV distribution to the CDF of the largest Einstein radius.

merging clusters, it is important to stress that the mass referred to in Fig. 40 is the total mass of all haloes enclosed by the corresponding tangential critical curves. Generally, we note that cluster mergers do not significantly alter the mass and redshift distributions of the strongest gravitational lenses. The plots shown here are almost identical to those presented in Sect. 7.3, which did not include the impact of cluster mergers. This is why we only show the plots of the first and the twelfth rank here. Most importantly, however, Fig. 40 confirms that the lower mass threshold of $M_{\rm min} = 10^{14}\,M_\odot/h$ discussed in Sect. 8.2.2 is well justified.

Figure 41 shows the CDFs of the twelve largest Einstein radii extracted from the 2 000 mock realisations sampled. While cluster mergers notably shift the CDFs to larger Einstein radii, the general characteristics discussed in Sect. 7.3 are conserved. The CDFs steepen with decreasing order, implying that lower orders are, in principle, more constraining. The black dashed line indicates the excellent fit of the GEV to the CDF of the 2 000 maxima sampled.

Next, we quantify the impact of cluster mergers on the GEV distribution of the largest Einstein radius. With mergers, the best-fitting parameters of the GEV distribution are given by $\alpha = (50.85 \pm 0.02)''$, $\beta = (6.61 \pm 0.03)''$, and $\gamma = (0.100 \pm 0.005)$. Excluding mergers, the best-fitting parameters are $\alpha = (45.88 \pm 0.02)''$, $\beta = (6.52 \pm 0.02)''$, and $\gamma(0.105 \pm 0.004)$. The CDFs and the PDFs of these distributions are compared in Fig. 42. In both cases, the shape parameters γ are positive, indicating that the GEV distributions are bounded from below. Most importantly, mergers increase the location parameter α by $\sim 5''$ ($\sim$11%), which means that the GEV distribution is significantly shifted to higher values. The mode of the GEV distribution (cf. Eq. (130))

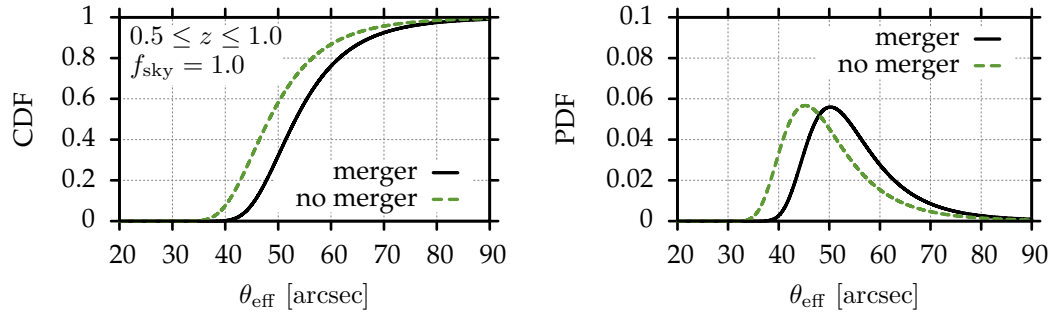

Figure 42: Impact of cluster mergers on the CDF and the PDF of the largest Einstein radius.

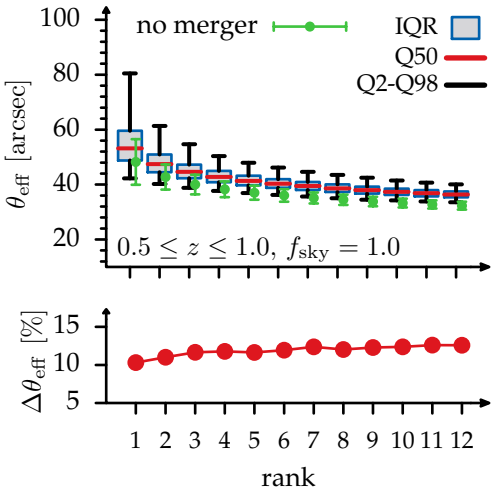

Figure 43: Box-and-whisker diagram comparing the order statistics of the twelve largest Einstein radii including and excluding cluster mergers. For each rank, in the upper plot the red lines indicate the median (Q50), the blue bordered grey boxes give the interquartile range (IQR), and the black whiskers mark the range between the 2 and 98 percentile (Q2, Q98) of the order statistics including the impact of cluster mergers. The green errors bars indicate the 68% confidence intervals of the order statistics excluding mergers. The lower plot shows the percentage increase of the medians caused by mergers.

increases from $45.2''$ without mergers to $50.2''$ with mergers. Similarly, the expectation value (cf. Eq. (131)) increases from $50.4''$ to $55.4''$.

The impact of cluster mergers on the order statistics of the twelve largest Einstein radii is summarised by the box-and-whisker diagram presented in Fig. 43. We chose this representation to simplify the comparison with the results of Chap. 7, but also because these diagrams compactly visualise important properties of statistical distributions. All medians of the twelve (six) highest orders are higher than $36''$ ($43''$), indicating that the ΛCDM model predicts a dozen Einstein radii as large as $\sim 35'' - 55''$ in the considered cosmological volume. If the 98 percentile was defined as exclusion criterion, one would need to observe approximately ten Einstein radii with $\theta_{\rm eff} \gtrsim 41''$, five with $\theta_{\rm eff} \gtrsim 48''$, or one large system with $\theta_{\rm eff} \gtrsim 80''$, to claim tension with the expectations of the ΛCDM model. Current observational data certainly do not exceed these expectations (Zitrin et al. 2011). Finally, the lower panel of Fig. 43 reveals that not only the expected value of the largest Einstein radius, but also those of the lower orders increase by $10 - 12\%$ because of the impact of cluster mergers.

In summary, the results of this section agree well with the findings of Chap. 5: cluster mergers are significant for the statistics of the strongest lenses. As a rule of thumb, mergers increase the expected values of the largest Einstein radii by ∼10%.

8.4 COMPARISON WITH OBSERVATIONAL DATA

8.4.1 *Galaxy cluster MACS J0717.5+3745*

As discussed in Chap. 6, the X-ray luminous galaxy cluster MACS J0717.5+3745 is a remarkable system: it is extremely massive, actively merging, and exhibits the largest known Einstein radius (Zitrin et al. 2009, 2011; Limousin et al. 2012). The cluster was re-observed as part of the Cluster Lensing And Supernova survey with Hubble (CLASH; Postman et al. 2012), a 524-orbit Hubble Space Telescope (HST) multi-cycle treasury program. Thereupon, Zitrin and collaborators revised their initial mass model from 2009 as published in Medezinski et al. (2013). The latest strong-lensing

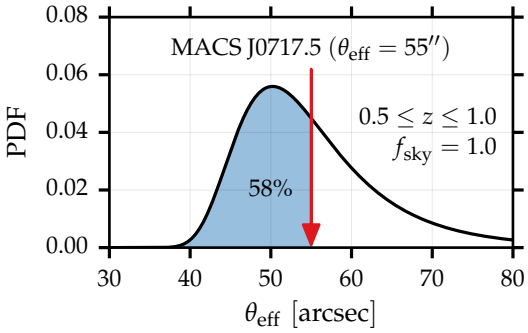

Figure 44: Comparison between the theoretically expected GEV distribution of the largest Einstein radius in the redshift range $0.5 \leq z \leq 1.0$ and the Einstein radius of the galaxy cluster MACS J0717.5+3745.

analysis of MACS J0717.5+3745 was conducted as part of the Hubble Frontier Fields program [1], yielding an Einstein radius of $\theta_{\mathrm{eff}} = (55 \pm 6)''$ for a source redshift $z_{\mathrm{s}} = 2.0$ (Zitrin et al., in preparation; private communication).

Although our case study in Sect. 6.4 already revealed that the Einstein radius of MACS J0717.5+3745 is not in tension with the expectations of the ΛCDM model, for completeness, we briefly update our results with the latest cosmological parameters from Planck (Planck Collaboration et al. 2013), and include the impact of cluster mergers. The cosmological volume analysed in the previous section was purposely chosen to contain the twelve MACS clusters discussed before. We can therefore use the best-fitting GEV parameters derived in Sect. 8.3.

Figure 44 shows that cluster mergers further confirm our main conclusion from Chap. 6: The large Einstein radius of MACS J0717.5+3745 clearly does not exceed the theoretical expectations of the ΛCDM model. In contrast, the probability for observing a maximum Einstein radius even larger than $55''$ amounts to ∼42%. Neglecting cluster mergers, this probability decreases to ∼24% (as can easily be verified by evaluating the GEV distribution with the best-fitting parameters given in Sect. 8.3). The 98 percentile of the GEV distribution is located at $\theta_{\mathrm{eff}} = 82''$, indicating that extraordinarily strong lenses would have to be observed to claim disagreement with the ΛCDM model. Interestingly, when cluster mergers are included, the Einstein radius of MACS J0717.5+3745 (accidentally) coincides with the expectation value $\theta_{\mathrm{eff}} = 55''$ of the theoretical GEV distribution (cf. Eq. (131)).

There is no need to revise the order statistics of the twelve MACS clusters discussed in Sect. 7.4, because we already showed that most Einstein radii of the lower orders lie below the theoretically expected values, even if cluster mergers are excluded. As indicated by Fig. 43, the inclusion of mergers would not add any new insight.

8.4.2 *SDSS clusters*

Hao et al. (2010) applied a cluster-finding algorithm to the Sloan Digital Sky Survey (SDSS) Data Release 7 (DR7) data (Abazajian et al. 2009) and assembled a large optical galaxy cluster catalogue consisting of over 55 000 rich clusters in the redshift range $0.1 \leq z \leq 0.55$. Zitrin et al. (2012) proposed a new method for performing a simplistic extrapolation of a strong-lensing analysis of these clusters in an automated way, and

1 http://www.stsci.edu/hst/campaigns/frontier-fields/

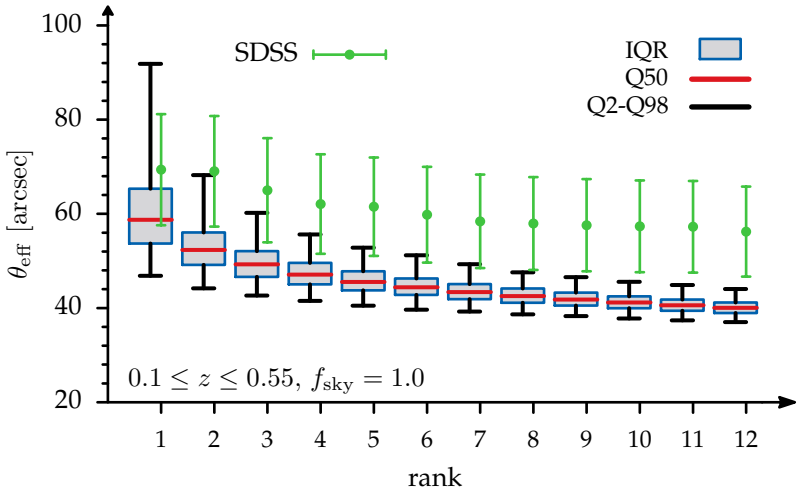

Figure 45: Box-and-whisker diagram comparing the theoretically expected order statistics of the twelve largest Einstein radii in the redshift range $0.1 \leq z \leq 0.55$ (full sky) and the largest Einstein radii in the SDSS sample analysed by Zitrin et al. (2012). For each rank, the red lines indicate the median (Q50), the blue bordered grey boxes give the interquartile range (IQR), and the black whiskers mark the range between the 2 and 98 percentile (Q2, Q98) of the order statistics. The green error bars indicate the estimated 68% confidence intervals of the Einstein radii in the SDSS sample.

Table 7: Comparison between the twelve largest Einstein radii in the SDSS sample analysed by Zitrin et al. (2012) and the theoretically expected order statistics for the redshift range $0.1 \leq z \leq 0.55$ (full sky). The error bounds of columns two and three indicate the 1σ confidence intervals. Q98 denotes the 98 percentile of the theoretical order statistics.

	SDSS	theory	
rank	$\theta_{\rm eff}$ [arcsec]	$\theta_{\rm eff}$ [arcsec]	Q98 [arcsec]
$1^{\rm st}$	69 ± 12	59 ± 9	92
$2^{\rm nd}$	69 ± 12	52 ± 5	68
$3^{\rm rd}$	65 ± 11	49 ± 4	60
$4^{\rm th}$	62 ± 10	47 ± 3	56
$5^{\rm th}$	62 ± 10	46 ± 3	53
$6^{\rm th}$	60 ± 10	44 ± 3	51
$7^{\rm th}$	58 ± 10	43 ± 2	49
$8^{\rm th}$	58 ± 10	43 ± 2	48
$9^{\rm th}$	58 ± 10	42 ± 2	47
$10^{\rm th}$	57 ± 10	41 ± 2	46
$11^{\rm th}$	57 ± 10	41 ± 2	45
$12^{\rm th}$	56 ± 10	40 ± 2	44

applied their technique to a subsample of 10 000 clusters to estimate their Einstein radii.

The method proposed by Zitrin et al. (2012) is based on the simple assumption that the light distribution observed in galaxy clusters generally traces their mass distribution well. The starting points are the red cluster member galaxies, which are assigned simple parametric mass profiles. The superposition of these individual profiles represents the galaxy component of the mass distribution. The dark matter component is constructed by smoothing the galaxies' distribution with a two-dimensional cubic spline interpolation. The sum of the two components serves as an indicator for the total projected matter density map of the cluster. The crucial point of the method is the calibration of the mass-to-light (M/L) ratio, which sets the normalisation of the projected surface mass density. Zitrin et al. (2012) calibrated this M/L ratio using a subsample of ten well-studied galaxy clusters that were covered by both high-quality HST images and the SDSS, and assumed that this calibration is (approximately) valid for the entire SDSS sample. Using this procedure, Zitrin and co-workers automatically (and blindly) processed the 10 000 SDSS clusters, derived simple lens models from the photometry of the cluster member galaxies and estimated the corresponding Einstein radii for sources at redshift $z_s = 2.0$.

To compare their results with the theoretically expected order statistics of the largest Einstein radii, we sampled 2 000 mock realisations of the redshift range $0.1 \leq z \leq 0.55$, assuming full sky coverage. Note that this choice was purposely too optimistic, because the SDSS DR7 only covered approximately one fourth of the full sky and, additionally, Zitrin et al. (2012) analysed only $\sim$20% of the discovered clusters to reduce the required computing time. Our theoretical estimates should therefore be expected to exceed the distribution of Einstein radii determined for the subsample of SDSS clusters.

However, Fig. 45 and Table 7 reveal exactly the opposite trend. The mean estimated Einstein radii extracted from the SDSS sample significantly exceed the expected values, and the difference increases with increasing rank. Starting with the second rank, the mean estimated Einstein radii even exceed the 98 percentiles of the theoretical distributions. On the other hand, the errors of the SDSS Einstein radii are still large. Zitrin et al. (2012) suggested to assume an uncertainty of at least $\sim$17% for the 1σ-boundary. From this point of view, all observed Einstein radii agree with the theoretically expected values within the 3σ confidence interval. However, we recall again that our theoretical estimates were computed for a substantially larger cosmological volume.

These results may imply that the observed lenses at low redshifts are somewhat stronger than theoretically expected, which would agree with the findings of Horesh et al. (2011), for example. Given the current state of the observational data, however, this conclusion would certainly be premature. The uncertainties of the method used by Zitrin et al. (2012) are still significant. Most importantly, the reliability of the assumed functional form for the M/L ratio needs to be verified and re-calibrated with a larger sample of well-studied lenses. Furthermore, Zitrin and co-workers mainly focused on the universal distribution of Einstein radii, instead of analysing the strongest lenses of their sample in detail (A. Zitrin, private communication).

More cautiously, we therefore conclude that the results of this section might indicate a discrepancy between theory and observations at low redshifts, and that it should certainly be interesting to carefully re-analyse the SDSS sample. Given the current state of the data and also the theoretical uncertainties influencing the modelling of the order statistics, there is, however, no reliable statistical evidence for claiming that these observations seriously challenge the predictions of the standard cosmological model.

8.5 CONCLUSIONS

In this chapter, we focused on the question whether or not the strongest observed gravitational lenses exceed the theoretical predictions of the standard cosmological model. We combined all previously developed techniques and calculated the impact of cluster mergers on the order statistics of the largest Einstein radii. Moreover, we compared the theoretical results with observational data at different redshifts.

In the first part of this chapter, we demonstrated that cluster mergers shift the GEV distribution of the largest Einstein radius to significantly higher values, typically increasing the location parameter and expected values by $\sim$10%. Furthermore, we showed that the order statistics of the n largest Einstein radii are also shifted by a similar amount. This confirmed our findings of Chap. 5, where we argued that cluster mergers are particularly important for the statistics of the strongest gravitational lenses.

In the second part of this chapter, we compared the order statistics of the largest Einstein radii, including the impact of cluster mergers, with recent observational data. As already shown in Chaps. 6 and 7, at redshifts $z > 0.5$, we see no evidence for a tension between the strength of observed gravitational lenses and the theoretical predictions of the ΛCDM model. On the contrary, we actually find that the largest known Einstein radius at redshifts $z > 0.5$, which was observed in the galaxy cluster MACS J0717.5+3745 (Zitrin et al. 2009, 2011; Limousin et al. 2012; Medezinski et al. 2013), agrees excellently well with the theoretical expectation value.

At redshifts $z < 0.5$, the situation is a little more controversial. We compared the largest Einstein radii of the 10 000 SDSS clusters analysed by Zitrin et al. (2012) to the theoretically expected order statistics, finding that the observed gravitational lenses in this redshift range appear to be stronger than expected. However, in this context, it is important to stress that the errors of the Einstein radii estimated for the SDSS sample are still large. Thus, given the premature state of current data, there is still no reliable statistical evidence for claiming disagreement with the ΛCDM model. Nevertheless, the SDSS sample might contain extraordinarily strong gravitational lenses, and it should certainly be interesting to carefully re-analyse these systems in future studies.

SUMMARY AND CONCLUSIONS

This thesis treated two largely different topics. In the first part, we employed radially inhomogeneous LTB models to probe the validity of the Copernican principle. In the second part, we investigated whether or not the strongest observed gravitational lenses exceed the maximum theoretical expectations of the ΛCDM model. Although we already presented detailed conclusions at the end of the individual chapters, we now try to summarise the most important results and provide a short outlook.

The line of reasoning of the first part can be summarised as follows: Current observational data, in particular the remarkable uniformity of the CMB spectrum, seem to confirm the fundamental assumption that the Universe is statistically isotropic about our position. In contrast, the assumption of spatial homogeneity on large scales is hard to confirm, mainly because it is difficult to disentangle a temporal from a spatial evolution along the PNC. Can we construct spherically symmetric, but radially inhomogeneous cosmologies that fit current data even more accurately than the standard cosmological model?

To this end, we first envisaged to live at the centre of a Gpc-scale LTB void whose matter density profile is tuned to fit current observational data. At first sight, these giant void scenarios appear very tempting because they are able to explain the apparent accelerated expansion of the Universe without resorting to any form of dark energy. On the other hand, these models obviously breach the Copernican principle, require radially fine-tuned matter density profiles, and are highly unlikely within the framework of the standard inflationary paradigm. Irrespective of these important (philosophical) issues, we showed that a quite general class of void models is ruled out by a very limited set of observational data. More precisely, we demonstrated that LTB models with constant bang time function and zero cosmological constant cannot simultaneously fit the small-angle CMB spectrum and the high local Hubble rate observed by Riess et al. (2011).

Several authors who found similar results proposed various extensions such as varying bang time functions that could help to reconcile the simplest LTB void models with current data (see e.g. Clarkson & Regis 2011; Nadathur & Sarkar 2011; Bull et al. 2012). However, we argued that we have fundamental objections against most modifications proposed, mainly because they eventually lead to even more fine-tuned, alternative cosmological models that would clearly be penalised by Ockham's razor in comparison with the much simpler ΛCDM model. In addition, according to Lovelock's remarkable theorems, the cosmological constant appears naturally in the field equations of general relativity and of any other metric theory of gravity, provided they satisfy very general simplicity conditions (Lovelock 1971, 1972). We thus argued that considering LTB models with non-zero cosmological constant seems to be the most natural extension of our approach. This is an interesting step because it shifts the research focus away from the dark energy problem to more general tests of the Copernican principle.

Based on this idea, we considered ΛLTB models with flexibly parametrised matter density profiles and used a Monte Carlo sampler in combination with recent observational data to systematically vary (and optimise) the shape of these profiles. Our analysis revealed that radially inhomogeneous models with fine-tuned matter density profiles do not noticeably improve the fit to the data. From a statistical point of view, the increased complexity of these models is not justified. Surprisingly, even without imposing any prior constraints on the detailed shape of the matter density profiles, the best-fitting ΛLTB models are almost perfectly homogeneous. Clearly, we could not find any statistical evidence for deviations from spatial homogeneity on the largest observable scales. On the contrary, we can conclude that the data considered in the first part of this thesis statistically favour the standard cosmological model and hence also provide (indirect) statistical support for the validity of the Copernican principle.

However, we also showed that more accurate constraints are required to ultimately confirm (or refute) the assumption of spatial homogeneity on the largest scales. Of course, future surveys containing more observational data will improve the situation. In this work, for instance, we used the Union2.1 compilation containing 580 type Ia supernovae to constrain ΛLTB models. New surveys such as the Dark Energy Survey (DES)[2] or the Large Synoptic Survey Telescope (LSST)[3] are expected to observe at least two orders of magnitude more supernovae up to redshifts $z \sim 1.2$ (Hook 2013). These data will impose much tighter constraints on the detailed shape of the luminosity distance and thus also help to constrain inhomogeneous cosmological models.

More importantly, however, we expect that the completion of our new numerical code for solving the linear perturbation equations on LTB backgrounds (Meyer et al., in preparation) will make a big difference. First, we intend to study the strength of the coupling between scalar, vectorial, and tensorial modes on LTB backgrounds with realistic cosmological initial conditions. If the coupling is sufficiently strong, it will be interesting to investigate whether this induces observable effects (e. g. a significant excitation of tensorial modes) which could help to quantify possible deviations from spatial homogeneity. Furthermore, we shall be able to extend our analysis of ΛLTB models by several observables that depend on the details of linear structure formation. This includes important cosmological probes such as cluster number counts, baryonic acoustic oscillations, or (tomographic) weak-lensing surveys (Schäfer & Heisenberg 2012; February et al. 2013). These observables contain a wealth of cosmological information and should certainly help to confirm (or refute) the Copernican principle.

In the second part of this thesis, we focused on the question whether or not the strongest observed gravitational lenses are in conflict with the concordance ΛCDM model. Our most important results of this part can be summarised as follows.

We showed that the theory of extreme value statistics provides a rigorous mathematical framework for studying the occurrence probability of the largest Einstein radius in a certain cosmological volume. In particular, the description in terms of the GEV distribution allows formulating exact ΛCDM exclusion criteria based on the largest observed Einstein radius in a concrete survey. However, inference based on a single observation is subject to several statistical peculiarities (e. g. statistical outliers)

2 http://www.darkenergysurvey.org
3 http://www.lsst.org

and might thus be dubious. Therefore, we argued that it is beneficial to extend our approach by considering the order statistics of the n largest Einstein radii, which allows formulating more robust ΛCDM exclusion criteria based on n observations instead of a single extreme event.

We developed fast, semi-analytic tools for forecasting the statistical strong-lensing properties of cosmological cluster populations. In particular, these tools allowed us to model the theoretically expected order statistics of the n largest Einstein radii in a predefined cosmological volume. While developing these methods, we demonstrated that cluster mergers are an important mechanism to substantially boost the lensing efficiency of the strongest lenses. For this reason, future semi-analytic studies inevitably need to take the impact of cluster mergers into account before questioning the validity of the ΛCDM model based on extreme strong-lensing events.

Furthermore, we found that the order statistics of the n largest Einstein radii is strongly influenced by a wide range of theoretical assumptions of the ΛCDM model. This property can both be interpreted as a strength and a weakness. It can be seen as a strength because it renders the order statistics a powerful cosmological probe that sensitively reacts to changes of the cosmological parameters (e. g. Ω_m and σ_8), certain details of structure formation (e. g. merger rates and halo mass function), and the internal properties of galaxy clusters (e. g. concentration and triaxiality). On the other hand, it can be seen as a weakness because due to this sensitivity, the order statistics is currently still subject to many theoretical uncertainties. Given the current state of the theory, it is certainly difficult to formulate reliable exclusion criteria that seriously challenge the underlying cosmological model.

There are, however, many details that can (and certainly will) be improved in future works. From a theoretical point of view, our analysis of the order statistics of the largest Einstein radii revealed that the following aspects of the semi-analytic modelling require substantial improvement: (1) the accuracy of the halo mass function, (2) the mass–concentration relation of massive clusters, and (3) the statistical description of triaxial dark matter haloes. In addition, we adopted a clearly simplistic picture of galaxy clusters, neglecting, for instance, substructures and the brightest cluster galaxies (BCG), both of which are known to further boost the strong-lensing efficiency (Meneghetti et al. 2013). At last, our simplistic model for the kinematics of cluster mergers could be improved by taking into account that (1) the major axes of infalling substructures are intrinsically aligned with the major axis of the main halo due to its tidal field, (2) subhaloes preferentially approach the main halo along its major axis (Lee et al. 2005; Altay et al. 2006; Zhang et al. 2009), and (3) impact parameters during cluster collisions are finite (Sarazin 2002).

From an observational point of view, it will be important to have homogeneous cluster surveys with well defined selection functions. Since we showed that the strongest gravitational lenses stem from a wide range in mass, it would be desirable to have surveys that not only observe the most massive galaxy clusters but ideally monitor complete samples of clusters with masses $M \gtrsim 10^{14}\,M_\odot/h$. Given current and upcoming surveys (e. g. DES, LSST, the Euclid satellite[4]; see Meneghetti et al.

4 http://www.euclid-ec.org

(2013) for a comprehensive review), we are optimistic that this can be achieved in the near future.

What can be said for sure is that (1) the discussion of the arc statistics problems and the Einstein ring problem certainly improved (and will improve) our understanding of cluster physics and structure formation, and (2) the statistics of strong-lensing events can be used as an important consistency check of the underlying cosmological model. Finally – and this is probably the most important result of the second part of this thesis – we can conclude that there is no statistical evidence at present for claiming that the largest observed Einstein radii exceed the theoretical expectations of the ΛCDM model.

Summarising both parts, we can conclude that the standard cosmological model successfully passed all statistical probes discussed in this thesis. From this point of view, the flat ΛCDM model remains a remarkable success. Nevertheless, we shall keep on questioning its foundations.

BIBLIOGRAPHY

Abazajian, K. N., Adelman-McCarthy, J. K., Agüeros, M. A., et al. (2009): *The Seventh Data Release of the Sloan Digital Sky Survey*. ApJS, **182**, 543

Ahnert, K. & Mulansky, M. (2011): *Odeint – Solving Ordinary Differential Equations in C++*. AIP Conference Proceedings, **1389** (1), 1586

Akaike, H. (1974): *A New Look at the Statistical Model Identification*. IEEE Transactions on Automatic Control, **19**, 716

Akeret, J., Seehars, S., Amara, A., Refregier, A., & Csillaghy, A. (2013): *CosmoHammer: Cosmological parameter estimation with the MCMC Hammer*. Astronomy and Computing, **2**, 27

Akima, H. (1970): *A New Method of Interpolation and Smooth Curve Fitting Based on Local Procedures*. J. ACM, **17** (4), 589

Alefeld, G. E., Potra, F. A., & Shi, Y. (1995): *Algorithm 748: Enclosing Zeros of Continuous Functions*. ACM Trans. Math. Softw., **21** (3), 327

Allison, R. & Dunkley, J. (2014): *Comparison of sampling techniques for Bayesian parameter estimation*. MNRAS, **437**, 3918

Alnes, H. & Amarzguioui, M. (2006): *CMB anisotropies seen by an off-center observer in a spherically symmetric inhomogeneous universe*. Phys. Rev. D, **74** (10), 103520

Altay, G., Colberg, J. M., & Croft, R. A. C. (2006): *The influence of large-scale structures on halo shapes and alignments*. MNRAS, **370**, 1422

Amanullah, R., Lidman, C., Rubin, D., et al. (2010): *Spectra and Hubble Space Telescope Light Curves of Six Type Ia Supernovae at 0.511 < z < 1.12 and the Union2 Compilation*. ApJ, **716**, 712

Amendola, L., Appleby, S., Bacon, D., et al. (2013): *Cosmology and Fundamental Physics with the Euclid Satellite*. Living Reviews in Relativity, **16**, 6

Amendola, L. & Tsujikawa, S., *Dark Energy: Theory and Observations* (Cambridge University Press, 2010)

Arnold, B. C., Balakrishnan, N., & Nagaraja, H. N., *A First Course in Order Statistics* (John Wiley & Sons, New York, 1992)

Audren, B. (2014): *Separate constraints on early and late cosmology*. MNRAS, **444**, 827

Audren, B., Lesgourgues, J., Benabed, K., & Prunet, S. (2013a): *Conservative constraints on early cosmology with MONTE PYTHON*. J. Cosmology Astropart. Phys., **2**, 001

Audren, B., Lesgourgues, J., Benabed, K., & Prunet, S. (2013b): *Monte Python: Monte Carlo Code for CLASS in Python*. Astrophysics Source Code Library

Baldi, M. & Pettorino, V. (2011): *High-z massive clusters as a test for dynamical coupled dark energy*. MNRAS, **412**, L1

Baltz, E. A., Marshall, P., & Oguri, M. (2009): *Analytic models of plausible gravitational lens potentials*. J. Cosmology Astropart. Phys., **1**, 15

Bartelmann, M. (2010a): *The dark Universe*. Reviews of Modern Physics, **82**, 331

Bartelmann, M. (2010b): *TOPICAL REVIEW Gravitational lensing*. Classical and Quantum Gravity, **27** (23), 233001

Bartelmann, M., Huss, A., Colberg, J. M., Jenkins, A., & Pearce, F. R. (1998): *Arc statistics with realistic cluster potentials. IV. Clusters in different cosmologies*. A&A, **330**, 1

Bennett, C. L., Larson, D., Weiland, J. L., et al. (2013): *Nine-year Wilkinson Microwave Anisotropy Probe (WMAP) Observations: Final Maps and Results*. ApJS, **208**, 20

Benson, A. J. (2008): *Constraining cold dark matter halo merger rates using the coagulation equations*. MNRAS, **388**, 1361

Bernardeau, F., Bonvin, C., & Vernizzi, F. (2010): *Full-sky lensing shear at second order*. Phys. Rev. D, **81** (8), 083002

Bertone, G., Hooper, D., & Silk, J. (2005): *Particle dark matter: evidence, candidates and constraints*. Phys. Rep., **405**, 279

Bhattacharya, S., Heitmann, K., White, M., et al. (2011): *Mass Function Predictions Beyond ΛCDM*. ApJ, **732**, 122

Biswas, T., Notari, A., & Valkenburg, W. (2010): *Testing the void against cosmological data: fitting CMB, BAO, SN and H_0*. J. Cosmology Astropart. Phys., **11**, 030

Bolejko, K. (2009): *The Szekeres Swiss Cheese model and the CMB observations*. General Relativity and Gravitation, **41**, 1737

Bolejko, K., Célérier, M.-N., & Krasiński, A. (2011): *Inhomogeneous cosmological models: exact solutions and their applications*. Classical and Quantum Gravity, **28** (16), 164002

Bolejko, K. & Wyithe, J. S. B. (2009): *Testing the copernican principle via cosmological observations*. J. Cosmology Astropart. Phys., **2**, 020

Bonafede, A., Feretti, L., Giovannini, G., et al. (2009): *Revealing the magnetic field in a distant galaxy cluster: discovery of the complex radio emission from MACS J0717.5 +3745*. A&A, **503**, 707

Bondi, H. (1947): *Spherically symmetrical models in general relativity*. MNRAS, **107**, 410

Bridle, S. L., Crittenden, R., Melchiorri, A., et al. (2002): *Analytic marginalization over CMB calibration and beam uncertainty*. MNRAS, **335**, 1193

Broadhurst, T. J. & Barkana, R. (2008): *Large Einstein radii: a problem for ΛCDM*. MNRAS, **390**, 1647

Brouzakis, N., Tetradis, N., & Tzavara, E. (2007): *The effect of large scale inhomogeneities on the luminosity distance*. J. Cosmology Astropart. Phys., **2**, 013

Bull, P., Clifton, T., & Ferreira, P. G. (2012): *Kinematic Sunyaev-Zel'dovich effect as a test of general radial inhomogeneity in Lemaître-Tolman-Bondi cosmology*. Phys. Rev. D, **85** (2), 024002

Carlson, B. (1995): *Numerical computation of real or complex elliptic integrals*. Numerical Algorithms, **10** (1), 13

Cayón, L., Gordon, C., & Silk, J. (2011): *Probability of the most massive cluster under non-Gaussian initial conditions*. MNRAS, **415**, 849

Célérier, M.-N. (2000): *Do we really see a cosmological constant in the supernovae data?* A&A, **353**, 63

Célérier, M.-N. (2012): *Some clarifications about Lemaître-Tolman models of the Universe used to deal with the dark energy problem*. A&A, **543**, A71

CÉLÉRIER, M.-N., BOLEJKO, K., & KRASIŃSKI, A. (2010): *A (giant) void is not mandatory to explain away dark energy with a Lemaître-Tolman model*. A&A, **518**, A21

CHONGCHITNAN, S. & SILK, J. (2012): *Primordial non-Gaussianity and extreme-value statistics of galaxy clusters*. Phys. Rev. D, **85** (6), 063508

CLARKSON, C. (2012): *Establishing homogeneity of the universe in the shadow of dark energy*. Comptes Rendus Physique, **13**, 682

CLARKSON, C., CLIFTON, T., & FEBRUARY, S. (2009): *Perturbation theory in Lemaître-Tolman-Bondi cosmology*. J. Cosmology Astropart. Phys., **6**, 025

CLARKSON, C., ELLIS, G. F. R., FALTENBACHER, A., ET AL. (2012): *(Mis)interpreting supernovae observations in a lumpy universe*. MNRAS, **426**, 1121

CLARKSON, C. & REGIS, M. (2011): *The cosmic microwave background in an inhomogeneous universe*. J. Cosmology Astropart. Phys., **2**, 013

CLIFTON, T., FERREIRA, P. G., & ZUNTZ, J. (2009): *What the small angle CMB really tells us about the curvature of the Universe*. J. Cosmology Astropart. Phys., **7**, 029

CLOWES, R. G., HARRIS, K. A., RAGHUNATHAN, S., ET AL. (2013): *A structure in the early Universe at z ˜1.3 that exceeds the homogeneity scale of the R-W concordance cosmology*. MNRAS, **429**, 2910

COLES, S., *An Introduction to Statistical Modeling of Extreme Values* (Springer, 2001)

CROCCE, M., FOSALBA, P., CASTANDER, F. J., & GAZTAÑAGA, E. (2010): *Simulating the Universe with MICE: the abundance of massive clusters*. MNRAS, **403**, 1353

DALAL, N., HOLDER, G., & HENNAWI, J. F. (2004): *Statistics of Giant Arcs in Galaxy Clusters*. ApJ, **609**, 50

DAVID, H. A. & NAGARAJA, H. N., *Order Statistics* (John Wiley & Sons, Hoboken, New Jersey, 2003)

DAVIS, O., DEVRIENDT, J., COLOMBI, S., SILK, J., & PICHON, C. (2011): *Most massive haloes with Gumbel statistics*. MNRAS, **413**, 2087

DUNSBY, P., GOHEER, N., OSANO, B., & UZAN, J.-P. (2010): *How close can an inhomogeneous universe mimic the concordance model?* J. Cosmology Astropart. Phys., **6**, 017

DURRER, R. & MAARTENS, R. (2008): *Dark energy and dark gravity: theory overview*. General Relativity and Gravitation, **40**, 301

EBELING, H., BARRETT, E., & DONOVAN, D. (2004): *Discovery of a Large-Scale Filament Connected to the Massive Galaxy Cluster MACS J0717.5+3745 at z=0.551,*. ApJ, **609**, L49

EBELING, H., BARRETT, E., DONOVAN, D., ET AL. (2007): *A Complete Sample of 12 Very X-Ray Luminous Galaxy Clusters at z > 0.5*. ApJ, **661**, L33

EBELING, H., EDGE, A. C., & HENRY, J. P. (2001): *MACS: A Quest for the Most Massive Galaxy Clusters in the Universe*. ApJ, **553**, 668

EDGE, A. C., EBELING, H., BREMER, M., ET AL. (2003): *The discovery of two distant, massive clusters of galaxies in the ROSAT All-Sky Survey*. MNRAS, **339**, 913

EFSTATHIOU, G. (2014): *H_0 revisited*. MNRAS, **440**, 1138

EINASTO, M., LIIVAMÄGI, L. J., TAGO, E., ET AL. (2011a): *SDSS DR7 superclusters. Morphology*. A&A, **532**, A5

EINASTO, M., LIIVAMÄGI, L. J., TEMPEL, E., ET AL. (2011b): *The Sloan Great Wall. Morphology and Galaxy Content*. ApJ, **736**, 51

Einstein, A. (1915): *Die Feldgleichungen der Gravitation*. Sitzungsberichte der Königlich Preußischen Akademie der Wissenschaften (Berlin), Seite 844-847., 844–847

Ellis, G. F. R. (2009): *Republication of: Relativistic cosmology*. General Relativity and Gravitation, **41**, 581

Enqvist, K. (2008): *Lemaitre Tolman Bondi model and accelerating expansion*. General Relativity and Gravitation, **40**, 451

Enqvist, K. & Mattsson, T. (2007): *The effect of inhomogeneous expansion on the supernova observations*. J. Cosmology Astropart. Phys., **2**, 019

Etherington, I. M. H. (1933): *On the Definition of Distance in General Relativity.* Philosophical Magazine, **15**, 761

Etherington, I. M. H. (2007): *Republication of: LX. On the definition of distance in general relativity*. General Relativity and Gravitation, **39**, 1055

Fanizza, G. & Nugier, F. (2014): *Lensing in the Geodesic Light-Cone coordinates and its exact application to an off-center observer in LTB models*. arXiv:1408.1604

February, S., Clarkson, C., & Maartens, R. (2013): *Galaxy correlations and the BAO in a void universe: structure formation as a test of the Copernican Principle*. J. Cosmology Astropart. Phys., **3**, 023

February, S., Larena, J., Clarkson, C., & Pollney, D. (2014): *Evolution of linear perturbations in spherically symmetric dust spacetimes*. Classical and Quantum Gravity, **31** (17), 175008

Fedeli, C. & Bartelmann, M. (2007): *Effects of early dark energy on strong cluster lensing*. A&A, **461**, 49

Fedeli, C., Meneghetti, M., Bartelmann, M., Dolag, K., & Moscardini, L. (2006): *A fast method for computing strong-lensing cross sections: application to merging clusters.* A&A, **447**, 419

Fisher, R. & Tippett, L. (1928): *Limiting Forms of the Frequency Distribution of the Largest or Smallest Member of a Sample.* Proc. Cambridge Phil. Soc., **24**, 180

Foley, R. J., Andersson, K., Bazin, G., et al. (2011): *Discovery and Cosmological Implications of SPT-CL J2106-5844, the Most Massive Known Cluster at z > 1.* ApJ, **731**, 86

Foreman, S., Moss, A., Zibin, J. P., & Scott, D. (2010): *Spatial and temporal tuning in void models for acceleration*. Phys. Rev. D, **82** (10), 103532

Foreman-Mackey, D., Hogg, D. W., Lang, D., & Goodman, J. (2013): *emcee: The MCMC Hammer*. PASP, **125**, 306

Friedmann, A. (1922): *Über die Krümmung des Raumes*. Zeitschrift fur Physik, **10**, 377

Garcia-Bellido, J. & Haugbølle, T. (2008): *Confronting Lemaitre Tolman Bondi models with observational cosmology*. J. Cosmology Astropart. Phys., **4**, 003

García-Bellido, J. & Haugbølle, T. (2008): *Looking the void in the eyes – the kinematic Sunyaev Zeldovich effect in Lemaître Tolman Bondi models*. J. Cosmology Astropart. Phys., **9**, 016

Giocoli, C., Meneghetti, M., Bartelmann, M., Moscardini, L., & Boldrin, M. (2012): *MOKA: a new tool for strong lensing studies*. MNRAS, **421**, 3343

Gnedenko, B. (1943): *Sur la distribution limite du terme maximum d'une serie aleatoire*. Ann. Math., **44**, 423

Goodman, J. & Weare, J. (2010): *Ensemble Samplers with Affine Invariance*. Communications in Applied Mathematics and Computational Science, **5** (1), 65

GOTTLÖBER, S. & YEPES, G. (2007): *Shape, Spin, and Baryon Fraction of Clusters in the MareNostrum Universe*. ApJ, **664**, 117

GREEN, S. R. & WALD, R. M. (2012): *Newtonian and relativistic cosmologies*. Phys. Rev. D, **85** (6), 063512

GUMBEL, E. (1958): *Statistics of extremes, 1958*. Columbia Univ. press, New York

GUY, J., ASTIER, P., BAUMONT, S., ET AL. (2007): *SALT2: using distant supernovae to improve the use of type Ia supernovae as distance indicators*. A&A, **466**, 11

HAAR, A. (1933): *Der Massbegriff in der Theorie der Kontinuierlichen Gruppen*. The Annals of Mathematics, **34** (1), 147

HALKOLA, A., HILDEBRANDT, H., SCHRABBACK, T., ET AL. (2008): *The mass distribution of RX J1347-1145 from strong lensing*. A&A, **481**, 65

HAO, J., MCKAY, T. A., KOESTER, B. P., ET AL. (2010): *A GMBCG Galaxy Cluster Catalog of 55,424 Rich Clusters from SDSS DR7*. ApJS, **191**, 254

HASTINGS, W. K. (1970): *Monte Carlo sampling methods using Markov chains and their applications*. Biometrika, **57** (1), 97

HELLABY, C. & KRASIŃSKI, A. (2006): *Alternative methods of describing structure formation in the Lemaitre-Tolman model*. Phys. Rev. D, **73** (2), 023518

HELLABY, C. & LAKE, K. (1985): *Shell crossings and the Tolman model*. ApJ, **290**, 381

HICKEN, M., WOOD-VASEY, W. M., BLONDIN, S., ET AL. (2009): *Improved Dark Energy Constraints from ˜100 New CfA Supernova Type Ia Light Curves*. ApJ, **700**, 1097

HOGG, D. W., EISENSTEIN, D. J., BLANTON, M. R., ET AL. (2005): *Cosmic Homogeneity Demonstrated with Luminous Red Galaxies*. ApJ, **624**, 54

HOLZ, D. E. & PERLMUTTER, S. (2012): *The Most Massive Objects in the Universe*. ApJ, **755**, L36

HOOK, I. M. (2013): *Supernovae and cosmology with future European facilities*. Royal Society of London Philosophical Transactions Series A, **371**, 20282

HORESH, A., MAOZ, D., HILBERT, S., & BARTELMANN, M. (2011): *Lensed arc statistics: comparison of Millennium simulation galaxy clusters to Hubble Space Telescope observations of an X-ray selected sample*. MNRAS, **418**, 54

HOTCHKISS, S. (2011): *Quantifying the rareness of extreme galaxy clusters*. J. Cosmology Astropart. Phys., **7**, 4

HU, W. & SUGIYAMA, N. (1996): *Small-Scale Cosmological Perturbations: an Analytic Approach*. ApJ, **471**, 542

JEE, M. J., ROSATI, P., FORD, H. C., ET AL. (2009): *Hubble Space Telescope Weak-lensing Study of the Galaxy Cluster XMMU J2235.3 - 2557 at z ˜ 1.4: A Surprisingly Massive Galaxy Cluster When the Universe is One-third of its Current Age*. ApJ, **704**, 672

JENKINS, A., FRENK, C. S., WHITE, S. D. M., ET AL. (2001): *The mass function of dark matter haloes*. MNRAS, **321**, 372

JENKINSON, A. F. (1955): *The frequency distribution of the annual maximum (or minimum) values of metereological events*. Quarterly Journal of the Royal Metereological Society, **81**, 158

JIANG, F. & VAN DEN BOSCH, F. C. (2014): *Generating merger trees for dark matter haloes: a comparison of methods*. MNRAS, **440**, 193

Jing, Y. P. & Suto, Y. (2000): *The Density Profiles of the Dark Matter Halo Are Not Universal*. ApJ, **529**, L69

Jing, Y. P. & Suto, Y. (2002): *Triaxial Modeling of Halo Density Profiles with High-Resolution N-Body Simulations*. ApJ, **574**, 538

Keeton, C. R. & Madau, P. (2001): *Lensing Constraints on the Cores of Massive Dark Matter Halos*. ApJ, **549**, L25

Kessler, R., Becker, A. C., Cinabro, D., et al. (2009): *First-Year Sloan Digital Sky Survey-II Supernova Results: Hubble Diagram and Cosmological Parameters*. ApJS, **185**, 32

Komatsu, E., Smith, K. M., Dunkley, J., et al. (2011): *Seven-year Wilkinson Microwave Anisotropy Probe (WMAP) Observations: Cosmological Interpretation*. ApJS, **192**, 18

Kotz, S. & Nadarajah, S., *Extreme Value Distributions - Theory and Applications* (Imperial College Press, London, 2000)

Krasiński, A. (2014): *Accelerating expansion or inhomogeneity? A comparison of the ΛCDM and Lemaître-Tolman models*. Phys. Rev. D, **89** (2), 023520

Krasiński, A. & Hellaby, C. (2002): *Structure formation in the Lemaître-Tolman model*. Phys. Rev. D, **65** (2), 023501

Labini, F. S., *Characterizing the large scale inhomogeneity of the galaxy distribution*. In J.-M. Alimi & A. Fuözfa, eds., *American Institute of Physics Conference Series*, volume 1241 of *American Institute of Physics Conference Series*, 981–990 (2010)

Labini, F. S. (2011): *Inhomogeneities in the universe*. Classical and Quantum Gravity, **28** (16), 164003

Lacey, C. & Cole, S. (1993): *Merger rates in hierarchical models of galaxy formation*. MNRAS, **262**, 627

LaRoque, S. J., Joy, M., Carlstrom, J. E., et al. (2003): *Sunyaev-Zeldovich Effect Imaging of MACS Galaxy Clusters at z > 0.5*. ApJ, **583**, 559

Larson, D., Dunkley, J., Hinshaw, G., et al. (2011): *Seven-year Wilkinson Microwave Anisotropy Probe (WMAP) Observations: Power Spectra and WMAP-derived Parameters*. ApJS, **192**, 16

Lee, J., Kang, X., & Jing, Y. P. (2005): *The Intrinsic Alignment of Dark Halo Substructures*. ApJ, **629**, L5

Lemaître, G. (1927): *Un Univers homogène de masse constante et de rayon croissant rendant compte de la vitesse radiale des nébuleuses extra-galactiques*. Annales de la Societe Scietifique de Bruxelles, **47**, 49

Lemaître, G. (1933): *L'Univers en expansion*. Annales de la Societe Scietifique de Bruxelles, **53**, 51

Lesgourgues, J. (2011): *The Cosmic Linear Anisotropy Solving System (CLASS) I: Overview*. arXiv:1104.2932

Lewis, A., Challinor, A., & Lasenby, A. (2000): *Efficient Computation of Cosmic Microwave Background Anisotropies in Closed Friedmann-Robertson-Walker Models*. ApJ, **538**, 473

Limousin, M., Ebeling, H., Richard, J., et al. (2012): *Strong lensing by a node of the cosmic web. The core of MACS J0717.5+3745 at z = 0.55*. A&A, **544**, A71

Limousin, M., Richard, J., Kneib, J.-P., et al. (2008): *Strong lensing in Abell 1703: constraints on the slope of the inner dark matter distribution*. A&A, **489**, 23

LOVELOCK, D. (1971): *The Einstein Tensor and Its Generalizations*. Journal of Mathematical Physics, **12**, 498

LOVELOCK, D. (1972): *The Four-Dimensionality of Space and the Einstein Tensor*. Journal of Mathematical Physics, **13**, 874

MA, C.-J., EBELING, H., DONOVAN, D., & BARRETT, E. (2008): *The Spatial Distribution of Galaxies of Different Spectral Types in the Massive Intermediate-Redshift Cluster MACS J0717.5+3745*. ApJ, **684**, 160

MAARTENS, R. (2011): *Is the Universe homogeneous?* Royal Society of London Philosophical Transactions Series A, **369**, 5115

MARRA, V., AMENDOLA, L., SAWICKI, I., & VALKENBURG, W. (2013a): *Cosmic Variance and the Measurement of the Local Hubble Parameter*. Physical Review Letters, **110** (24), 241305

MARRA, V. & NOTARI, A. (2011): *Observational constraints on inhomogeneous cosmological models without dark energy*. Classical and Quantum Gravity, **28** (16), 164004

MARRA, V. & PÄÄKKÖNEN, M. (2010): *Observational constraints on the ΛLTB model*. J. Cosmology Astropart. Phys., **12**, 021

MARRA, V., PÄÄKKÖNEN, M., & VALKENBURG, W. (2013b): *Uncertainty on w from large-scale structure*. MNRAS, **431**, 1891

MARRIAGE, T. A., ACQUAVIVA, V., ADE, P. A. R., ET AL. (2011): *The Atacama Cosmology Telescope: Sunyaev-Zel'dovich-Selected Galaxy Clusters at 148 GHz in the 2008 Survey*. ApJ, **737**, 61

MEDEZINSKI, E., UMETSU, K., NONINO, M., ET AL. (2013): *CLASH: Complete Lensing Analysis of the Largest Cosmic Lens MACS J0717.5+3745 and Surrounding Structures*. ApJ, **777**, 43

MELCHIOR, P., SUTTER, P. M., SHELDON, E. S., KRAUSE, E., & WANDELT, B. D. (2014): *First measurement of gravitational lensing by cosmic voids in SDSS*. MNRAS, **440**, 2922

MENANTEAU, F., HUGHES, J. P., SIFÓN, C., ET AL. (2012): *The Atacama Cosmology Telescope: ACT-CL J0102-4915 "El Gordo," a Massive Merging Cluster at Redshift 0.87*. ApJ, **748**, 7

MENEGHETTI, M., ARGAZZI, R., PACE, F., ET AL. (2007): *Arc sensitivity to cluster ellipticity, asymmetries, and substructures*. A&A, **461**, 25

MENEGHETTI, M., BARTELMANN, M., DAHLE, H., & LIMOUSIN, M. (2013): *Arc Statistics*. Space Sci. Rev., **177**, 31

MENEGHETTI, M., FEDELI, C., PACE, F., GOTTLÖBER, S., & YEPES, G. (2010): *Strong lensing in the MARENOSTRUM UNIVERSE. I. Biases in the cluster lens population*. A&A, **519**, A90

MENEGHETTI, M., FEDELI, C., ZITRIN, A., ET AL. (2011): *Comparison of an X-ray-selected sample of massive lensing clusters with the MareNostrum Universe ΛCDM simulation*. A&A, **530**, A17

MOORE, B., QUINN, T., GOVERNATO, F., STADEL, J., & LAKE, G. (1999): *Cold collapse and the core catastrophe*. MNRAS, **310**, 1147

MORTONSON, M. J., HU, W., & HUTERER, D. (2011): *Simultaneous falsification of ΛCDM and quintessence with massive, distant clusters*. Phys. Rev. D, **83** (2), 023015

MOSS, A., ZIBIN, J. P., & SCOTT, D. (2011): *Precision cosmology defeats void models for acceleration*. Phys. Rev. D, **83** (10), 103515

MROCZKOWSKI, T., DICKER, S., SAYERS, J., ET AL. (2012): *A Multi-wavelength Study of the Sunyaev-Zel'dovich Effect in the Triple-merger Cluster MACS J0717.5+3745 with MUSTANG and Bolocam*. ApJ, **761**, 47

Mullis, C. R., Rosati, P., Lamer, G., et al. (2005): *Discovery of an X-Ray-luminous Galaxy Cluster at z=1.4*. ApJ, **623**, L85

Nadathur, S. (2013): *Seeing patterns in noise: gigaparsec-scale 'structures' that do not violate homogeneity*. MNRAS, **434**, 398

Nadathur, S. & Hotchkiss, S. (2014): *A robust public catalogue of voids and superclusters in the SDSS Data Release 7 galaxy surveys*. MNRAS, **440**, 1248

Nadathur, S. & Sarkar, S. (2011): *Reconciling the local void with the CMB*. Phys. Rev. D, **83** (6), 063506

Nakamura, T. T. & Suto, Y. (1997): *Strong Gravitational Lensing and Velocity Function as Tools to Probe Cosmological Parameters — Current Constraints and Future Predictions —*. Progress of Theoretical Physics, **97**, 49

Narayan, R. & Bartelmann, M. (1996): *Lectures on Gravitational Lensing*. ArXiv Astrophysics e-prints

Nariai, H. (1950): *On some static solutions of Einstein's gravitational field equations in a spherically symmetric case*. Sci. Rep. Tohoku Univ. Eighth Ser., **34**, 160

Navarro, J. F., Frenk, C. S., & White, S. D. M. (1996): *The Structure of Cold Dark Matter Halos*. ApJ, **462**, 563

Navarro, J. F., Hayashi, E., Power, C., et al. (2004): *The inner structure of ΛCDM haloes - III. Universality and asymptotic slopes*. MNRAS, **349**, 1039

Newman, A. B., Treu, T., Ellis, R. S., & Sand, D. J. (2011): *The Dark Matter Distribution in A383: Evidence for a Shallow Density Cusp from Improved Lensing, Stellar Kinematic, and X-ray Data*. ApJ, **728**, L39

Oguri, M. (2004): *Strong Gravitational Lenses in a Cold Dark Matter Universe*. Ph.D. thesis, The University of Tokyo

Oguri, M. & Blandford, R. D. (2009): *What is the largest Einstein radius in the universe?* MNRAS, **392**, 930

Oguri, M. & Keeton, C. R. (2004): *Effects of Triaxiality on the Statistics of Large-Separation Gravitational Lenses*. ApJ, **610**, 663

Oguri, M., Lee, J., & Suto, Y. (2003): *Arc Statistics in Triaxial Dark Matter Halos: Testing the Collisionless Cold Dark Matter Paradigm*. ApJ, **599**, 7

Parkinson, H., Cole, S., & Helly, J. (2008): *Generating dark matter halo merger trees*. MNRAS, **383**, 557

Peebles, P. J. & Ratra, B. (2003): *The cosmological constant and dark energy*. Reviews of Modern Physics, **75**, 559

Perlmutter, S., Aldering, G., Goldhaber, G., et al. (1999): *Measurements of Omega and Lambda from 42 High-Redshift Supernovae*. ApJ, **517**, 565

Pickands, J. (1975): *Statistical inference using extreme order statistics*. Annals of Statistics, **3**, 119

Planck Collaboration, Ade, P. A. R., Aghanim, N., et al. (2013): *Planck 2013 results. XVI. Cosmological parameters*. arXiv:1303.5076

Plebański, J. & Krasiński, A., *An Introduction to General Relativity and Cosmology* (Cambridge University Press, 2006)

POSTMAN, M., COE, D., BENÍTEZ, N., ET AL. (2012): *The Cluster Lensing and Supernova Survey with Hubble: An Overview*. ApJS, **199**, 25

POWER, C., NAVARRO, J. F., JENKINS, A., ET AL. (2003): *The inner structure of ΛCDM haloes - I. A numerical convergence study*. MNRAS, **338**, 14

PRESS, W., *Numerical Recipes 3rd Edition: The Art of Scientific Computing* (Cambridge University Press, 2007)

PRESS, W. H. & SCHECHTER, P. (1974): *Formation of Galaxies and Clusters of Galaxies by Self-Similar Gravitational Condensation*. ApJ, **187**, 425

PUCHWEIN, E., BARTELMANN, M., DOLAG, K., & MENEGHETTI, M. (2005): *The impact of gas physics on strong cluster lensing*. A&A, **442**, 405

PULLEN, A. R. & HIRATA, C. M. (2010): *Non-detection of a statistically anisotropic power spectrum in large-scale structure*. J. Cosmology Astropart. Phys., **5**, 027

RAYCHAUDHURI, A. (1955): *Relativistic Cosmology. I.* Physical Review, **98**, 1123

REDLICH, M., BARTELMANN, M., WAIZMANN, J.-C., & FEDELI, C. (2012): *The strongest gravitational lenses. I. The statistical impact of cluster mergers*. A&A, **547**, A66

REDLICH, M., BOLEJKO, K., MEYER, S., LEWIS, G. F., & BARTELMANN, M. (2014a): *Probing spatial homogeneity with LTB models: a detailed discussion*. A&A, **in press**. DOI: 10.1051/0004-6361/201424553

REDLICH, M., WAIZMANN, J.-C., & BARTELMANN, M. (2014b): *The strongest gravitational lenses: IV. The order statistics of the largest Einstein radii with cluster mergers*. A&A, **569**, A34

REISS, R.-D. & THOMAS, M., *Statistical Analysis of Extreme Values, 3rd ed.* (Birkhauser Verlag, Basel, 2007)

RIESS, A. G., FILIPPENKO, A. V., CHALLIS, P., ET AL. (1998): *Observational Evidence from Supernovae for an Accelerating Universe and a Cosmological Constant*. AJ, **116**, 1009

RIESS, A. G., MACRI, L., CASERTANO, S., ET AL. (2011): *A 3% Solution: Determination of the Hubble Constant with the Hubble Space Telescope and Wide Field Camera 3*. ApJ, **730**, 119

ROBERTSON, H. P. (1935): *Kinematics and World-Structure*. ApJ, **82**, 284

ROSATI, P., TOZZI, P., GOBAT, R., ET AL. (2009): *Multi-wavelength study of XMMU J2235.3-2557: the most massive galaxy cluster at z > 1*. A&A, **508**, 583

SACHS, R. (1961): *Gravitational Waves in General Relativity. VI. The Outgoing Radiation Condition*. Royal Society of London Proceedings Series A, **264**, 309

SARAZIN, C. L., *The Physics of Cluster Mergers*. In L. Feretti, I. M. Gioia, & G. Giovannini, eds., *Merging Processes in Galaxy Clusters*, volume 272 of *Astrophysics and Space Science Library*, 1–38 (2002)

SARKAR, P., YADAV, J., PANDEY, B., & BHARADWAJ, S. (2009): *The scale of homogeneity of the galaxy distribution in SDSS DR6*. MNRAS, **399**, L128

SCHÄFER, B. M. & HEISENBERG, L. (2012): *Weak lensing tomography with orthogonal polynomials*. MNRAS, **423**, 3445

SCHÄFER, B. M., HEISENBERG, L., KALOVIDOURIS, A. F., & BACON, D. J. (2012): *On the validity of the Born approximation for weak cosmic flexions*. MNRAS, **420**, 455

SCHNEIDER, P., EHLERS, J., & FALCO, E. E., *Gravitational Lenses* (Springer, 1992)

SCHRAMM, T. (1990): *Realistic elliptical potential wells for gravitational lens models*. A&A, **231**, 19

Schwarz, G. (1978): *Estimating the Dimension of a Model*. The Annals of Statistics, **6** (2), 461

Scrimgeour, M. I., Davis, T., Blake, C., et al. (2012): *The WiggleZ Dark Energy Survey: the transition to large-scale cosmic homogeneity*. MNRAS, **425**, 116

Sheth, R. K. & Tormen, G. (1999): *Large-scale bias and the peak background split*. MNRAS, **308**, 119

Sheth, R. K. & Tormen, G. (2002): *An excursion set model of hierarchical clustering: ellipsoidal collapse and the moving barrier*. MNRAS, **329**, 61

Silk, J. (1977): *Large-scale inhomogeneity of the Universe - Spherically symmetric models*. A&A, **59**, 53

Smale, P. R. & Wiltshire, D. L. (2011): *Supernova tests of the timescape cosmology*. MNRAS, **413**, 367

Springel, V., White, S. D. M., Jenkins, A., et al. (2005): *Simulations of the formation, evolution and clustering of galaxies and quasars*. Nature, **435**, 629

Straumann, N., *General relativity with applications to astrophysics* (Springer, 2004)

Sunyaev, R. A. & Zeldovich, I. B. (1980): *The velocity of clusters of galaxies relative to the microwave background - The possibility of its measurement*. MNRAS, **190**, 413

Sunyaev, R. A. & Zeldovich, Y. B. (1970): *Small-Scale Fluctuations of Relic Radiation*. Ap&SS, **7**, 3

Sunyaev, R. A. & Zeldovich, Y. B. (1972): *The Observations of Relic Radiation as a Test of the Nature of X-Ray Radiation from the Clusters of Galaxies*. Comments on Astrophysics and Space Physics, **4**, 173

Sutter, P. M., Lavaux, G., Wandelt, B. D., et al. (2014): *Voids in the SDSS DR9: observations, simulations, and the impact of the survey mask*. MNRAS, **442**, 3127

Suzuki, N., Rubin, D., Lidman, C., et al. (2012): *The Hubble Space Telescope Cluster Supernova Survey. V. Improving the Dark-energy Constraints above z > 1 and Building an Early-type-hosted Supernova Sample*. ApJ, **746**, 85

Tinker, J., Kravtsov, A. V., Klypin, A., et al. (2008): *Toward a Halo Mass Function for Precision Cosmology: The Limits of Universality*. ApJ, **688**, 709

Tolman, R. C. (1934): *Effect of Inhomogeneity on Cosmological Models*. Proceedings of the National Academy of Science, **20**, 169

Torri, E., Meneghetti, M., Bartelmann, M., et al. (2004): *The impact of cluster mergers on arc statistics*. MNRAS, **349**, 476

Umetsu, K. & Broadhurst, T. (2008): *Combining Lens Distortion and Depletion to Map the Mass Distribution of A1689*. ApJ, **684**, 177

Valkenburg, W. (2012): *Complete solutions to the metric of spherically collapsing dust in an expanding spacetime with a cosmological constant*. General Relativity and Gravitation, **44**, 2449

Valkenburg, W., Marra, V., & Clarkson, C. (2014): *Testing the Copernican principle by constraining spatial homogeneity*. MNRAS, **438**, L6

von Mises, R. (1954): *La distribution de la plus grande de n valuers.* Americ. Math. Soc, **Volume II**, 271

Vonlanthen, M., Räsänen, S., & Durrer, R. (2010): *Model-independent cosmological constraints from the CMB*. J. Cosmology Astropart. Phys., **8**, 023

WAIZMANN, J.-C., ETTORI, S., & BARTELMANN, M. (2013): *Order statistics applied to the most massive and most distant galaxy clusters*. MNRAS, **432**, 914

WAIZMANN, J.-C., ETTORI, S., & MOSCARDINI, L. (2011): *On a novel approach using massive clusters at high redshifts as cosmological probe*. MNRAS, **418**, 456

WAIZMANN, J.-C., ETTORI, S., & MOSCARDINI, L. (2012a): *An application of extreme value statistics to the most massive galaxy clusters at low and high redshifts*. MNRAS, **420**, 1754

WAIZMANN, J.-C., REDLICH, M., & BARTELMANN, M. (2012b): *The strongest gravitational lenses. II. Is the large Einstein radius of MACS J0717.5+3745 in conflict with ΛCDM?* A&A, **547**, A67

WAIZMANN, J.-C., REDLICH, M., MENEGHETTI, M., & BARTELMANN, M. (2014): *The strongest gravitational lenses. III. The order statistics of the largest Einstein radii*. A&A, **565**, A28

WALKER, A. G. (1935): *On Riemanntan spaces with spherical symmetry about a line, and the conditions for isotropy in genj relativity*. The Quarterly Journal of Mathematics, **6**, 81

WARREN, M. S., ABAZAJIAN, K., HOLZ, D. E., & TEODORO, L. (2006): *Precision Determination of the Mass Function of Dark Matter Halos*. ApJ, **646**, 881

WEINBERG, S., *Cosmology* (Oxford University Press, 2008)

WILLIAMSON, R., BENSON, B. A., HIGH, F. W., ET AL. (2011): *A Sunyaev-Zel'dovich-selected Sample of the Most Massive Galaxy Clusters in the 2500 deg^2 South Pole Telescope Survey*. ApJ, **738**, 139

ZHANG, J., FAKHOURI, O., & MA, C.-P. (2008): *How to grow a healthy merger tree*. MNRAS, **389**, 1521

ZHANG, Y., YANG, X., FALTENBACHER, A., ET AL. (2009): *The Spin and Orientation of Dark Matter Halos Within Cosmic Filaments*. ApJ, **706**, 747

ZIBIN, J. P. (2008): *Scalar perturbations on Lemaître-Tolman-Bondi spacetimes*. Phys. Rev. D, **78** (4), 043504

ZIBIN, J. P. & MOSS, A. (2011): *Linear kinetic Sunyaev-Zel'dovich effect and void models for acceleration*. Classical and Quantum Gravity, **28** (16), 164005

ZIBIN, J. P., MOSS, A., & SCOTT, D. (2008): *Can We Avoid Dark Energy?* Physical Review Letters, **101** (25), 251303

ZITRIN, A., BROADHURST, T., BARKANA, R., REPHAELI, Y., & BENÍTEZ, N. (2011): *Strong-lensing analysis of a complete sample of 12 MACS clusters at z > 0.5: mass models and Einstein radii*. MNRAS, **410**, 1939

ZITRIN, A., BROADHURST, T., BARTELMANN, M., ET AL. (2012): *The universal Einstein radius distribution from 10 000 SDSS clusters*. MNRAS, **423**, 2308

ZITRIN, A., BROADHURST, T., REPHAELI, Y., & SADEH, S. (2009): *The Largest Gravitational Lens: MACS J0717.5+3745 (z = 0.546)*. ApJ, **707**, L102

ZUMALACÁRREGUI, M., GARCÍA-BELLIDO, J., & RUIZ-LAPUENTE, P. (2012): *Tension in the void: cosmic rulers strain inhomogeneous cosmologies*. J. Cosmology Astropart. Phys., **10**, 009

ACKNOWLEDGEMENTS

Finally, it is a great pleasure to thank several people who contributed to this thesis in many different ways. I am deeply grateful to all of them.

First and foremost, I would like to thank you, Matthias, for being a great mentor – not only professionally but also personally; for supporting my research plans, although they did not always coincide with your own interests; for giving me maximum freedom and never putting any pressure on me; for supporting my research visit at the University of Sydney; and for your valuable guidance. Thank you very much!

I would like to thank Luca Amendola for kindly accepting to be the second referee of my thesis as well as Karlheinz Meier and Volker Springel for being examiners in my Ph.D. defence.

Geraint F. Lewis kindly invited me to visit his Gravitational Astrophysics group at the Sydney Institute for Astronomy (SIfA). The year in Sydney was truly superb! I want to thank Geraint for this opportunity, his great support, his valuable contributions, and the joyful discussions. At the same time, I would like to thank Krzysztof Bolejko for his tireless support, for always being very helpful, for teaching me so much about inhomogeneous cosmological models, and for the numerous contributions to this thesis. Krzysztof, thank you very much! My year in Sydney would not have been as pleasurable without the friendly and open minded colleagues at SIfA. In particular, I would like to mention Foivos (Greek pasta!), Hareth, Magda, and Stuart.

Now, it is time to thank my superb colleagues at the Institute for Theoretical Astrophysics (ITA). Without all of you – the famous ITA girls and ITA boys – the time at ITA would not have been so enjoyable. I will always remember the relaxed and pleasant working atmosphere as well as the truly legendary coffee breaks. In particular, I want to thank Jean-Claude (yes, you still count as an ITA boy) for the productive collaboration although we never worked at the same institute during the last three years. Sven, I really enjoyed (and still enjoy) the close collaboration with you. Thank you also for proofreading the first part of my thesis. I am very thankful to Christian, not so much for teaching me countless details about Star Wa... , ahem, Star Trek, but for teaching me how to typeset properly and for carefully proofreading large parts of my thesis. At last, I want to thank my awesome (former) office mates: Alex, Britta, Christian, Gero, Jonas, and our frequent visitor Björn. Thank you for standing all the lame jokes, for sharing so many funny moments, for valuable – sometimes even profound – discussions, and many more things! Northeim office is a great place!

I am deeply grateful to my family! Without your enduring support, this thesis clearly would not exist. You enabled me to study without worries and without ever expecting any return. You never stopped encouraging me. You were always there for me. Thank you!

Finally, I am profoundly grateful to you, Barbara, for always being supportive and motivating, for cheering me up and making me laugh, for giving me all the time I needed, and for so many other things that do not belong here!

COLOPHON

This document was typeset using the (slightly modified) typographical look-and-feel `classicthesis` developed by André Miede. The style was inspired by Robert Bringhurst's seminal book on typography "*The Elements of Typographic Style*". `classicthesis` is available for both LaTeX and LyX:

http://code.google.com/p/classicthesis/